CWP-639
May 2009

Estimation and Analysis of Attenuation Anisotropy

Jyoti Behura

— Doctoral Thesis —
Geophysics

Defended May 1, 2009

Committee Chair: Dr. Donna Anderson
Advisor: Dr. Ilya Tsvankin

Committee members:
Dr. Ken Larner
Dr. Tom Davis
Dr. Luis Tenario
Dr. Jim Gaiser

Center for Wave Phenomena
Colorado School of Mines
Golden, Colorado 80401
(1) 303 273-3557

Abstract

Attenuation and attenuation anisotropy can furnish valuable information about lithology, fluids, and fractures in rocks. Properties such as permeability, fluid mobility and saturation that are difficult to measure using conventional velocity or amplitude-variation-with-offset (AVO) analysis could possibly be extracted from attenuation measurements.

To understand the response of such highly viscoelastic rocks as oil shales to seismic waves and thermal stimulation, I study their shear-wave properties within the seismic frequency band (0.01 Hz to 80 Hz) for a wide range of temperatures (30°C-350°C). The physical state of the kerogen in the shales is extremely sensitive to heat, which makes estimation of shear-wave properties of oil shales particularly attractive. Although the shear-wave moduli and attenuation have a negligible dependence on frequency, they show substantial variation with temperature. The melting of kerogen can increase attenuation by a factor of 10 and at the same time decrease the shear-wave velocity by a factor of five. Velocity and attenuation anisotropy also show significant variations with temperature; the SH-wave velocity-anisotropy parameter γ could attain anomalously large values approaching three.

Using first-order perturbation theory, I analyze the influence of the inhomogeneity angle ξ (the angle between the real and imaginary parts of the wave vector) on velocity and attenuation in arbitrarily anisotropic media. For a wide range of small and moderate angles ξ, the group attenuation coefficient $\mathcal{A}_g$ practically coincides with the phase attenuation coefficient $\mathcal{A}|_{\xi=0^\circ} = 1/(2Q)$ which suggests that the estimated attenuation ($\mathcal{A}_g$) is a direct measure of the intrinsic attenuation of the subsurface. I then analyze reflection coefficients at boundaries between attenuative anisotropic media by developing linearized expressions for plane-wave reflection/transmission coefficients in terms of the velocity- and attenuation-anisotropy parameters, as well as the velocity and attenuation contrasts across the interface. Only in the presence of strong attenuation ($Q < 10$) does the contribution of the attenuation-related terms become comparable to that of the velocity terms. Interestingly, for an incident wave with a nonzero inhomogeneity angle ξ, the form of the linearized reflection coefficients is different from the conventional AVO expression.

To estimate interval anisotropic attenuation from reflection seismic data, I adopt a

layer-stripping approach that incorporates a modified spectral-ratio method. While there are no restrictions on heterogeneity and anisotropy of the target layer, the overburden has to be composed of laterally homogeneous layers with a horizontal symmetry plane (e.g., layers may be orthorhombic). Numerical examples for horizontally layered VTI (transversely isotropic with a vertical symmetry axis) and orthorhombic media confirm that the method yields accurate interval phase attenuation coefficients even for models with uncommonly strong attenuation and substantial velocity and attenuation anisotropy.

I apply the layer-stripping approach to wide-azimuth P-wave data acquired over a gas reservoir in the Coronation Field, Alberta and estimate the interval anisotropic P-wave velocity and attenuation fields. The lower half of the survey area shows strong azimuthal velocity anisotropy with the vertical symmetry planes aligned consistently along the NS- and EW-directions. The vertical attenuation coefficient shows a reasonable correspondence with existing gas-producing well locations. Interval attenuation anisotropy is anomalously strong and much higher than velocity anisotropy.

This thesis is dedicated to

Bapa, Maa, Lulu bhai, Tukunu apa, and Jinu apa

for their unconditional love and support.

Do not go where the path may lead, go instead where there is no path and leave a trail.

-Ralph Waldo Emerson

Table of Contents

Acknowledgments

This day takes me back to the spring of 2003 when I decided to pursue a PhD degree in the US. At that time I was not sure what attracted me to grad school and, above all, if it was the right decision. It has been almost six years since then and I still cannot say if I made the right choice. However, now I do realize that higher education has been a journey of self-discovery. This journey has by no means been easy or without stumbling blocks; it has, however, taught me lessons that will last a lifetime and given me memories that I will forever cherish. One of the pleasures of concluding this thesis is the opportunity to thank all the people who have been a part of this endeavor.

Farnoush has given me the love and support that have carried me through rough times. She has not only been a constant source of inspiration, but also someone I could always bounce ideas off of. Her wisdom and kindness have made me a better man. Shayan has been a great friend and an entertaining companion. My soccer skills have vastly improved because of the numerous kick-some-ball sessions with him. I am certain that with the skills he possesses, we could soon see him playing for Manchester United and 'schooling' Christiano Ronaldo (though he thinks he is already better than Ronaldo). The first few years of my PhD were especially rough and Xiaoxia was always there to guide me. Our numerous discussions on research, life, politics, and religion helped shape my thinking in many ways and made her a friend for life.

My committee members: Ilya Tsvankin, Ken Larner, Tom Davis, Luis Tenorio, Donna Anderson, and Jim Gaiser were always ready to answer my questions and offer advice. Discussions with them opened my eyes to novel ideas and different perspectives on the same problem. Ken was extremely helpful in editing many of my manuscripts. His probing questions led to intelligent discussions that have shaped my research interests in more ways than one. Luis taught me statistics and helped me with the statistical analysis in some of my publications. Tom and Jim provided me with the necessary practical viewpoint, and Donna gave a lot of geological input. I will always be thankful to them for this constructive relationship.

My thesis advisor, Ilya Tsvankin, has provided me with the guidance that has led to

the successful completion of this thesis. He has given me adequate freedom to work on my ideas and, at the same time, shown me the right direction when I went astray. Ilya's ability to suggest the correct explanations for my observations and to accurately predict the outcome has always amazed me. He has also taught me the art of writing scientific documents and instilled in me the confidence to do independent research.

I feel fortunate to have worked with Mike Batzle on my second comprehensive project. His refreshingly healthy and carefree view of the world made working with him fun and fruitful at the same time. Roel Snieder is the quintessential scientist. Always open to new ideas and a constant source of encouragement, he is perfect to share ideas with. CWP prides itself on its professional presentations and John Hogan taught me how to do this. With his soft yet commanding voice, he helped me hone my oral communication skills. Paul Sava let me sit in his imaging classes; his ability to simplify complicated ideas made learning fun and interesting. The help and encouragement of Vladimir Grechka, John Dorgan, Terry Young, Ken Larner, Joe Dellinger, Nurul Kabir, Subhashish Mallick, Martin Landrø, Tom Davis, Luis Tenorio, Evert Slob, Dirk Gajewski, and Ivan Pšenčík has made my stay at CSM extremely beneficial.

In many ways, much of this work would not have been possible or would have been delayed had it not been for the computational expertise of John Stockwell. I am grateful to him for putting up with my continual demand for faster machines, newer operating systems, and current software. As Farnoush once said, Barbara McLenon has been like a mom to many of us. Although she is the publication specialist at CWP, she takes time to be the social face of the group and makes it a point to regularly ask abount our well-being. There is none more efficient and organized than Michelle Szobody. A thorough professional, she was always there to solve our problems with her characteristic, "I will take care of it." Judy Armstrong and Norm Bleistein are wonderful people and the time I spent at their place in Frisco was special. Apart from Ilya, Diane Witters played a significant role in improving my technical writing.

The Geophysics Department, with Terry Young at the head, has created a wonderful environment that fosters learning and collaboration which has helped me expand my horizons. I am grateful to BP and Occidental Oil and Gas Corporation for the internship opportunities. GX Technology and Apache Corporation, through Alex Calvert and Edward Jenner, provided me with field data to test my ideas. Besides the financial support provided by CWP for all these years, the SEG scholarship and the ConocoPhillips Spirit scholarship

went a long way in helping me with academic needs. I will always be grateful for their generosity.

I have made many friends along the way. They have helped me, in one way or another, in my quest for this degree. Steve Smith is a storehouse of information and has the uncanny ability to make people laugh with weird jokes. The many table tennis sessions with Pawan Dewangan were loads of fun. The talented Sanne Cottar is a great friend and fun to hang out with. Rodrigo Fuck always amazed me with his intelligence and insightful comments. Yris Olaya is a fun hiking companion and spoiled me with tasty Colombian food on many occassions. Gabriela Melo is a great dancing partner and I will always cherish our Salsa evenings. Kurang Mehta is an honest man whose discipline always impressed me. There was never a dull moment with Ivan Vasconcelos; the summer of 2005 that we spent together in Houston was pleasant. Jia Yan will always be one of my favourite juniors. PhD work usually has many speed-bumps, but rarely there are any speed-killers. While working on the field data date, I encountered a speed-killer which rendered more than a month's work useless. At this crucial juncture Steve Smith, Farnoush Forghani, Filippo Broggini, Jia Yan, Myong Jae Kwon, Xiaoxiang Wang, Yongxia Liu, Yong Ma, Mamoru Takanashi, Yuanzhong Fan, Ran Xuan, and Rosie came to my rescue; they offered me to use their computers which helped me finish the thesis on time. I will always be grateful for their generosity. I am also thankful to Debashish Sarkar, Matt Haney, Kasper van Wijk, Crucelis (Cucha) Lopez, Matt Reynolds, Eldar Guliyev, Elmar Safarov, Eugenia Rojas, Yaping Zhu, Masatoshi Miyazawa, Laxmidhar Behera, Barry Kirkendal, Whitney Goodrich, Carlos Pacheco, Ronny Hofmann, Agnibha Das, Rituparna Sarker, Katie Baker, Damien Jougnot, Rajinder Singh, Milana Ayzenberg, and Ludmila Adam for their help and support.

Labanyendu bhai constantly encouraged and helped me with my efforts to join IIT. My sister-in-law Mili apa, brother-in-law Srinu bhai, niece Litun, and my nephew Dholu (I doubt if he will like his name when he grows up) have given me a lot of joy.

All of my achievements and successes also belong to my family who has been by my side every step of the way. I can vividly recall the evenings my mother, Manjushree, spent teaching me English grammar and copying exercises from textbooks so that I could solve them later. Her love and kindness will forever shape my life. My father, Arjun, taught me the value of hard work, honesty, and discipline. His principle of 'simple living, high thinking' has gone a long way in my success. My brother, Sidharth, has been a life-long friend and support. Through his perseverence, he has shown me that one can achieve great

heights if he is focused and determined. Tukunu apa inherits my mother's kindness and my father's wisdom and has been a source of inspiration all through my life. As a kid, I used to look up to her, and I am glad I still do. Jinu apa possesses the passion and strong resolve to get any task done. Only her love and loyalty to the family surpass her bravery. To these wonderful people, I dedicate this thesis.

Chapter 1

Introduction

1.1 Attenuation of Seismic Waves and Attenuation Anisotropy

Attenuation is the gradual loss of intensity of a wave as it travels through a medium. In physics, attenuation generally refers to loss of energy arising from scattering as well as absorption. In geophysics, however, attenuation typically refers only to partial conversion of seismic energy to other forms of energy such as heat. This loss of energy manifests itself in a decrease of amplitude and alteration of the frequency content of waves traveling through the subsurface. Also, in the presence of attenuation, waves exhibit velocity dispersion.

Attenuation analysis can provide valuable information about lithology, presence of fluids, and physical properties of subsurface rocks (e.g., Johnston *et al.*, 1979; Johnston & Toksöz, 1981; Winkler & Nur, 1982; Vo-Thanh, 1990; Gautam *et al.*, 2003; Prasad & Nur, 2003; Batzle *et al.*, 2006; Behura *et al.*, 2007). Several publications exploit this property to delineate steam floods (Macrides *et al.*, 1988; Hedlin *et al.*, 2001) and monitor the thermal recovery of hydrocarbons (Eastwood *et al.*, 1994; Dilay & Eastwood, 1995), while Rapoport *et al.* (2004) use it as a direct hydrocarbon indicator (DHI). Valle-García & Ramírez-Cruz (2002) note that zones of relatively high attenuation coincide with the producing formations in a mature oil field; Quan & Harris (1997) claim that their attenuation-tomography results have good correlation with lithology. In addition, other properties such as permeability, mobility of fluids, and fluid saturation that cannot be inferred from velocity or amplitude-variation-with-offset (AVO) analysis could possibly be extracted from attenuation analysis. Patchy-saturation models of Pride & Berryman (2003) and Johnson (2001) provide adequate physical explanation for the relationship between attenuation and saturation. Using a mesoscopic-loss model, Pride & Berryman (2003) show that fluid flow can result in high attenuation within the seismic bandwidth. Their model predicts a linear relation between Q and permeability and therefore the measured attenuation should be an indicator of per-

meability. Experimental verification of their model is provided by Gautam *et al.* (2003) who observe a direct relationship between attenuation and fluid mobility - the lower the mobility, the smaller is the frequency of maximum attenuation. Using many field-data examples and rock-physics models, Pride *et al.* (2003) argue that permeability is related to seismic attenuation.

The angular velocity variation (velocity anisotropy) and its influence on traveltimes and amplitudes of seismic waves has been extensively studied in the literature (e.g., Backus, 1962; Thomsen, 1986; Helbig, 1994; Alkhalifah & Tsvankin, 1995; Tsvankin, 1997; Rüger, 1997, 1998; Grechka & Tsvankin, 1998; Wang, 2002; Crampin & Peacock, 2005; Tsvankin, 2005). Like velocity, attenuation can also be anisotropic, as demonstrated by many laboratory experiments (e.g., Hosten *et al.*, 1987; Tao & King, 1990; Best, 1994; Prasad & Nur, 2003; Behura *et al.*, 2006; Zhu *et al.*, 2007b) and field studies (e.g., Ganley & Kanasewich, 1980; Hiramatsu & Ando, 1995; Liu *et al.*, 2007; Maultzsch *et al.*, 2007). In fact, attenuation anisotropy often is stronger than velocity anisotropy (Hosten *et al.*, 1987; Arts & Rasolofosaon, 1992; Zhu *et al.*, 2007b).

Many of the factors that cause velocity anisotropy, such as directionally-dependent stress and interbedding of thin layers, are also responsible for attenuation anisotropy (e.g., Liu *et al.*, 1993; Carcione, 1992; Molotkov & Bakulin, 1998; Stanley & Christensen, 2001; Prasad & Nur, 2003; Behura *et al.*, 2006; Zhu *et al.*, 2007a). The structural arrangement of the rock matrix can also cause anisotropic attenuation. For example, frictional loss (Walsh, 1966; Buckingham, 2000) due to bedding-parallel shearing should be higher than the loss from bedding-perpendicular shearing.

The primary cause of attenuation anisotropy, however, is believed to be the preferential flow of fluids in the rock (e.g., Mavko & Nur, 1979; Akbar *et al.*, 1993; Parra, 1997; MacBeth, 1999; Brajanovski *et al.*, 2005). Using different fluid-flow models, Pointer *et al.* (2000) show that aligned fluid-filled cracks can result in anisotropic attenuation. The poroelastic model of Chapman (2003) can explain strong anisotropic attenuation in the seismic bandwidth. Azimuthal scattering (Willis *et al.*, 2004) and anisotropy of the density tensor in poroelastic Biot media (Molotkov & Bakulin, 1998) are some other possible causes of the angular variation of attenuation coefficients.

In isotropic media, attenuation is most commonly quantified in terms of the quality factor Q and the attenuation coefficient (Johnston & Toksöz, 1981). Wave propagation in attenuative anisotropic media is more complicated as seen from the detailed study of Carcione

(2000). His results, expressed in terms of stiffness coefficients, however, are not suitable for seismic data processing purposes. Zhu & Tsvankin (2006) introduced the Thomsen-style notation – two isotropic reference quantities ($\mathcal{A}_{P0}$ and $\mathcal{A}_{S0}$) and three dimensionless parameters (ϵ_Q, δ_Q, and γ_Q) – for describing attenuation coefficients in transversely isotropic (TI) media. The coefficients $\mathcal{A}_{P0}$ and $\mathcal{A}_{S0}$ represent the symmetry direction P- and S-wave normalized attenuation coefficients:

$$\mathcal{A}_{P0} = \frac{1}{2Q_{33}}, \tag{1.1}$$

$$\mathcal{A}_{S0} = \frac{1}{2Q_{55}}, \tag{1.2}$$

where $Q_{ij} = c_{ij}^R/c_{ij}^I$ is the Q-factor matrix and c_{ij} is the complex stiffness tensor. The attenuation-anisotropy parameter ϵ_Q represents the fractional difference in P-wave attenuation coefficients along the symmetry direction and the isotropy plane:

$$\epsilon_Q = \frac{Q_{33} - Q_{11}}{Q_{11}}, \tag{1.3}$$

the parameter δ_Q controls the attenuation in the vicinity of the symmetry axis:

$$\delta_Q = \frac{1}{\mathcal{A}_{P0}} \frac{d^2\mathcal{A}(\theta)}{d\theta^2}\bigg|_{\theta=0^\circ} = \frac{4}{g^2}\frac{Q_{33} - Q_{55}}{Q_{55}} + 2\frac{Q_{33} - Q_{13}}{Q_{13}}\left(1 + 2\delta - \frac{2}{g^2}\right), \tag{1.4}$$

and γ_Q is responsible for the attenuation anisotropy of SH-waves:

$$\gamma_Q = \frac{Q_{55} - Q_{66}}{Q_{66}}, \tag{1.5}$$

where $g = V_{P0}/V_{S0}$ is the velocity ratio, V_{P0}, V_{S0} are the symmetry-direction P- and S-wave velocities, and δ is the Thomsen velocity-anisotropy parameter (Thomsen, 1986). A similar Tsvankin-style notation (Tsvankin, 1997) describing attenuation coefficients in orthorhombic media was introduced later by Zhu & Tsvankin (2007).

1.2 Rock-physics of Viscoelastic Materials

Although many publications have studied the magnitude of attenuation and attenuation mechanisms in the laboratory, almost all existing measurements (e.g., Lockner *et al.*, 1977; Toksöz *et al.*, 1979; Winkler & Nur, 1982; Murphy *et al.*, 1986; O'Hara, 1989; Vo-

Figure 1.1: The pitch-drop experiment is a long-term test which measures the flow of a piece of pitch over many years (Edgeworth *et al.*, 1984). Pitch (bitumen) is a highly viscous liquid which appears solid at room temperature. Tar pitch flows extremely slowly at room temperature, eventually forming a drop.

Thanh, 1990) are in the ultrasonic frequency bandwidth. In contrast, the bandwidth of typical seismic surveys is between 5 Hz and 100 Hz. Consequently, there might not be a direct correspondence between the laboratory measurements and field data. Application of ultrasonic measurements to interpretation of seismic data involves extrapolation which could contain large errors (Tutuncu *et al.*, 1998; Batzle *et al.*, 2006). In fact, attenuation mechanisms inferred from laboratory experiments might not even exist within the seismic bandwidth. Note that velocities in attenuative rocks can vary substantially with frequency (Batzle *et al.*, 2006). Therefore, experimentally-determined velocities at ultrasonic frequencies likely differ from the velocity of seismic waves (Tutuncu *et al.*, 1998).

This is especially true for rocks saturated with viscoelastic fluids, such as heavy oils (in tar sands, Figure 1.1) and kerogen (organic matter in shales). Since the "pore-fluids" are viscoelastic, the rock properties in the seismic band would be significantly different from those in the logging-frequency range and the ultrasonic band. Also, unlike common fluids (e.g. brine and light oil), kerogens and heavy oils act as solids at room temperatures and

fluids at higher temperatures. The physical properties of these rocks can change substantially during the thermal hydrocarbon-recovery procedures. Therefore, experimental study of the physical properties of such strongly viscoelastic rocks in the laboratory should be done within the seismic bandwidth and thermal-recovery temperatures.

1.3 Influence of the Inhomogeneity Angle

Although experimental measurements provide useful physical insight into the possible attenuation mechanisms and the magnitude of attenuation coefficients, it is extremely difficult to study different aspects of wave propagation in isolation in the laboratory. One such issue is the influence of the so-called inhomogeneity angle. In attenuative media, the direction of maximum attenuation ($\mathbf{k}^I$) might differ from the direction of wave propagation ($\mathbf{k}^R$), and the angle between these two directions is referred to as the inhomogeneity angle ξ (Figure 1.2). The inhomogeneity angle has been measured only in laboratory experiments (Huang *et al.*, 1994; Deschamps & Assouline, 2000). Estimating this angle from seismic data is extremely difficult. Because of the complexity arising from the introduction of the inhomogeneity angle, wave propagation has been traditionally studied in the "homogeneous" regime (Hauge, 1981; Tonn, 1991; Hiramatsu & Ando, 1995; Neep *et al.*, 1996; Dasgupta & Clark, 1998; Vasconcelos & Jenner, 2005; Maultzsch *et al.*, 2007; Zhu *et al.*, 2007b). For point-source radiation in weakly attenuative anisotropic media, the angle ξ is usually small and can be ignored (Zhu, 2006; Vavryčuk, 2008). In the presence of layering and other types of heterogeneity, however, ξ can attain large values. For the model in Figure 1.3, the wave vector in the elastic cap rock is real, while the wave vector of the transmitted wave in the attenuative reservoir is complex. According to Snell's law, the projection of the slowness vector onto the interface has to be preserved, which means that the attenuation vector ($\mathbf{k}^I$) of the transmitted wave has to be orthogonal to the interface. Then the resulting inhomogeneity angle of the transmitted wave is equal to the transmission angle and can approach 90°.

It is natural to expect that the inhomogeneity angle should influence the attenuation coefficient measured from seismic data. In addition, attenuation analysis becomes particularly involved in anisotropic media where the ray may significantly deviate from both the phase direction and the direction of maximum attenuation. When the medium is anisotropic, the relationship between the angle ξ and the attenuation coefficients is obscured by the complexity of the exact equations. Therefore, one of the primary goals of this

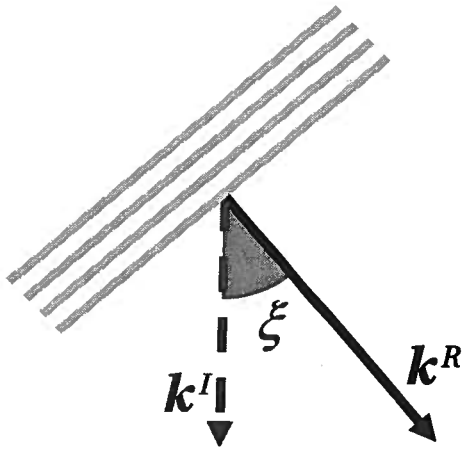

Figure 1.2: Plane wave with a nonzero inhomogeneity angle ξ. The wave propagates in the direction $\mathbf{k}^R$ (perpendicular to the planes of constant phase) and attenuates most rapidly in the direction $\mathbf{k}^I$.

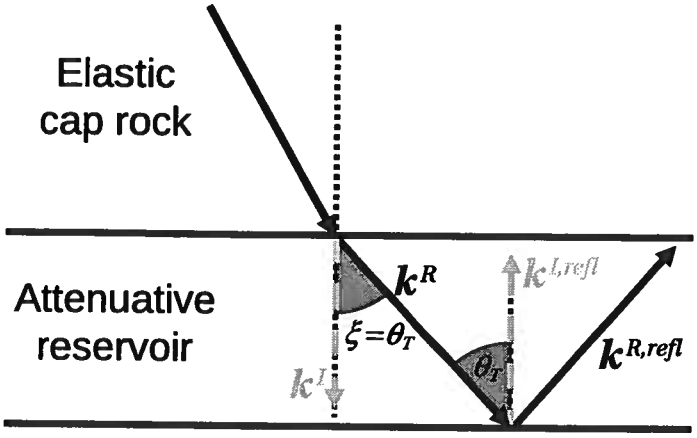

Figure 1.3: Illustration of the reflection/transmission problem at the interface between a purely elastic cap rock and an attenuative reservoir. $\mathbf{k}^R$ and $\mathbf{k}^I$ are the real and imaginary parts of the wave vector of the transmitted wave, while $\mathbf{k}^{R,refl}$ and $\mathbf{k}^{I,refl}$ correspond to the reflected wave. The inhomogeneity angle ξ of the transmitted wave is equal to the transmission angle θ_T.

thesis is to address the influence of the inhomogeneity angle on phase and group attenuation coefficients.

1.4 Reflection Coefficients in Attenuative Media

While most existing attenuation studies are focused on plane-wave attenuation coefficients, which determine the amplitude decay along the raypath of seismic waves, it is also important to evaluate the influence of attenuation and attenuation anisotropy on reflection coefficients. Conventional AVO analysis is carried out under the assumption that the subsurface is purely elastic, which leads Luh (1988) and Samec *et al.* (1990) to attribute some failures of AVO studies to the influence of attenuation. A number of publications have been devoted to the analysis of reflection coefficients in elastic isotropic (e.g., Bortfeld, 1961; Shuey, 1985; Aki & Richards, 2002) and anisotropic (e.g., Banik, 1987; Rüger, 1997, 1998; Vavryčuk & Psencík, 1998; Jílek, 2002b) media. Whereas a handful of studies have focused on reflection coefficients in attenuative isotropic media (Krebes, 1983; Ursin & Stovas, 2002; Nechtschein & Hron, 1997; Hearn & Krebes, 1990), the influence of attenuation anisotropy on reflection coefficients has not been sufficiently addressed. Existing publications (Stovas & Ursin, 2003; Carcione, 2007) do not provide insight into the behavior of reflection coefficients in attenuative anisotropic media and do not take the influence of the inhomogeneity angle into account. Therefore, the thesis also addresses the important practical problem of the behavior of plane-wave reflection coefficients for an interface between two anisotropic attenuative media.

1.5 Estimating Attenuation from Seismic Data

Since attenuation and attenuation anisotropy can provide valuable information about the lithology, physical properties, and fluid properties of rocks, it is highly desirable to estimate attenuation coefficients from seismic data. However, despite significant progress in the understanding of attenuation mechanisms and wave propagation in attenuative media, estimation of attenuation coefficients from seismic data remains to be a challenging problem. Although there have been some recent advances in estimating attenuation from vertical seismic profiling (VSP) (Ganley & Kanasewich, 1980; Amundsen & Mittet, 1994; Hedlin *et al.*, 2001; Maultzsch *et al.*, 2007) and crosswell (Macrides *et al.*, 1988; Neep *et al.*, 1996) data, extraction of interval attenuation from reflection seismic data remains to be elusive. In

a few existing case studies of attenuation analysis using reflection data (e.g., Vasconcelos & Jenner, 2005), the attenuation coefficient is estimated for a stack of layers above the reflector. Dasgupta & Clark (1998) introduce a technique for estimating interval attenuation from reflection data based on the spectral-ratio method. Their algorithm, however, is restricted to zero-offset reflections and requires knowledge of the source signature. One of the goals of the thesis is to develop an algorithm for extracting the interval anisotropic attenuation from reflection seismic data.

This thesis addresses all the above issues and spans over laboratory, theoretical, and field studies.

1.6 Thesis Overview

As discussed above, to develop a better rock physics model, one needs to conduct experiments at seismic frequencies, which is done in **Chapter 2**. The velocity, attenuation, and anisotropy of two shale samples, one rich in organic content and the other a lean shale, are studied in the laboratory under varying temperatures. The frequency of investigation ranges from 0.01 Hz to 80 Hz (to include the seismic bandwidth) and the temperatures range between 30°C and 350°C to simulate thermal-recovery conditions of hydrocarbons in oil shales. This experiment sheds new light on the attenuation mechanisms in shales at seismic frequencies and thermal-recovery temperatures. Increasing temperature results in liquefaction and subsequent volatilization of the organic content (kerogen). Such phase changes not only cause significant fluctuations in velocity and attenuation, but also lead to strong velocity and attenuation anisotropy.

The influence of the inhomogeneity angle on phase and group attenuation coefficients is analyzed in **Chapter 3**. Using a perturbation approach, I show that for a wide range of small and moderate values of ξ, the group attenuation coefficient (estimated from seismic data) is not influenced by ξ and represents a measure of the intrinsic attenuation. This conclusion remains valid even for uncommonly high attenuation ($Q \approx 10$) and strong velocity and attenuation anisotropy. For large ξ approaching the so-called "forbidden directions", however, the group attenuation coefficient depends on the inhomogeneity angle and no longer yields the intrinsic attenuation.

In **Chapter 4**, using a perturbation approach (similar to that of Vavryčuk & Psencík, 1998), I study the influence of anisotropic attenuation on reflection coefficients for an interface between two arbitrarily anisotropic media. I show that only when attenuation is

strong (the quality factor $Q < 10$), its contribution to the reflection coefficients is substantial. For such highly attenuative media, it is also necessary to take attenuation anisotropy into account, if the magnitude of the Thomsen-style attenuation-anisotropy parameters is relatively large. Also, a nonzero inhomogeneity angle of the incident wave introduces additional terms into the PP- and PS-wave reflection coefficients, which makes conventional AVO analysis inadequate for strongly attenuative media.

In **Chapter 5**, I introduce a novel technique for extracting interval anisotropic attenuation coefficients from reflection data. This method is based on the kinematic layer-stripping technique developed by Dewangan & Tsvankin (2006) and uses a modified version of the spectral-ratio method (Johnston & Toksöz, 1981). While no information about velocity and attenuation anywhere in the medium is required, the overburden has to be laterally homogeneous with a horizontal symmetry plane.

As a test of this algorithm, in **Chapter 6** I process a 3D wide-azimuth land dataset from Coronation, Alberta, Canada. I compute the interval P-wave anisotropic velocity and attenuation fields within a target layer comprising the gas-sand reservoir. The estimated vertical attenuation coefficient shows a reasonable correspondence with locations of existing gas-producing wells.

Chapter 2

The Shear Properties of Oil Shales

2.1 Summary

Organic-rich shales house large untapped amounts of hydrocarbons. In-situ recovery of hydrocarbons from oil shales involves thermal cracking and steam-flooding of these reservoirs, which changes their physical properties, in particular shear properties. I study, within the seismic band, the shear properties (the rigidity moduli and attenuation) of two types of oil shales, one rich and the other low in organic content (kerogen). To understand the influence of thermal recovery processes, I also analyze these shales for a wide range of temperatures.

Both the kerogen-rich and lean shales show a weak dependence of rigidity (shear) moduli and attenuation on frequency within the seismic bandwidth. These shales, however, show a dramatic change in shear-wave velocity and attenuation with temperature. Their shear moduli and quality factor (Q) decrease with melting of the kerogen; however, with further loss of some of the kerogen, both shear moduli and Q increase. The magnitude of these changes along the direction of the bedding and perpendicular to the bedding differ, which makes velocity and attenuation anisotropy potentially valuable attributes. Both velocity and attenuation anisotropy of the shales can change significantly with temperature, in some cases by more than an order of magnitude. The SH-wave anisotropy parameter γ is closely related to the physical state of kerogen in the shale and could possibly be used as a direct indicator of the extent of kerogen-melt in the rock. The kerogen content in shales also influences their velocity and attenuation. The greater the organic content, the lower is the shear modulus and the higher the attenuation. In addition, shales with higher organic content show a substantially greater change in the shear moduli with temperature compared to lean shales. Such dramatic changes in velocity and attenuation in oil shales with heating should be clearly visible in seismic data, offering the promise that these measurements can

be qualitatively and quantitatively used in seismic analysis.

2.2 Introduction

Increased demand has fostered interest in unconventional hydrocarbon sources such as heavy oils and oil shales. These energy resources have reserves that are nearly triple the world reserves of conventional oil and gas.

A vast unexploited source of hydrocarbons is oil shales, i.e., shales rich in kerogen. The Schlumberger Oilfield Glossary defines kerogen as "the naturally occurring, solid, insoluble organic matter that occurs in source rocks and can yield oil upon heating." The original organic constituents of kerogen are algae and woody plant material. Kerogens have a high molecular weight relative to bitumen, or soluble organic matter. Bitumen forms from kerogen during petroleum generation.

Estimates vary as to how much oil is contained in oil shale reserves. The US Office of Naval Petroleum and Oil Shale Reserves estimates there are some 1.6 trillion barrels of oil contained in oil shales around the world, with 60-70% of reserves (1.0-1.2 trillion barrels) in the United States. Most U.S. oil shale is concentrated in the Green River Formation in Wyoming, Utah, and Colorado. These oil shale resources occupy a total area of 16,000 square miles.

Technical challenges and environmental concerns, however, hinder oil-shale exploitation. Environmental considerations, for example, have prohibited surface mining. This calls for in-situ recovery, which, in turn, poses new technical challenges. One promising in-situ project is being carried out by Shell Oil Company under the name of the Mahogany Research Project in Colorado, which uses electrical heating. A heating element is lowered into the well and allowed to heat the kerogen over time, slowly converting it into oil and gas, which are then pumped to the surface.

Heating changes such physical properties as velocity, anisotropy, and attenuation, which can have a substantial influence on seismic wave propagation. Seismic techniques can play an important role in monitoring changes in these oil shale reservoirs. The seismic response of oil shales to varying temperature and pressure, however, is not well understood. To address this problem, experiments have been carried out under controlled conditions in the laboratory (Parker, 1968; Johnston, 1987; Mah, 2005). These studies, however, are limited to the ultrasonic frequency bandwidth.

Unlike common fluids (e.g., brine and light oil), kerogens found in oil shales act as solids

at room temperatures and fluids at higher temperatures. Therefore, at room temperature, kerogens support shear waves, but not at higher temperatures where the shear modulus approaches zero. They would, however, have a nonzero bulk modulus at all temperatures, and the percentage change in the bulk modulus should be smaller compared to the change in the shear properties. So the shear study of these rocks is more attractive than the study of their bulk properties, which makes acquisition of multicomponent seismic data all the more important.

To understand the shear behavior of oil shales in the seismic frequency band, I conduct experiments to estimate their shear moduli and attenuation under varying temperature (encompassing the thermal recovery process: 0°C-350°C) and frequency (encompassing the seismic bandwidth: 0.01Hz-80 Hz). I analyze two shale samples with different amounts of organic content from the Green River Formation, Colorado. To my knowledge, no such studies with a simultaneous change in temperature and frequency have yet been published.

2.3 Experiment

This method of calculating the complex shear modulus is well-known in polymer and soil science (Moyal & Fletcher, 1945; Wilhelm, 2002) and needs only minor corrections for the geometry of the sample. In fact, this method is not much different from the methodology used for rock measurements by Jackson & Paterson (1987). The same technique is also employed by Behura *et al.* (2007) to measure the shear properties of heavy oils and heavy-oil saturated rocks. For detailed mathematical description of the above operation, one can refer to the mechanical deformation of circular and rectangular shafts found in most textbooks on mechanics of solids (e.g., Crandall *et al.*, 1999). Measurements are carried out using a shear rheometer shown in Figure 2.1, and the experiment is schematically shown in Figure 2.2.

Apart from the mechanical components in Figure 2.1, the rheometer consists of an assemblage of electronics and a computer interface to electronically control the mechanical parts and acquire data. After selecting the geometry of the sample used in the analysis, the user defines the deformational sequence to be applied to the sample. The microprocessor translates the strain and strain rate history into the motion of the servo-controlled motor based upon the employed geometry. The sample is clamped at both ends, and in this case, measurements are conducted for dry rock samples and with no lateral confining stress. The sample temperature history is controlled during the test using convected gas in the

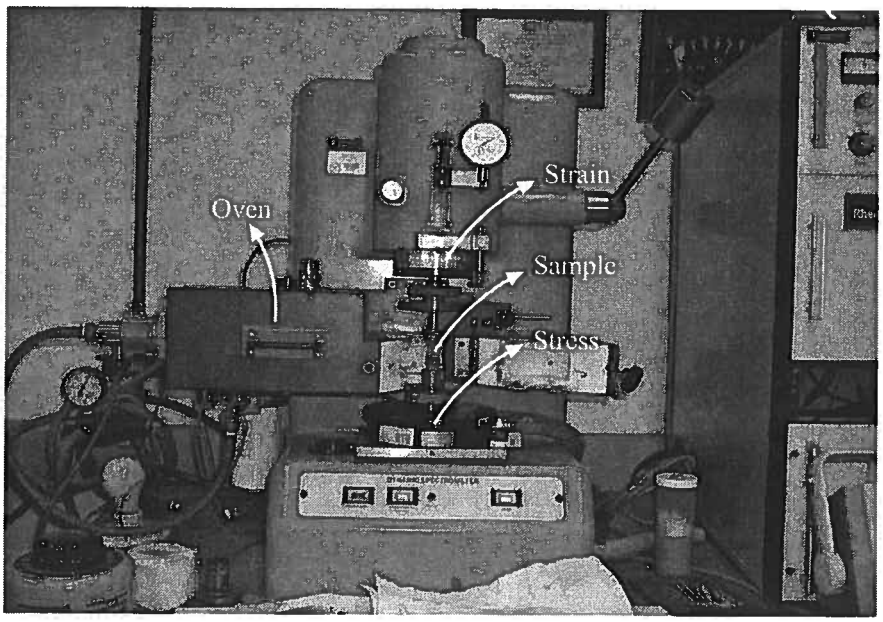

Figure 2.1: Rheometer used in the study.

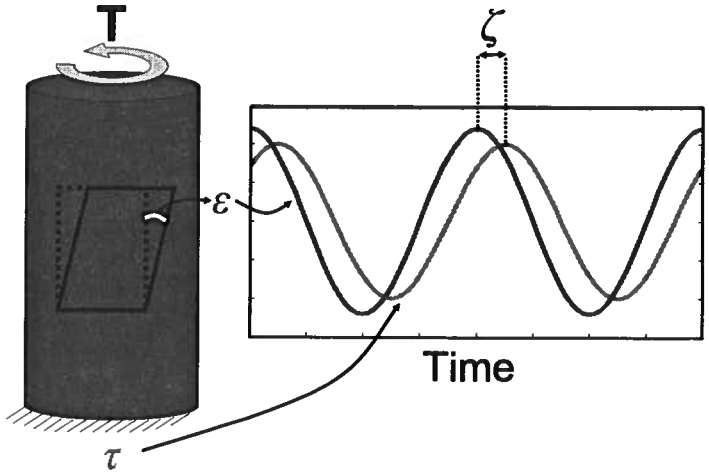

Figure 2.2: Schematic diagram of harmonic loading applied to one end of a rock sample. The applied torque **T** results in stress τ (red curve), which lags behind the strain ε (blue curve) by the phase angle ζ.

surrounding environmental chamber. A sinusoidal torsional strain is applied to one (free) end of the sample, and the resulting response is measured by a transducer at the other end, which is fixed. From this response, the computer calculates the resulting stresses and strains and generates values of the rheological properties.

This method of calculating the complex shear modulus is well-known in polymer and soil science (Moyal & Fletcher, 1945; Wilhelm, 2002) and needs only minor corrections for the geometry of the sample. In fact, this method is not much different from the methodology used for rock measurements by Jackson & Paterson (1987). The same technique is also employed by Behura *et al.* (2007) to measure the shear properties of heavy oils and heavy-oil saturated rocks. For detailed mathematical description of the above operation, one can refer to the mechanical deformation of circular and rectangular shafts found in most textbooks on mechanics of solids (e.g., Crandall *et al.*, 1999).

When a viscoelastic material is subjected to a sinusoidally varying strain, a steady state will be reached when the resulting stress is also sinusoidal with the same angular frequency, but a phase lag of ζ, which represents a measure of attenuation of that body (Gray, 1972; Nowick & Berry, 1972; Chow, 1995; Braun *et al.*, 2001). For an elastic material, $\zeta = 0$, while for a purely viscous fluid, ζ can approach $\pi/2$. The value of ζ for a viscoelastic body is between these two limits.

The harmonic strain ε and stress τ can be represented as

$$\varepsilon = \varepsilon_0 e^{-i\omega t}, \tag{2.1}$$

$$\tau = \tau_0 e^{-i(\omega t - \zeta)}, \tag{2.2}$$

where ω and ε_0 are the excitation frequency and amplitude, respectively and τ_0 is the peak amplitude of the resulting stress. The above complex form of the stress function is divided by the strain to give the complex dynamic shear modulus c:

$$c = \tau_0^R/\varepsilon_0 + i\,\tau_0^I/\varepsilon_0, \tag{2.3}$$

where

$$\tau_0^R = \tau_0 \cos\zeta, \tag{2.4}$$

$$\tau_0^I = \tau_0 \sin\zeta. \tag{2.5}$$

The in-phase part of the stress τ_0^R gives the "real" or "storage" modulus c^R and the out-of-phase part of the stress gives the "imaginary" or "loss" modulus, c^I,

$$c^R = \tau_0^R/\varepsilon_0, \tag{2.6}$$

$$c^I = \tau_0^I/\varepsilon_0. \tag{2.7}$$

We use the common definition of the quality factor, Q (inversely proportional to the attenuation coefficient) defined as (Gray, 1972; Nowick & Berry, 1972; Chow, 1995; Lakes, 1998; Braun *et al.*, 2001; Aki & Richards, 2002)

$$Q \equiv \frac{1}{\tan\zeta} = 2\pi\frac{W_{st}}{W_{dis}}, \tag{2.8}$$

where W_{st} is the maximum elastic stored energy during a cycle of loading at the frequency under consideration and W_{dis} is the energy dissipation per cycle.

The mechanical work done over time T is given by

$$W_{dis} = \int_T \tau d\varepsilon. \tag{2.9}$$

Using equation 2.9, W_{dis} can be calculated by integrating the out-of-phase component of stress over an entire cycle (Gray, 1972; Nowick & Berry, 1972; Chow, 1995; Braun *et al.*, 2001):

$$W_{dis} = \int_0^{2\pi/\omega} (\tau_0^I \sin\omega t)(-\varepsilon_0\omega\sin\omega t)\, dt, \tag{2.10}$$

$$= -\pi\tau_0^I\varepsilon_0, \tag{2.11}$$

$$= -\pi c^I\varepsilon_0^2. \tag{2.12}$$

Equation 2.12 can be interpreted to imply that the energy supplied to the material by the out-of-phase components is irreversibly converted to heat. Similarly, integration of the in-phase components over the full cycle yields zero work, implying that energy associated with the in-phase components is reversible, so there is no loss of energy for the in-phase components over a full cycle. The maximum energy stored by the in-phase components

occurs at a quarter of the cycle and is calculated as (Gray, 1972; Nowick & Berry, 1972)

$$W_{st} = \int_0^{\pi/2\omega} (\tau_0^R \cos\omega t)(-\varepsilon_0 \omega \sin\omega t)\, dt, \tag{2.13}$$

$$= -\frac{1}{2}\tau_0^R \varepsilon_0, \tag{2.14}$$

$$= -\frac{1}{2} c^R \varepsilon_0^2. \tag{2.15}$$

Substituting equations 2.12 and 2.15 into equation 2.8, I get

$$Q = \frac{1}{\tan\zeta} = \frac{c^R}{c^I}. \tag{2.16}$$

As mentioned above, we use this definition (equation 2.16) of Q in our analysis, which is also the standard definition of Q used in physics, classical mechanics, engineering, and material science. The above definition of Q is valid for any strength of attenuation; Q is infinite for purely elastic materials and vanishes for completely attenuative materials.

For torsion rectangular tests, the shear modulus is given by (e.g., Zhang *et al.*, 2003)

$$|c| = \frac{ML}{BT^3\theta}\left(\frac{3 + 1.8(T/B)}{1 - 0.378(T/B)^2}\right), \tag{2.17}$$

where M is the torque in the torque transducer, θ is the shear angle of the motor, and L, B, and T denote the length, breadth, and thickness, respectively, of the rectangular sample. For the rheometer used in this study, the maximum error in the measured torque is 3.89×10^{-2} Nm, in θ is the 5×10^{-5} radians, and in the phase angle ζ it is 1×10^{-5} radians.

2.4 Rock Samples

I examine two shale samples from the Green River Formation in Colorado. One of them is a lean shale with a low organic content of about 5% and the other is rich in kerogen with a high organic content (approximately 30%, Figure 2.3). The lean shales are gray-colored because of the lack of kerogen in contrast to the kerogen-rich shales, which are brownish-black. The typical dimensions of the samples used in the study are $45 \times 12.8 \times 3.2$ mm.

For measuring shear-wave anisotropy, I cut samples along three orthogonal planes (Figure 2.4). I assume the shales to be transversely isotropic (TI), which has been established

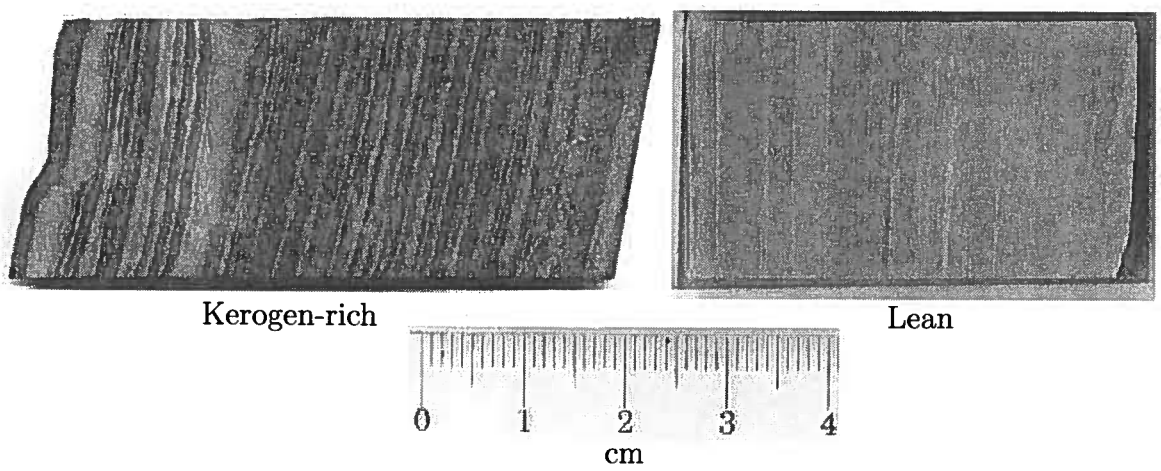

Figure 2.3: Shale samples used in the study. On the left is the dark organic-rich shale and on the right is the lean shale with little organic content.

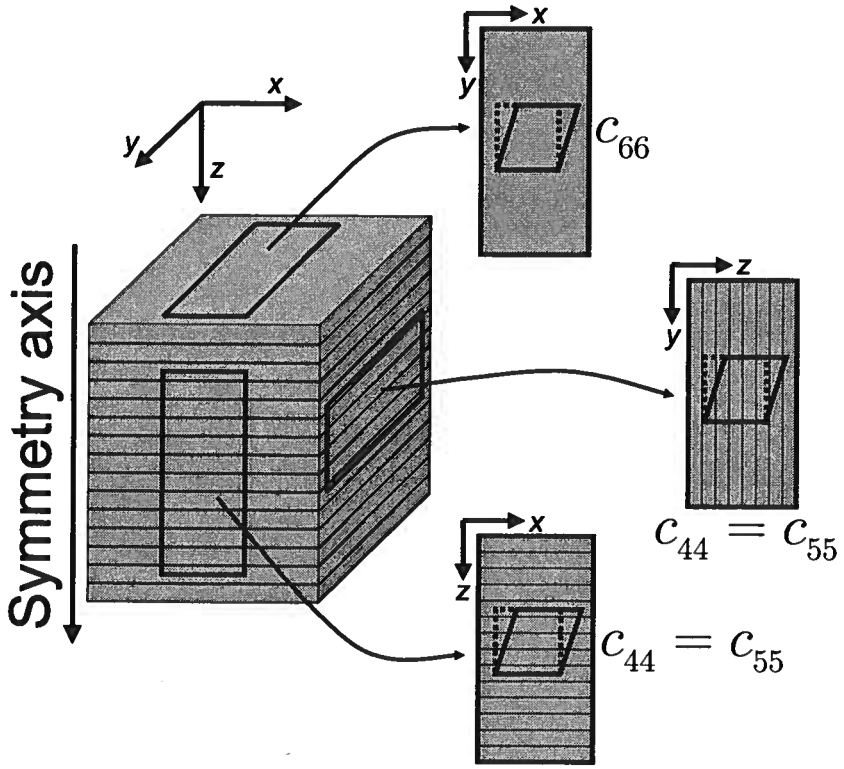

Figure 2.4: Shale samples cut in specific directions to measure $c_{44} = c_{55}$ and c_{66}.

in similar shales by many researchers (Vernik & Nur, 1992; Johnston & Christensen, 1996; Vernik & Liu, 1997; Carcione, 2000). A sample cut parallel to the symmetry axis is used to measure the complex stiffness $c_{44} = c_{55}$ (Figure 2.4). As the shale is TI, a sample cut in the vertical symmetry plane with its long axis orthogonal to the symmetry axis (Figure 2.4) would give $c_{44} = c_{55}$ as well (Thomsen, 1986; Tsvankin, 2005). A sample cut in the isotropy plane, as shown in Figure 2.4, is used to estimate c_{66}.

The shales are examined under temperatures ranging from 30°C to 350°C at equal intervals of 20°C. To understand the dispersion behavior, the sample is analyzed for frequencies ranging from 0.01 to 80 Hz (with increments of 0.1 on the $\log_{10}$ scale) at each temperature. All measurements are made in the linear viscoelastic regime, which is tested by conducting a strain-sweep experiment designed to measure the modulus of the rock for increasing strain amplitudes. Within the linear viscoelastic regime, the modulus does not change; and a strain amplitude lying within this linear region is selected for conducting all other temperature-frequency measurements of the rock. For the shales, we use strains between 6×10^{-5} to 8×10^{-5}. Note that this strain amplitude is larger than the strains encountered in exploration seismology [about 10^{-6}; Winkler *et al.* (1979)].

As pointed out by Iwasaki *et al.* (1978), higher strain amplitudes might result in lower moduli. To verify the validity of this statement, further experiments should be carried out at lower strain amplitudes using more sensitive equipment. We should, however, remember that this strain limit for linear behavior varies from one rock to another. For the time being, we assume that the higher strain does not significantly change the modulus, and the relaxation mechanisms remain the same. The measurements are carried out under a variable applied axial stress, which does not allow the sample to expand vertically. This is similar to reservoir recovery conditions where the shale is heated but its expansion is restricted.

2.5 Kerogen-rich Shale

Figures 2.5a and 2.5b show the real part of the stiffness c_{55} and the quality factor Q_{55}, respectively. The real part of c_{66} and Q_{66} are shown in Figure 2.6. Here and in the experiments below, the data have not been smoothed and are presented as collected, without any processing.

Frequency dispersion is relatively weak in these kerogen-rich shales, as evident from the small change in c_{55}^R and c_{66}^R with frequency (Figures 2.5a and 2.6a). Both storage moduli

(c_{55}^R and c_{66}^R) increase with frequency, even though the increase is small, with the most noticeable change occurring in the vicinity of 150°C. Attenuation in the directions both parallel and perpendicular to the bedding is also weakly dependent on frequency, with an attenuation peak near 150°C. At higher temperatures, however, attenuation decreases with frequency.

Both moduli (c_{55}^R and c_{66}^R) and quality factors (Q_{55} and Q_{66}) show a marked change with temperature [also observed in typical inorganic shales by Johnston (1987)]. Figure 2.7 shows a comparison of the elastic moduli and attenuation (along the two directions) for 0.3 Hz. Both moduli (c_{55}^R and c_{66}^R) drop steadily with temperature until it reaches 200°C. The drop in c_{55}^R is more pronounced that that in c_{66}^R. With further increase in temperature, c_{55}^R rises, reaches a maximum, and then drops again. In contrast, c_{66}^R shows relatively little change for temperatures greater than $\approx$ 200°C.

The change in both Q_{55} and Q_{66} with increasing temperature follows a similar pattern. They drop from about 40 at room temperature to below 5 at 150°C, then increase with temperature with s small drop near 300°C.

2.5.1 Attenuation Mechanisms

Since kerogen is viscoelastic, at low frequencies the molecules/chains have enough time to come to equilibrium, resulting in a low storage modulus. In contrast, at relatively higher frequencies the molecules/chains do not have sufficient time to relax as they are tangled and "locked," thereby making the material stiffer (high c^R), as there is a more efficient transfer of mechanical energy between the molecules/chains. Also, at low frequencies the material has sufficient time to relax almost completely as the molecules/chains slide past each other, which minimizes the energy loss (high Q). The "locking" of the molecules/chains at higher frequencies translates into a high value of Q, as relative sliding is inhibited which lowers frictional loss. For intermediate frequencies, however, the molecules/chains have the maximum slip during a cycle of loading, leading to the maximum frictional loss of energy.

The same mechanism is observed by Behura *et al.* (2007) in heavy oils and is similar to the maximum dielectric loss occurring at molecular resonant frequencies (Strobl, 1997). Here, an analogy can be drawn with the Maxwell model comprised of a spring and a dashpot in series. At high frequencies, the dashpot has little time to move, and thus the system responds elastically (high Q). At intermediate relaxation frequencies, the vibration frequency matches the rate of movement of the piston in the dashpot, resulting in the

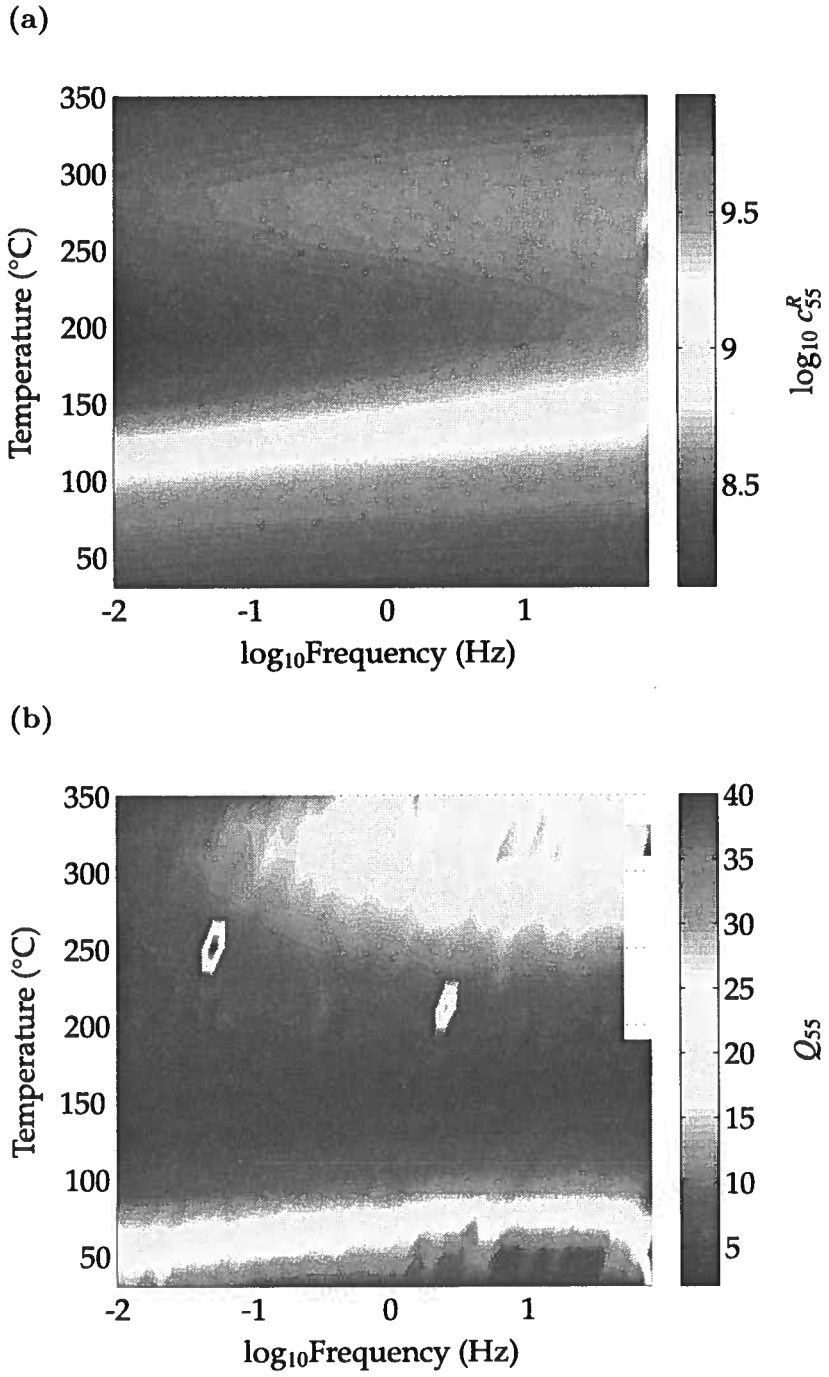

Figure 2.5: Real part of the shear modulus c_{55}^R (a) and the quality factor Q_{55} (b) of the kerogen-rich shale.

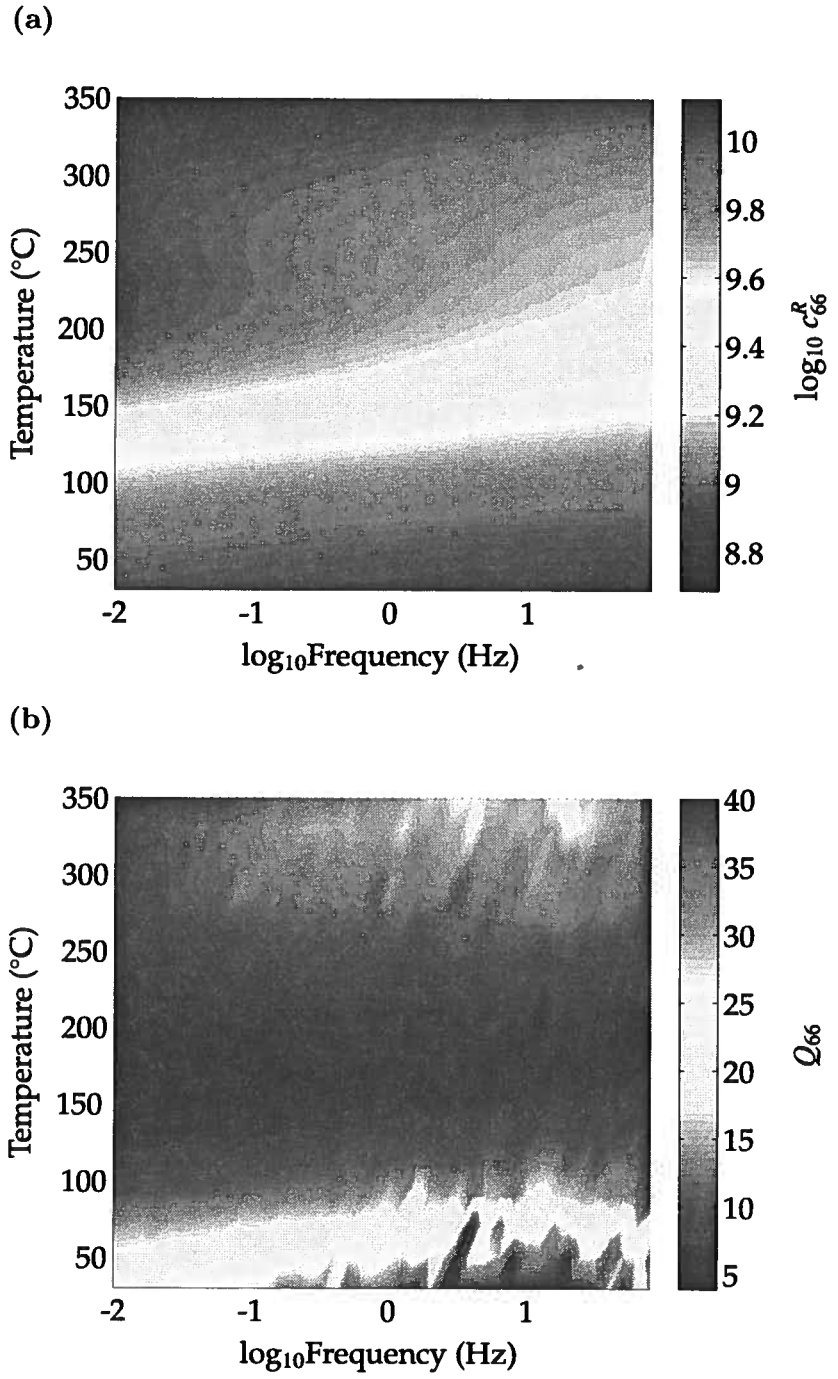

Figure 2.6: Real part of the shear modulus c_{66}^R (a) and the quality factor Q_{66} (b) of the kerogen-rich shale.

maximum energy loss (low Q). When the system is vibrated at a low frequency, the piston moves by the same amount as for the resonant frequencies. However, because the time period of each cycle is now long, most of the cycle is dominated by elastic movement of the spring (after the piston in the dashpot has passed the point of the maximum displacement). This results in a relatively large storage energy compared to the dissipated energy (high Q).

At low temperatures ($< 100°C$) the kerogen is close to a solid but melts with further increase in temperature and is eventually volatilized for temperatures exceeding 200°C. Because the rock is dry and the kerogen is still close to a solid for temperatures less than 100°C, Coulomb frictional dissipation owing to relative motion at grain boundaries (Walsh, 1966) or at interfaces between mineral and kerogen surfaces dominates fluid movement. Since frictional sliding is the dominant attenuation mechanism at these low temperatures, the moduli and quality factors show a weak frequency dependence (Johnston & Toksöz, 1981). At intermediate temperatures (100°C - 200°C), however, the contribution of fluid movement to attenuation increases because the kerogen melts. Whether it is attributable to viscous relaxation of the fluid or to "squirting" of the fluid in the cracks can possibly be determined by computing the crack aspect ratio, as suggested by O'Connell & Budiansky (1977). For temperatures larger than 200°C, the kerogen is altered and partially expelled, thereby increasing the stiffness and decreasing any frictional losses as well, as evident from the increase in Q (Figures 2.5b and 2.6b). Because of the lack of fluids in the shale at these high temperatures, frictional sliding is the dominant attenuation mechanism, as corroborated by the weak frequency dependence of the moduli and quality factors.

2.5.2 Anisotropy

Shales are usually laminated and therefore commonly transversely isotropic (Wang, 2002). Any change in the weaker layers comprising the shale will have a greater influence on the properties measured along the bedding-perpendicular direction compared to the bedding-parallel direction. Carcione (2000) suggests that the stiffness c_{55} is primarily controlled by the isotropic kerogen (compliant material) in the shales while c_{66} is dominated by the clay (stiff material) in the layering. Thus, any change in the physical state of the kerogen would be reflected in c_{55}, while the alterations in the clay layering would show up in c_{66}. The liquefaction of the kerogen with heating and its subsequent evaporation explains the initial rapid drop in c_{55}^R followed by an increase for temperatures above 200°C (Figure 2.5). The modulus c_{66}^R (Figure 2.6), on the other hand, drops steadily with increasing

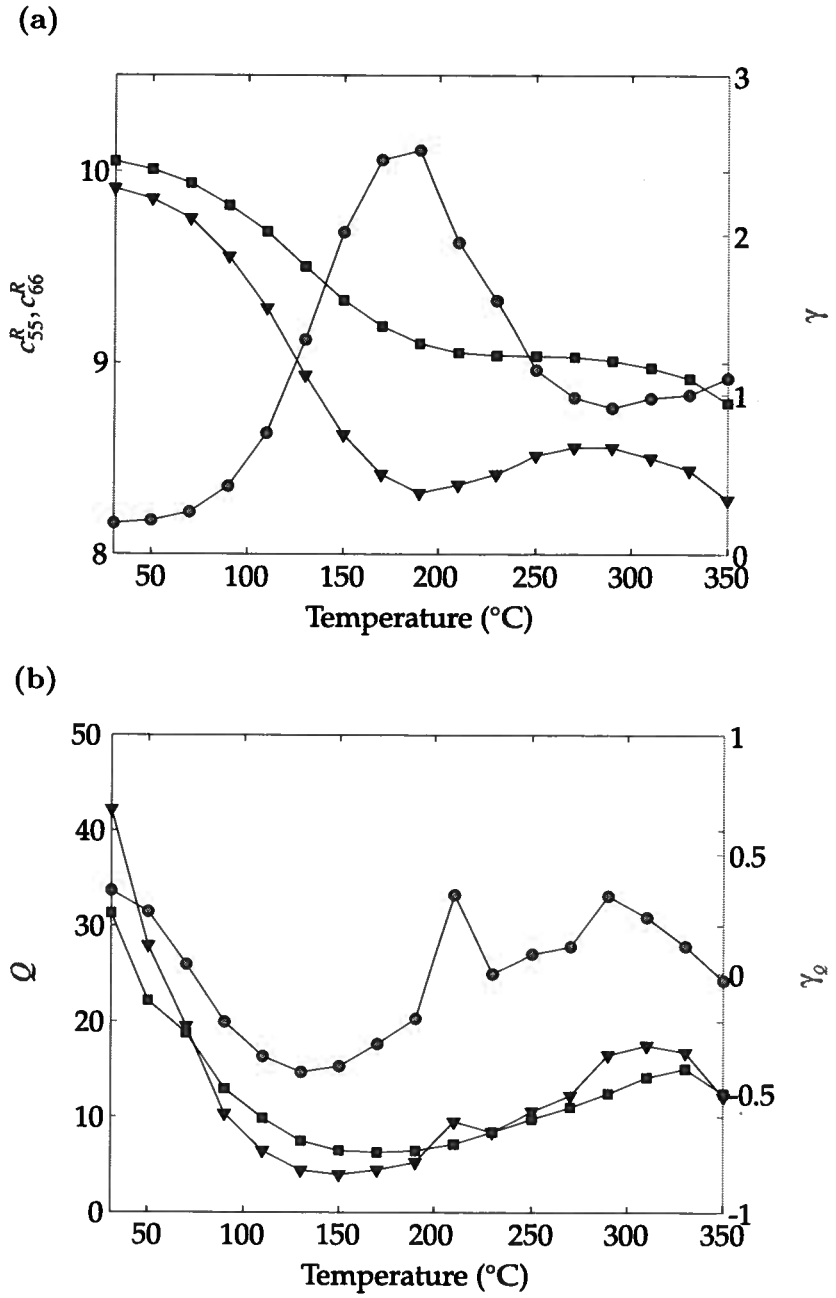

Figure 2.7: (a) The moduli c_{55}^R (triangles) and c_{66}^R (squares) and the velocity-anisotropy parameter γ (circles) of the kerogen-rich shale at a frequency of 0.3 Hz. (b) The quality factors Q_{55} (triangles) and Q_{66} (squares) and the attenuation-anisotropy parameter γ_Q (circles) at the same frequency.

temperature, which points to the possibility that the clay minerals are undergoing certain physical and chemical changes but no phase changes. It is also possible that the constituents of the clay layers include some kerogen which also contributes to the drop in c_{66}^R.

The difference in the moduli and attenuation along the bedding-parallel and bedding-perpendicular directions can be conveniently represented using Thomsen's SH-wave velocity-anisotropy parameter γ (Thomsen, 1986) and the SH-wave attenuation-anisotropy parameter γ_Q (Zhu, 2006) defined as the fractional difference between the SH-wave velocities and attenuation coefficients $\mathcal{A}$, respectively, in the directions orthogonal and parallel to the symmetry axis:

$$\gamma = \frac{c_{66}^R - c_{55}^R}{2c_{55}^R}, \tag{2.18}$$

$$\gamma_Q = \frac{\mathcal{A}_{66} - \mathcal{A}_{55}}{\mathcal{A}_{55}} = \frac{Q_{55} - Q_{66}}{Q_{66}}. \tag{2.19}$$

Parameters γ and γ_Q for the whole frequency and temperature range are shown in Figures 2.8a and 2.8b. SH-wave velocity anisotropy can be anomalously strong, with γ attaining values as large as three; attenuation anisotropy can also be significant, with γ_Q values approaching two. For typical shales, γ does not exceed 0.5 (Wang, 2002), which is significantly lower than the maximum value of γ observed here. Note that the sign of γ_Q can change as well.

The weak frequency dependence of c_{55} and c_{66} translates into a generally weak variation of γ and γ_Q with frequency. The parameter γ_Q, however, shows a moderate dependence on frequency for temperatures above 300°C.

Temperature, on the other hand, has a marked influence on both γ and γ_Q (Figures 2.7). The change in γ with temperature arises from the difference in the behavior of c_{55}^R and c_{66}^R. As the kerogen melts with increasing temperature, c_{55}^R drops more significantly compared to c_{66}^R, resulting in a jump in γ. The peak in γ corresponds to the maximum amount of melt in the shale. With further increase in temperature, kerogen starts evaporating, which results in a drop in γ as the shale becomes less compliant, which increases c_{55}^R but not c_{66}^R (Figure 2.7a). Therefore, the parameter γ could be used as an indicator of the physical state of kerogen in shales. Note that the velocity-anisotropy parameter γ changes by a factor of 10 (Figure 2.8a), which should be detectable in 4D studies.

The initial drop in γ_Q (Figure 2.8b) corresponds to the melting of the kerogen. Sub-

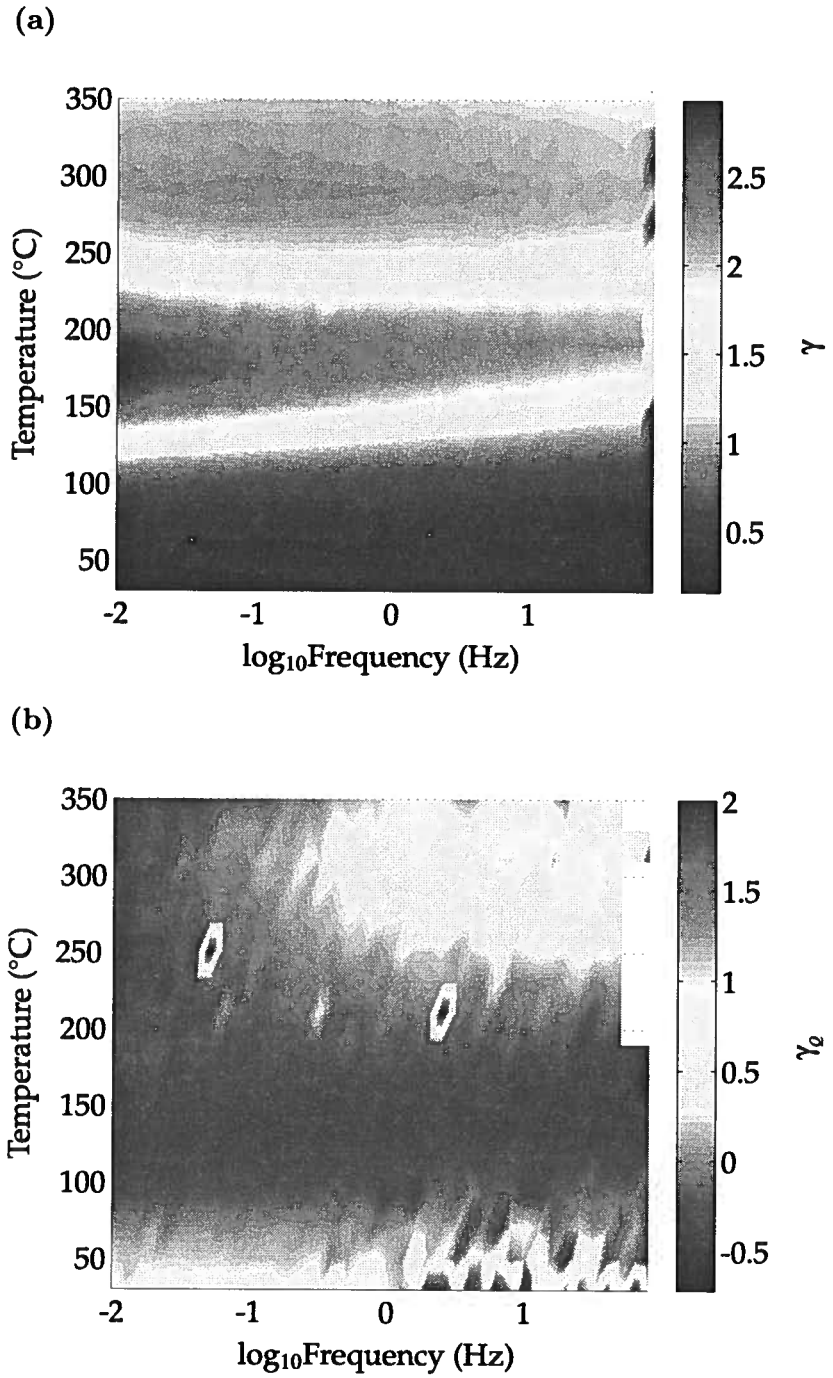

Figure 2.8: The SH-wave (a) velocity anisotropy parameter γ, and (b) attenuation anisotropy parameter γ_Q in the kerogen-rich shale.

sequently, as the kerogen starts evaporating, Q_{55} also increases, resulting in an increase in γ_Q. As with velocity anisotropy, attenuation anisotropy also shows a large change with temperature, which could have a substantial influence on SH-wave propagation. Although the change in γ_Q is not as prominent as in γ, it is high enough to be detectable in seismic data.

2.6 Lean Shale

The moduli c_{55}^R and c_{66}^R of the lean shale and their corresponding quality factors are shown in Figures 2.9 and 2.10. The temperature and frequency trends observed for the lean shale are similar to those described above for the kerogen-rich shale. The moduli of the lean shale, however, are larger than those of the kerogen-rich shale because of the lower content of the more compliant kerogen.

The low organic content is also responsible for the weak frequency dispersion in the lean shales (Figures 2.9a and 2.10a). The increase in both moduli is not significant, especially within the seismic band. Attenuation also shows a weak dependence on frequency (Figure 2.9b), which implies that friction may be the dominant attenuation mechanism. Although other mechanisms like "squirt flow" of fluids and viscous relaxation might also be present (notably in the vicinity of 150°C), additional experiments are needed to fully understand their role.

As with the kerogen-rich shales, the modulus c_{55}^R of the lean shales is more sensitive to temperature changes than is c_{66}^R. The initial drop in c_{55}^R is most probably due to the liquefaction of the small amount of kerogen sandwiched between clay layers. The liquefaction of kerogen not only softens the rock, reducing c_{55}^R, but also sharply decreases the quality factor Q_{55} (Figure 2.9b). This is because the liquid kerogen facilitates sliding, thereby decreasing the efficiency of transfer of mechanical energy between clay particles and increasing frictional loss. With further heating above 200°C, the lighter kerogen components evaporate, making the shale stiffer. The quality factor Q_{55} also increases as the frictional sliding between the clay layers is reduced. Again, only c_{55} and not c_{66} is expected to be influenced, which is clear from Figures 2.9 and 2.10. The changes in c_{66} and Q_{66}, on the other hand, are primarily because of physical and chemical alterations to the clay minerals which explains the steady drop in c_{66} and attenuation with temperature.

The effect of melting of kerogen and its subsequent evaporation is more apparent in the behavior of the anisotropy parameter γ (Figure 2.11). With melting of kerogen, γ increases

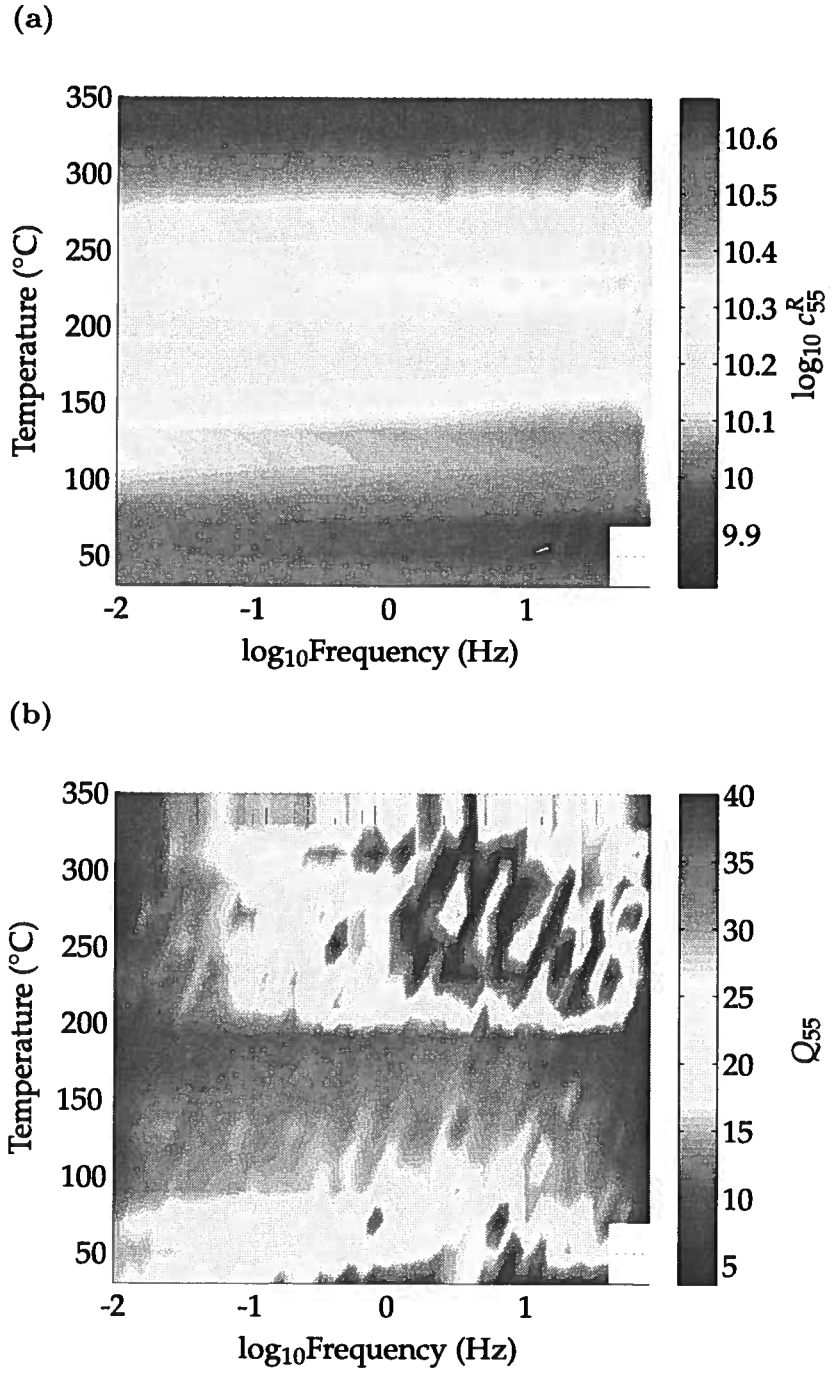

Figure 2.9: Real part of shear modulus c_{55}^R (a) and the quality factor Q_{55} (b) of the lean shale.

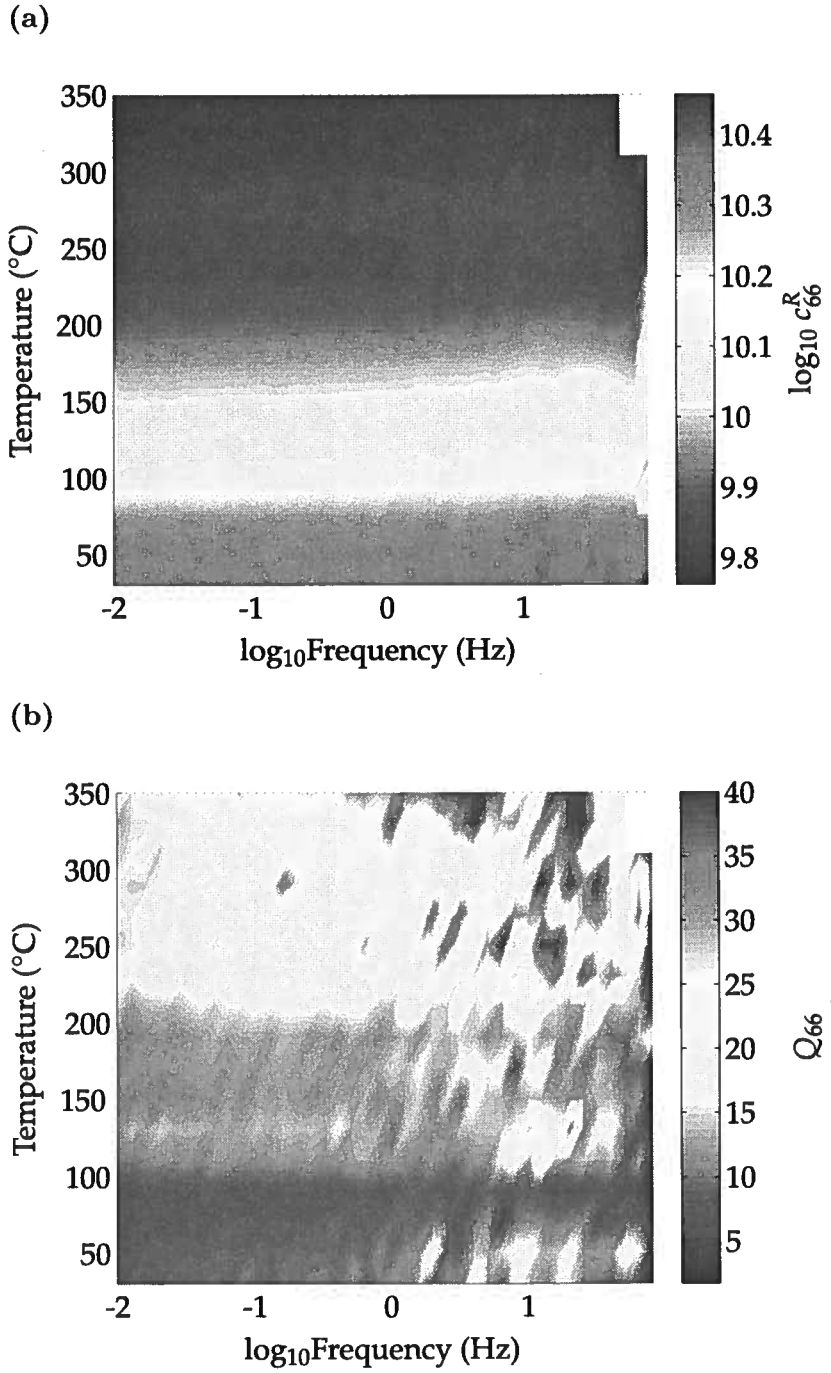

Figure 2.10: Real part of shear modulus c_{66}^R (a) and the quality factor Q_{66} (b) of the kerogen-rich shale.

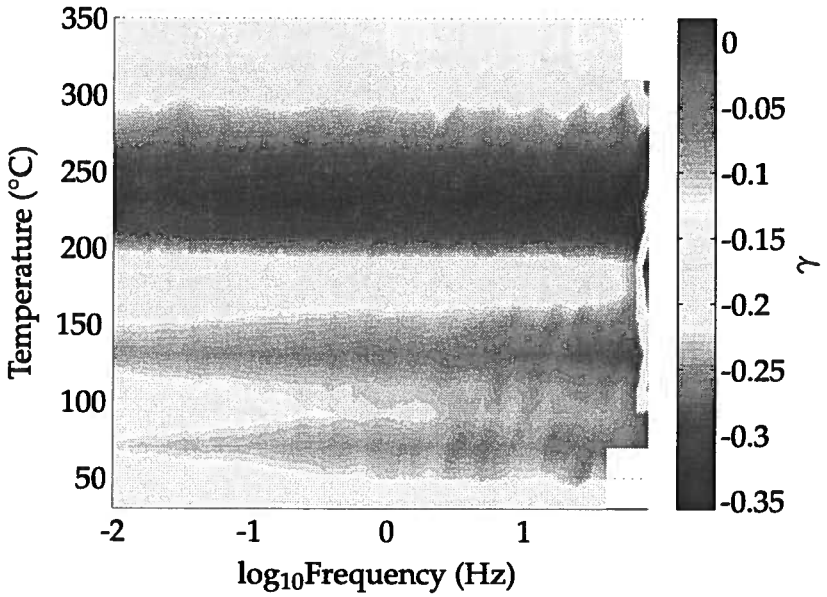

Figure 2.11: SH-wave velocity-anisotropy parameter γ of the lean shale.

as the difference between the moduli (c_{55}^R and c_{66}^R) grows. Above 200°C, the drop in γ is caused by the loss of kerogen.

2.7 Discussion

This experiment also demonstrates the contribution of lamination to the strength of anisotropy in TI media. Bakulin (2003) shows that the effect of layering on TI anisotropy is of second order compared to that of intrinsic anisotropy, but if the elastic contrast between the different layers is large, the layer-induced anisotropy can be significant. At room temperatures, the kerogen is solid and the contrast in the shear modulus of the solid clay (and carbonate) layers and the kerogen layers is not significant. This results in a low value of γ at room temperatures (Figure 2.8a). With increase in temperature, the kerogen progressively melts, thereby increasing the contrast between the layers, which results in a notable increase in γ.

2.8 Conclusions

Unlike common fluids (e.g. brine and light oil), kerogens in oil shales act as solids at room temperatures and fluids at higher temperatures. In other words, at room temperature, kerogens support a shear wave, while at higher temperatures the shear modulus approaches zero. Kerogens, however, have a non-zero bulk modulus at all temperatures, and the percentage change in the bulk modulus should be smaller compared to the change in the shear properties. So shear information can be more diagnostic of physical changes than bulk modulus properties, which makes acquisition of multicomponent seismic data all the more important. Our shear-wave measurements, made for a wide range of temperatures, simulate conditions encountered during in-situ steam flooding of oil shale reservoirs. Moreover, as shales are effectively viscoelastic, their properties in the seismic band are significantly different from those in the logging-frequency and ultrasonic bands. In the absence of strong heterogeneity, the shear properties acquired at frequencies ranging from 0.01 to 80 Hz (which includes the seismic band), should be close to the seismic properties of oil shales in the field.

The negligible frequency variation of the moduli and attenuation within the seismic bandwidth makes application of frequency-dependent analysis unlikely. Most of the existing methods for Q estimation from field data assume a constant Q within the seismic bandwidth, an approximation confirmed by our laboratory measurements.

Oil shales show a strong dependence of the rigidity moduli and attenuation on temperature. Heating melts the kerogen, which reduces the shear-wave velocity significantly, by a factor of five in some cases. The shear-wave quality factor can also drop by a factor of 10 over the range from room temperature to about $\approx 150°$C. Therefore, reservoir areas affected by heat should show a noticeable drop in velocities accompanied by a significant increase in attenuation. Such differences should be clearly visible on amplitudes and traveltimes of shear waves.

Heating of oil shales also substantially alters their velocity and attenuation anisotropy. The SH-wave velocity-anisotropy parameter γ could attain anomalously large values approaching three. The change in the attenuation-anisotropy parameter γ_Q can also be substantial. Since the melting of kerogen manifests itself in an increase in γ, while the loss of kerogen reduces γ, this parameter could be used as an indicator of the degree of kerogen melt in shales. SH-wave velocity and attenuation anisotropy could also be used to identify heated compartments of the reservoir.

Comparison of the kerogen-rich and lean shales indicates that the temperature dependence of shale properties is closely related to its organic content. Lean-shales have higher storage moduli and a higher Q than more organic-rich shales. Also, the temperature-related change in velocity and attenuation anisotropy is greater in shales richer in organic content. This can potentially be used to estimate the organic content of shales from seismic data.

Thus, this suite of measurements should be directly applicable to seismic analysis of oil-shale reservoirs during their exploration, development, and production. The high sensitivity of shear properties of oil shales to temperature makes 4D multicomponent seismic analysis of these reservoirs promising.

Chapter 3

The mystery of the inhomogeneity angle

3.1 Summary

The inhomogeneity angle (the angle between the real and imaginary parts of the wave vector) is seldom taken into account in estimating attenuation coefficients from seismic data. Wave propagation through the subsurface, however, can result in relatively large inhomogeneity angles ξ, especially for models with significant attenuation contrasts across layer boundaries. Here, I study the influence of the angle ξ on phase and group attenuation in arbitrarily anisotropic media using the first-order perturbation theory verified by exact numerical modeling.

Application of the spectral-ratio method to transmitted or reflected waves yields the normalized group attenuation coefficient $\mathcal{A}_g$, which is responsible for the amplitude decay along seismic rays. Our analytic solutions show that for a wide range of inhomogeneity angles the coefficient $\mathcal{A}_g$ is close to the normalized *phase* attenuation coefficient $\mathcal{A}$ computed for $\xi = 0^\circ$ ($\mathcal{A}|_{\xi=0^\circ}$). The coefficient $\mathcal{A}|_{\xi=0^\circ}$ can be inverted directly for the attenuation-anisotropy parameters, so no knowledge of the inhomogeneity angle is required for attenuation analysis of seismic data. This conclusion remains valid even for uncommonly high attenuation with the quality factor Q less than 10 and strong velocity and attenuation anisotropy. However, the relationship between the group and phase attenuation coefficients becomes more complicated for relatively large inhomogeneity angles approaching so-called "forbidden directions." I also demonstrate that the velocity function remains practically independent of attenuation for a wide range of small and moderate angles ξ.

In principle, estimation of the attenuation-anisotropy parameters from the coefficient $\mathcal{A}|_{\xi=0^\circ}$ requires computation of the phase angle, which depends on the anisotropic velocity field. For moderately anisotropic models, however, the difference between the phase and group directions should not significantly distort the results of attenuation analysis.

3.2 Introduction

In attenuative media, the direction of maximum attenuation of a plane wave can differ from the propagation direction. This implies that the real part of the wave vector $\mathbf{k}^R$ ("propagation vector") deviates from the imaginary part $\mathbf{k}^I$ ("attenuation vector"), as illustrated in Figure 3.1. The angle between the vectors $\mathbf{k}^R$ and $\mathbf{k}^I$ is called the "inhomogeneity angle," denoted here by ξ. When $\xi = 0°$, the plane wave is often characterized as "homogeneous;" when $\xi \neq 0°$, it is called "inhomogeneous." For plane-wave propagation, ξ represents a free parameter except for certain "forbidden directions" (Krebes & Le, 1994; Carcione & Cavallini, 1995; Červený & Pšenčík, 2005a,b) where solutions of the wave equation do not exist. If the wavefield is excited by a point source, the inhomogeneity angle is determined by the medium properties including the boundary conditions (Zhu, 2006; Vavryčuk, 2007).

Alternatively, the wave vector in attenuative media can be parameterized in terms of the "inhomogeneity parameter" D (Boulanger & Hayes, 1993; Declercq *et al.*, 2005; Červený & Pšenčík, 2005a):

$$\mathbf{k} = \omega(\sigma\mathbf{n} + iD\mathbf{m})\,, \tag{3.1}$$

such that

$$\mathbf{m} \cdot \mathbf{n} = 0\,, \tag{3.2}$$

where D is real, while σ is complex. The vector $\mathbf{n}$ specifies the direction of wave propagation, while the vector $\mathbf{m}$ is orthogonal to it. The main advantage of this parameterization is that it eliminates forbidden directions from the solutions of the Christoffel equation (Červený & Pšenčík, 2005a).

Many results on attenuation analysis are obtained under the assumption that the inhomogeneity angle can be ignored (Hauge, 1981; Dasgupta & Clark, 1998; Zhu *et al.*, 2007b). For point-source radiation in homogeneous media, the influence of the inhomogeneity angle is indeed small, unless the medium is anomalously attenuative and anisotropic (Zhu, 2006; Vavryčuk, 2007).

During wave propagation in layered media, however, the angle ξ can attain significant values. For the model in Figure 3.2, the wave vector in the elastic cap rock is real, while that in the attenuative reservoir is complex. Because the projections of the incident (real)

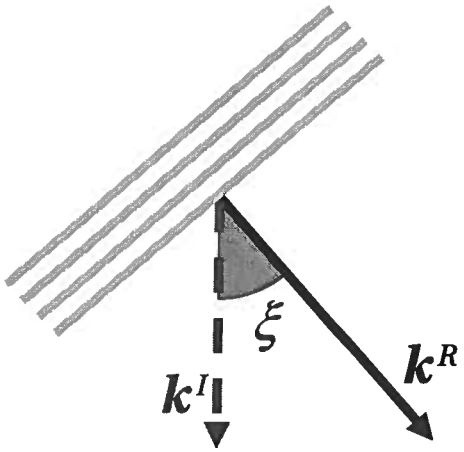

Figure 3.1: Plane wave with a nonzero inhomogeneity angle ξ. The wave propagates in the direction $\mathbf{k}^R$ (perpendicular to the planes of constant phase) and attenuates most rapidly in the direction $\mathbf{k}^I$.

and transmitted (complex) wave vectors onto the interface have to be the same according to Snell's law, the imaginary part $\mathbf{k}^I$ of the wave vector in the reservoir is orthogonal to the interface. This implies that the inhomogeneity angle of the transmitted wave is equal to the transmission angle, which can reach 90°. It is also clear that the inhomogeneity angle of the wave reflected from the base of the reservoir can be large as well. This situation, for example, is always encountered in soft absorbing sediments beneath the ocean bottom.

Existing measurements of the inhomogeneity angle are limited to laboratory studies (Deschamps & Assouline, 2000; Huang *et al.*, 1994). Indeed, although the angle ξ can be significant, its estimation from seismic data is extremely difficult. It seems natural to expect that the inhomogeneity angle should influence the attenuation along the raypath (group attenuation), which is the only relevant attenuation measurement in seismic processing.

Attenuation analysis becomes particularly involved in anisotropic media where the ray may significantly deviate from both the phase direction and the direction of maximum attenuation. When the medium is anisotropic, the relationship between the angle ξ and the attenuation coefficients is obscured by the complexity of the exact equations. It can be inferred from the work of Gajewski & Pšenčík (1992) that in weakly attenuative media the group attenuation coefficient yields the quality factor of the medium. Numerical modeling by Deschamps & Assouline (2000) also shows that group attenuation reflects the intrinsic

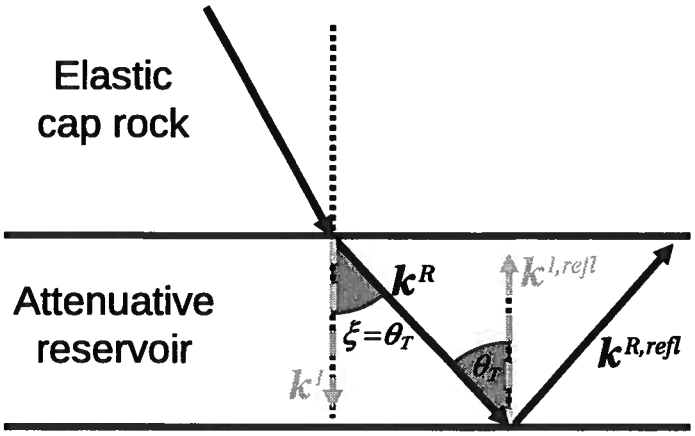

Figure 3.2: Illustration of the reflection/transmission problem at the interface between a purely elastic cap rock and an attenuative reservoir. $\mathbf{k}^R$ and $\mathbf{k}^I$ are the real and imaginary parts of the wave vector of the transmitted wave, while $\mathbf{k}^{R,refl}$ and $\mathbf{k}^{I,refl}$ correspond to the reflected wave. As discussed in the text, the inhomogeneity angle ξ of the transmitted wave is equal to the transmission angle θ_T.

viscoelasticity of the material. The analytic results of Vavryčuk (2008) and Červený & Pšenčík (2008a) indicate that group attenuation is insensitive to the inhomogeneity parameter. Their asymptotic analysis, however, is valid only for weak attenuation and plane waves with small values of the inhomogeneity parameter D.

Here, I use first-order perturbation theory to study the influence of the inhomogeneity angle on the group and phase attenuation coefficients. By perturbing an isotropic attenuative background, I obtain a weakly anisotropic medium with angular dependence of both velocity and attenuation. In contrast to the methodology of Červený & Pšenčík (2008a) and Vavryčuk (2008), our approach allows for arbitrarily large attenuation and "strongly inhomogeneous" waves. Therefore, this perturbation scheme helps us to analyze wave propagation for a wide range of angles ξ including the vicinity of forbidden directions. First, I develop closed-form linearized expressions for group and phase attenuation in arbitrarily anisotropic media, which provide useful physical insight into the influence of the angle ξ. The general equations are then simplified for the special case of TI media by expressing them through the Thomsen-style anisotropy parameters. Finally, the conclusions drawn from the analytic expressions are corroborated by exact numerical modeling.

3.3 Phase and Group Attenuation Coefficients

The Christoffel equation, which describes plane-wave propagation in anisotropic media, can be solved for the real (k^R) and imaginary (k^I) parts of the wave vector. The ratio k^I/k^R yields the phase attenuation per wavelength, which is called the normalized phase attenuation coefficient $\mathcal{A}$ (Zhu & Tsvankin, 2006):

$$\mathcal{A} = \frac{k^I}{k^R}. \tag{3.3}$$

For a nonzero inhomogeneity angle ξ, the coefficient $\mathcal{A}$ is a measure of attenuation along the vector $\mathbf{k}^I$ rather than $\mathbf{k}^R$. Also, in seismic data processing, the attenuation is measured along the raypath, which deviates from the phase direction $\mathbf{k}^R$ when the medium is anisotropic.

Attenuation is commonly computed from seismic data using the spectral-ratio method (e.g., Johnston & Toksöz, 1981; Tonn, 1991), which has been extended to anisotropic media (Zhu *et al.*, 2007b). If two receivers record the same event at two different locations along a raypath, the attenuation coefficient can be estimated from the ratio S of the measured amplitude spectra:

$$\ln S = \ln \mathcal{G} - k_g^I \, l, \tag{3.4}$$

where $\mathcal{G}$ contains the reflection/transmission coefficients, source/receiver radiation patterns, and geometrical spreading along the raypath, k_g^I is the average group attenuation coefficient, and l is the distance between the two receivers. Assuming that the medium between the receivers is homogeneous, equation 3.4 can be rewritten in terms of the group velocity V_g and traveltime t:

$$\begin{aligned} \ln S &= \ln \mathcal{G} - k_g^I \, V_g \, t, \\ &= \ln \mathcal{G} - \omega \, \mathcal{A}_g \, t, \end{aligned} \tag{3.5}$$

where ω is the angular frequency and $\mathcal{A}_g = k_g^I/k_g^R = k_g^I/(\omega/V_g)$ is the normalized group attenuation coefficient. It follows from equation 3.5 that by estimating the slope of $\ln S$ expressed as a function of ω, I can compute the group attenuation along the raypath, if the traveltime t is known. Therefore, $\mathcal{A}_g$ is the measure of attenuation obtained from seismic

data.

If the medium is anisotropic (or isotropic, but the inhomogeneity angle is large, as discussed below), the group-velocity vector $\mathbf{V}_g$ deviates from the phase direction parallel to $\mathbf{k}^R$. To simplify the analytic development, I choose a coordinate frame in which $\mathbf{k}^R$ coincides with the axis x_3 and $\mathbf{k}^I$ is confined to the $[x_1, x_3]$-plane (Figure 3.3). The group attenuation coefficient k_g^I can be found by projecting the phase attenuation vector $\mathbf{k}^I$ onto the group direction:

$$k_g^I = \frac{1}{V_g}\left(\mathbf{k}^I \cdot \mathbf{V}_g\right) , \tag{3.6}$$

$$= k^I(\cos\xi\cos\psi + \sin\xi\sin\psi\cos\phi) , \tag{3.7}$$

where ψ is the angle between $\mathbf{k}^R$ and $\mathbf{V}_g$ (group angle) and ϕ is the azimuth of $\mathbf{V}_g$ with respect to the $[x_1, x_3]$-plane (Figure 3.3). For isotropic media and symmetry planes in anisotropic media, $\mathbf{V}_g$ lies in the plane formed by the vectors $\mathbf{k}^R$ and $\mathbf{k}^I$ (i.e., $\phi = 0$), and k_g^I is given by

$$k_g^I = k^I\cos(\xi - \psi) . \tag{3.8}$$

Using equation 3.7, the normalized group attenuation coefficient $\mathcal{A}_g$ can be represented as

$$\mathcal{A}_g = \frac{k_g^I}{k_g^R} = \frac{k^I\cos\xi\cos\psi\,(1 + \tan\xi\tan\psi\cos\phi)}{\omega/V_g} . \tag{3.9}$$

The group velocity can be obtained from the well-known relation (e.g., Červený & Pšenčík, 2006):

$$\frac{1}{\omega}\,\mathbf{k}^R \cdot \mathbf{V}_g = 1 , \tag{3.10}$$

or

$$\frac{\omega}{V_g} = k^R\cos\psi . \tag{3.11}$$

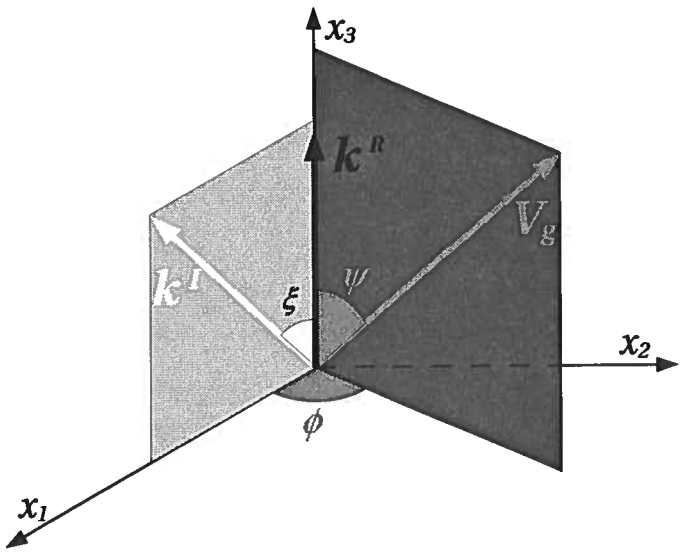

Figure 3.3: Plane wave propagating along the coordinate axis x_3 in an anisotropic attenuative medium. The group angle ψ is the deviation of the group velocity vector $\mathbf{V}_g$ from the real part $\mathbf{k}^R$ of the wave vector. The azimuth of the vector $\mathbf{V}_g$ with respect to the plane formed by $\mathbf{k}^R$ and $\mathbf{k}^I$ is denoted by ϕ.

Substituting equation 3.11 into equation 3.9 yields

$$\mathcal{A}_g = \frac{k^I}{k^R} \cos\xi \left(1 + \tan\xi \tan\psi \cos\phi\right). \tag{3.12}$$

Equation 3.12 can be used to compute the exact coefficient $\mathcal{A}_g$ for arbitrarily anisotropic, attenuative media and any angle ξ. If the group-velocity vector is confined to the plane formed by $\mathbf{k}^R$ and $\mathbf{k}^I$ (see above), $\cos\phi = 1$ and equation 3.12 becomes

$$\mathcal{A}_g = \frac{k^I}{k^R} \frac{\cos(\xi - \psi)}{\cos\psi}. \tag{3.13}$$

For a zero inhomogeneity angle, the coefficient $\mathcal{A}_g$ reduces to

$$\mathcal{A}_g(\xi = 0°) = \left.\frac{k^I}{k^R}\right|_{\xi=0°} = \mathcal{A}|_{\xi=0°}. \tag{3.14}$$

Equation 3.14 demonstrates that even for arbitrary anisotropy, the group attenuation coefficient coincides with the phase attenuation coefficient for $\xi = 0°$ (Zhu, 2006). It is unclear,

however, how $\mathcal{A}_g$ is related to phase attenuation for a nonzero ξ and what role is played by the inhomogeneity angle in the estimation of the attenuation coefficient.

3.4 Isotropic Media

To evaluate the influence of the inhomogeneity angle on velocity and attenuation in isotropic media, I obtain the real and imaginary parts of the vector $\mathbf{k}$ from the wave equation. The derivation, discussed in Appendix A, shows that the solution exists only if $\mathbf{k}^R \cdot \mathbf{k}^I > 0$, which means that the inhomogeneity angle in isotropic media should be smaller than 90° (I assume that $\xi > 0$ because positive and negative inhomogeneity angles are equivalent in the absence of anisotropy). Therefore, the attenuation vector $\mathbf{k}^I$ cannot deviate from $\mathbf{k}^R$ by 90° or more, and angles $\xi \geq 90°$ correspond to so-called "forbidden directions." Note that for isotropic *non-attenuative* media, the inhomogeneity angle of an evanescent (inhomogeneous) plane wave is always equal to 90°, which explains the properties of surface and nongeometrical modes (Tsvankin, 1995).

The squared magnitudes of the vectors $\mathbf{k}^R$ and $\mathbf{k}^I$ for $\xi < 90°$ (Appendix A) are given by

$$(k^R)^2 = \frac{\omega^2}{2V^2}\left[\sqrt{1+\frac{1}{(Q\cos\xi)^2}}+1\right], \tag{3.15}$$

$$(k^I)^2 = \frac{\omega^2}{2V^2}\left[\sqrt{1+\frac{1}{(Q\cos\xi)^2}}-1\right], \tag{3.16}$$

where $V = \sqrt{a_{33}^R}$ is the real part of the medium velocity and a_{ij} is the density-normalized stiffness tensor. The only approximation used to derive equations 3.15 and 3.16 is that quadratic and higher-order terms in the inverse quality factor $1/Q$ [but not in $1/(Q\cos\xi)$] can be neglected compared to unity. Equivalent solutions for k^R and k^I in isotropic media are given in Červený & Pšenčík (2005a).

3.4.1 Small and Moderate Inhomogeneity Angles

The dependence of the wave vector on the inhomogeneity angle is controlled by the product $Q\cos\xi$. If the angle ξ is not close to 90° and the medium does not have uncommonly strong attenuation, I can assume that $(Q\cos\xi) \gg 1$ and simplify equations 3.15 and 3.16

to (see Appendix A)

$$k^R = \frac{\omega}{V}, \tag{3.17}$$

$$k^I = \frac{\omega}{2VQ\cos\xi}. \tag{3.18}$$

According to equation 3.17, for $(Q\cos\xi) \gg 1$ the velocity of wave propagation is equal to V and is independent of the inhomogeneity angle and of attenuation. Using equations 3.17 and 3.18, I find the normalized phase attenuation coefficient $\mathcal{A}$ as

$$\mathcal{A} = \frac{k^I}{k^R} = \frac{1}{2Q\cos\xi}. \tag{3.19}$$

In general, the inhomogeneity angle also influences the group velocity and the group angle. For $(Q\cos\xi) \gg 1$, however, the influence of ξ is negligible (Appendix A):

$$\tan\psi = \frac{\tan\xi}{1+2Q^2} \ll 1, \tag{3.20}$$

and $V_g \approx V$. The normalized group attenuation coefficient $\mathcal{A}_g$ (equation 3.12) then becomes

$$\mathcal{A}_g = \frac{k^I\cos\xi}{k^R}. \tag{3.21}$$

If the wave vector is described by equations 3.17 and 3.18, equation 3.21 yields

$$\mathcal{A}_g = \frac{1}{2Q} = \mathcal{A}|_{\xi=0^\circ}. \tag{3.22}$$

Therefore, for a wide range of common inhomogeneity angles, the group attenuation coefficient $\mathcal{A}_g$ does not depend on the angle ξ and is close to the phase attenuation coefficient $\mathcal{A}$ computed for $\xi = 0^\circ$. Later I demonstrate that this result remains valid for much more complicated models with anisotropic velocity and attenuation functions. Equation 3.22 also shows that seismic attenuation measurements (i.e., the coefficient $\mathcal{A}_g$) for isotropic media provide a direct estimate of the quality factor Q. This conclusion applies to both P- and S-waves and a wide range of angles ξ (Figure 3.4).

3.4.2 Large Inhomogeneity Angles

For large inhomogeneity angles approaching 90°, the assumption $(Q\cos\xi) \gg 1$ used to derive equations 3.17 and 3.18 is no longer satisfied. In the limit of $(Q\cos\xi) \ll 1$ $(\xi \to 90°)$, equations 3.15 and 3.16 give completely different approximate solutions for the wave vector (Appendix A):

$$k^R = \frac{\omega}{V\sqrt{2Q\cos\xi}}\left(1 + \frac{Q\cos\xi}{2}\right), \tag{3.23}$$

$$k^I = \frac{\omega}{V\sqrt{2Q\cos\xi}}\left(1 - \frac{Q\cos\xi}{2}\right). \tag{3.24}$$

Dropping quadratic and higher-order terms in $Q\cos\xi$, I find

$$\mathcal{A} = \frac{k^I}{k^R} = 1 - Q\cos\xi\,. \tag{3.25}$$

The velocity of wave propagation, determined by the denominator of the expression for k^R (equation 3.23), is proportional to $\sqrt{Q\cos\xi}$ and goes to zero when the inhomogeneity angle approaches 90°.

When $\xi \to 90°$, the influence of the inhomogeneity angle on the group quantities ψ, V_g, and $\mathcal{A}_g$ is no longer negligible. The group angle for large inhomogeneity angles becomes (Appendix A)

$$\tan\psi = \frac{1}{Q} - \cos\xi\,. \tag{3.26}$$

Equation 3.26 demonstrates that for strong attenuation (small Q) the group-velocity vector deviates from the phase direction toward the attenuation vector when $\xi \to 90°$. Note that despite the medium being isotropic, the group and phase directions differ because of nonzero values of ξ.

The coefficient $\mathcal{A}_g$ for large angles ξ can be obtained by substituting equations 3.25 and 3.26 into equation 3.12:

$$\mathcal{A}_g = (1 - Q\cos\xi)\left[\cos\xi + \left(\frac{1}{Q} - \cos\xi\right)\sin\xi\right]. \tag{3.27}$$

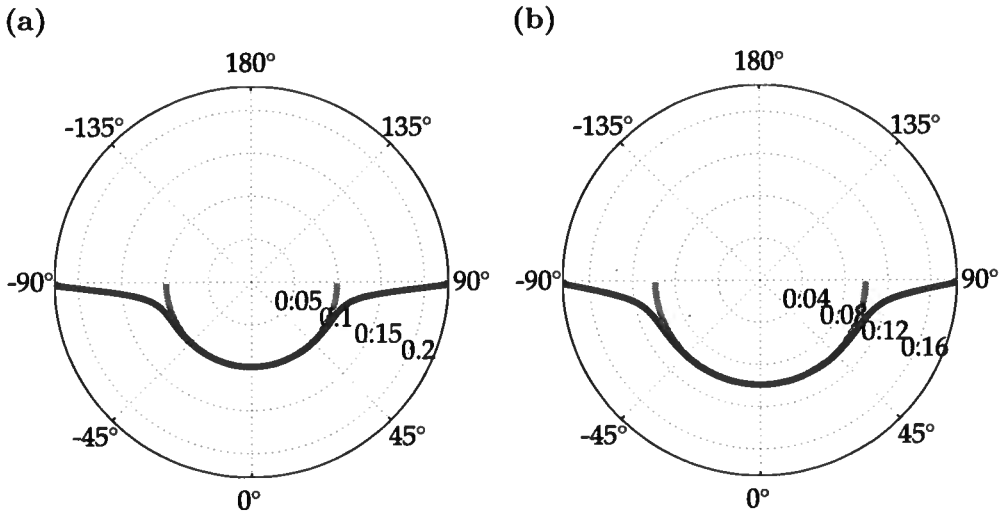

Figure 3.4: Exact P-wave (a) and S-wave (b) coefficient $\mathcal{A}|_{\xi=0^\circ}$ (equation 3.3, gray curve) and the normalized group attenuation $\mathcal{A}_g$ (equation 3.12, black curve) in isotropic media as a function of the inhomogeneity angle ξ (numbers on the perimeter). The quality factors are $Q_P = Q_S = 5$.

Linearizing equation 3.27 in $\cos\xi$ yields

$$\mathcal{A}_g = \frac{1}{Q} - \cos\xi\,. \tag{3.28}$$

Equation 3.28 shows that the group attenuation coefficient $\mathcal{A}_g$ for large inhomogeneity angles reduces to just $\tan\psi$ (see equation 3.26). Therefore, whereas the real and imaginary parts of the wave vector (equations 3.23 and 3.24) become infinite as $\xi \to 90^\circ$, the group attenuation coefficient approaches $1/Q$ and is about twice as large as $\mathcal{A}|_{\xi=0^\circ}$ (Figure 3.4). Hence, for large angles ξ close to 90°, seismic attenuation measurements in isotropic media *do not* provide a direct estimate of the quality factor because $\mathcal{A}_g$ rapidly increases with ξ from $1/(2Q)$ to $1/Q$.

Although the presence of anisotropy makes treatment of wave propagation in attenuative media much more complicated, several key conclusions drawn above prove to be valid for models with anisotropic velocity and attenuation functions.

3.5 Anisotropic Media

The dependence of attenuation on the inhomogeneity angle ξ in anisotropic media is influenced by the angular variation of the phase quantities and by the difference between the group and phase directions. Using the Christoffel equation B.1, the phase attenuation coefficient $\mathcal{A}$ can be computed for arbitrary values of the angle ξ. Then general group-velocity equations (e.g., Tsvankin, 2005) can be employed to obtain the group attenuation coefficient. It would be useful, however, to develop analytic expressions for phase and group attenuation that provide physical insight into the contribution of the inhomogeneity angle. To derive analytic expressions for $\mathbf{k}^R$, $\mathbf{k}^I$, and $\mathcal{A}_g$ in arbitrarily anisotropic media, I use the first-order perturbation theory, as discussed in Appendix B. The analytic development is supported by numerical modeling based on exact solutions.

3.5.1 Perturbation of the Complex Wave Vector

I consider an isotropic, attenuative background medium, which is perturbed to obtain anisotropic velocity and attenuation functions. The real and imaginary parts of the wave vector in the background are denoted by $\mathbf{k}^{R,0}$ and $\mathbf{k}^{I,0}$, respectively. I choose the coordinate frame in which $\mathbf{k}^{R,0}$ coincides with the x_3-axis and $\mathbf{k}^{I,0}$ lies in the $[x_1, x_3]$-plane. The angle ξ is kept fixed, so the real and imaginary parts of the perturbed wave vector $\mathbf{k} = \mathbf{k}^R - i\mathbf{k}^I$ remain parallel to the corresponding parts of the background vector $\mathbf{k}^0$.

First, I obtain linearized expressions for the perturbations Δk^R and Δk^I in arbitrarily anisotropic media using the coordinate frame defined by $\mathbf{k}^R$ and $\mathbf{k}^I$ (equations B.15–B.20). To express Δk^R and Δk^I in a fixed coordinate frame, one has to rotate the perturbation density-normalized stiffness tensor Δa_{ijkl} accordingly. For example, to derive Δk^R and Δk^I for TI media as a function of the phase angle θ (the angle between $\mathbf{k}^R$ and the symmetry axis), the tensor Δa_{ijkl} in equations B.15–B.20 is rotated about the x_2-axis by the angle θ.

For the special case of P-wave propagation in TI media, the perturbations Δk^R and Δk^I take the form

$$\frac{\Delta k_P^R}{k_P^{R,0}} = -\left(\delta \sin^2\theta \cos^2\theta + \epsilon \sin^4\theta\right), \tag{3.29}$$

$$\frac{\Delta k_P^I}{k_P^{I,0}} = \delta_Q \sin^2\theta \cos^2\theta + \epsilon_Q \sin^4\theta$$

$$- (\delta \sin^2\theta \cos^2\theta + \epsilon \sin^4\theta) - \left[\delta + 2(\epsilon - \delta)\sin^2\theta\right] \sin 2\theta \tan\xi\,, \qquad (3.30)$$

where ϵ and δ are the Thomsen velocity-anisotropy parameters, and ϵ_Q and δ_Q are the Thomsen-style attenuation-anisotropy parameters (Zhu & Tsvankin, 2006). The parameter ϵ_Q determines the fractional difference between the P-wave phase attenuation coefficients $\mathcal{A}|_{\xi=0^\circ}$ in the horizontal and vertical directions, while δ_Q controls the coefficient $\mathcal{A}|_{\xi=0^\circ}$ in the vicinity of the symmetry axis. Equations 3.29 and 3.30 are derived for the attenuation vector $\mathbf{k}^I$ confined to the plane defined by $\mathbf{k}^R$ and the symmetry axis. Similar expressions for SV- and SH-waves in TI media are given in Appendix C (equations C.1–C.4).

Note that the real part Δk^R of the linearized perturbation in the wave vector in equations 3.29, C.1, and C.3 is independent of the inhomogeneity angle and is entirely governed by velocity anisotropy. This conclusion is corroborated by the numerical example in Figure 3.5. As the inhomogeneity angle varies from 0° to 70°, there is no noticeable change in k^R even in the presence of velocity anisotropy (Figures 3.5c and 3.5d) and attenuation anisotropy (Figures 3.5e and 3.5f). The "isotropic" behavior of k^R in Figures 3.5e and 3.5f indicates that attenuation anisotropy has little influence on the velocity function, which is controlled by the velocity-anisotropy parameters (Figures 3.5c and 3.5d). Whereas equations 3.29, C.1, and C.3 remain accurate for a wide range of ξ (Figures 3.5b, 3.5d, and 3.5f) and strong attenuation anisotropy, they break down for the angle ξ approaching 90°.

The attenuation vector k^I (equations 3.30, C.2, and C.4), on the other hand, is influenced by both velocity and attenuation anisotropy, as well as by the inhomogeneity angle ξ. The increase in ξ from 0° to 70° in Figure 3.6 causes a substantial change in k^I, both for isotropic and TI media. Figures 3.6d–3.6i illustrate the dependence of k^I on the velocity- and attenuation-anisotropy parameters. It is interesting to note that for small ξ the contribution of velocity and attenuation anisotropy to k^I (equations 3.30, C.2, and C.4) is of the same order. With increasing ξ, however, the influence of velocity anisotropy (Figure 3.6f) becomes more pronounced compared to that of attenuation anisotropy (Figure 3.6i) because the $\tan\xi$-term in equation 3.30 depends just on ϵ and δ. Figure 3.6 also demonstrates that equation 3.30 deviates from the exact k^I only for large angles ξ, with the error primarily controlled by the velocity-anisotropy parameters.

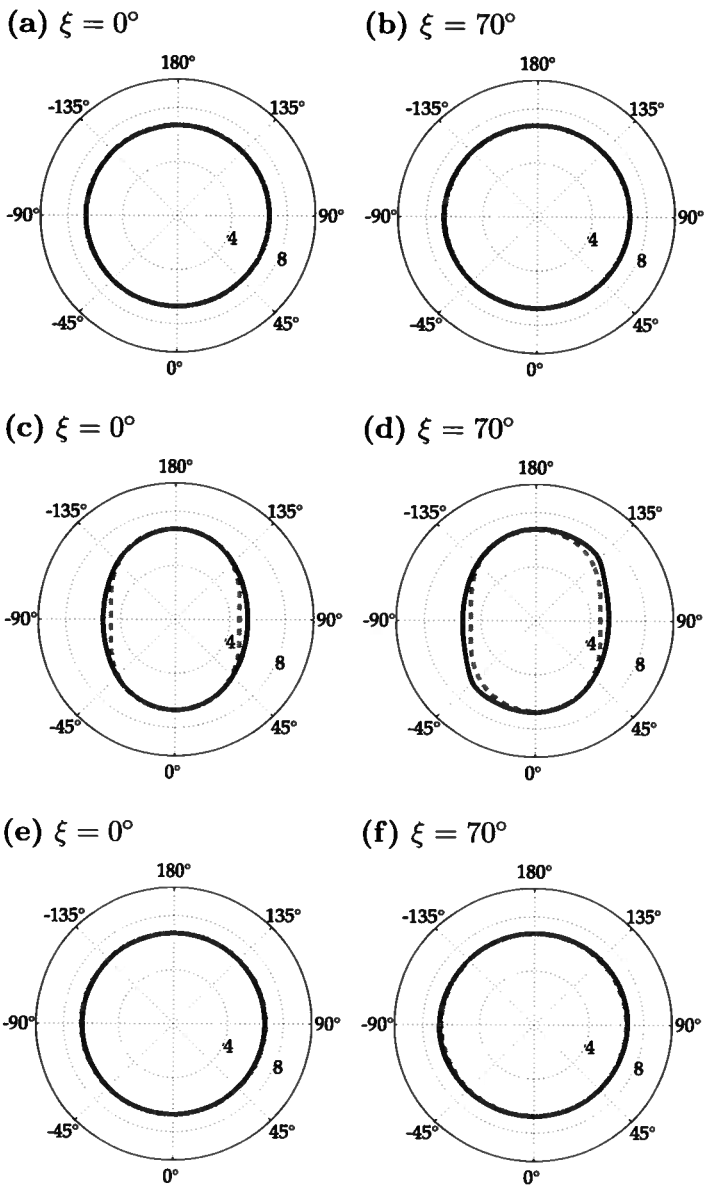

Figure 3.5: Exact real part k^R (in 100 m^{-1}) of the P-wave vector $\mathbf{k}$ (solid lines) and approximate $k^R = k^{R,0} + \Delta k^R$ from equation 3.29 (dashed lines) for $\xi = 0°$ (a,c,e) and $\xi = 70°$ (b,d,f) as a function of the phase angle (numbers on the perimeter). The model in (a,b) is isotropic; in (c,d) it is anisotropic in terms of velocity but has isotropic attenuation, while in (e,f) it has isotropic velocity and anisotropic attenuation (Table 3.1). The frequency is 30 Hz.

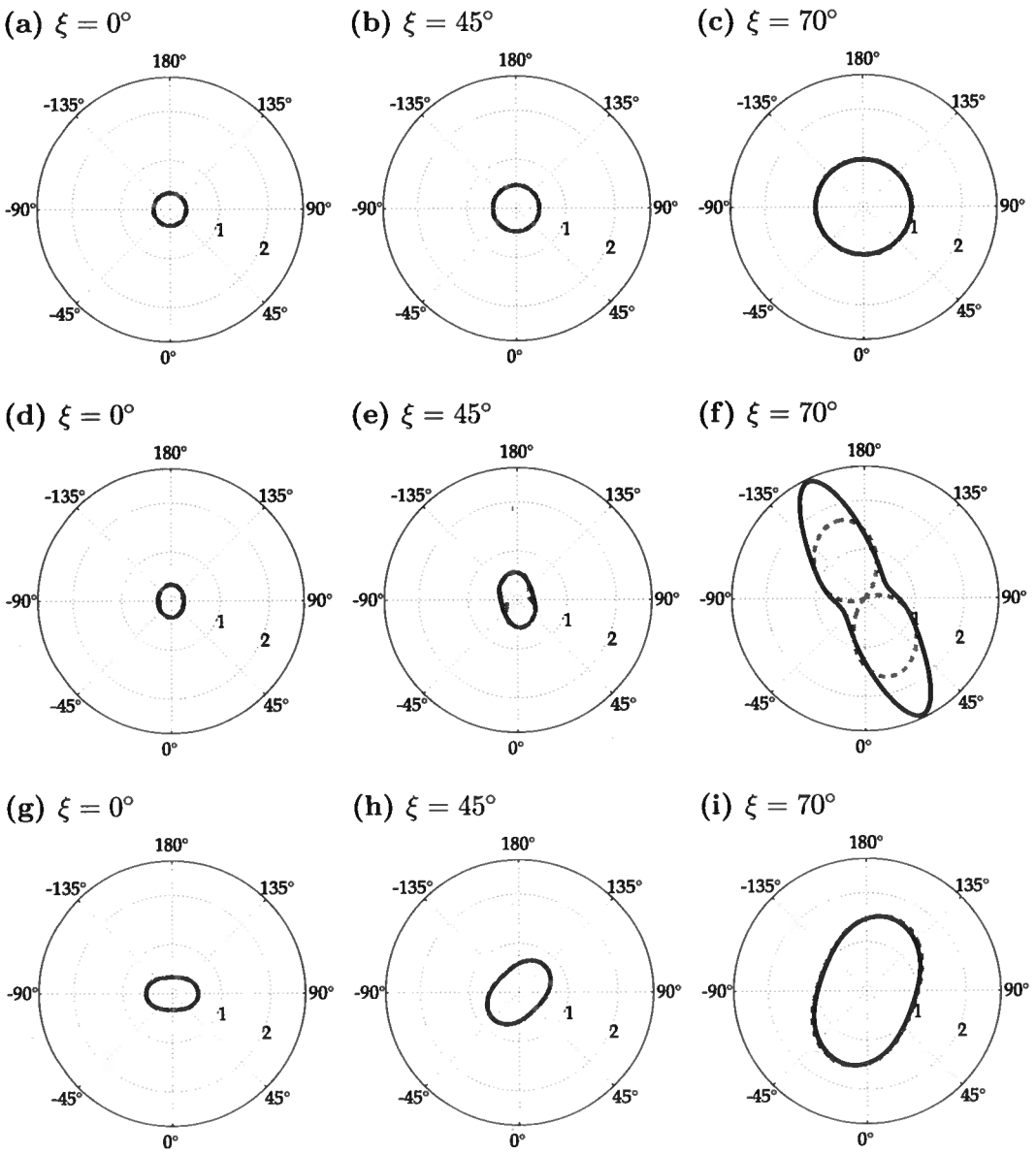

Figure 3.6: Exact imaginary part k^I of the P-wave vector $\mathbf{k}$ (solid lines) and approximate $k^I = k^{I,0} + \Delta k^I$ (in 100 m^{-1}) from equation 3.30 (dashed lines) for $\xi = 0°$ (a,d,g), $\xi = 45°$ (b,e,h) and $\xi = 70°$ (c,f,i) as a function of the angle between $\mathbf{k}^I$ and the symmetry axis. In (a,b,c) both velocity and attenuation are isotropic; in (d,e,f) only velocity varies with angle, while attenuation is isotropic; in (g,h,i) attenuation varies with angle, while velocity is isotropic. The model parameters are given in Table 3.1. The frequency is 30 Hz.

	ξ	ϵ	δ	γ	Q_{P0}	Q_{S0}	ϵ_Q	δ_Q	γ_Q
Figs. 3.5a,b	0°, 70°	0	0	0	10	10	0	0	0
3.5c,d	0°, 70°	0.3	0.2	0	10	10	0	0	0
3.5e,f	0°, 70°	0	0	0	10	10	0.6	0.4	0
Figs. 3.6a,b,c	0°, 45°, 70°	Same as in Figures 3.5a,b							
3.6d,e,f	0°, 45°, 70°	Same as in Figures 3.5c,d							
3.6g,h,i	0°, 45°, 70°	Same as in Figures 3.5e,f							
Fig. 3.7a	0°	0.3	0.2	0	10	10	0.6	0.4	0
3.7b	0°	0	0	0.3	10	10	0	0	0.5
Fig. 3.8	-	0.3	0.2	0	5	5	0.6	0.4	0
Fig. 3.9a	60°	0	0	0	10	10	0	0	0
3.9b	60°	0.3	0.2	0	10	10	0	0	0
3.9c	60°	0.6	0.4	0	10	10	0	0	0
3.9d	60°	0	0	0	10	10	0.6	0.4	0
Fig. 3.10a,b	60°	0.6	0.4	0	10	10	0.6	0.4	0
3.10c,d	60°	0	0	0.5	10	10	0	0	0.5
Fig. 3.11	-	0	0	0.3	5	5	0	0	0.5
Fig. 3.12a	-	0	0	1	5	5	0	0	-0.5
3.12b	-	0	0	0.3	5	5	0	0	-0.5

Table 3.1: Medium parameters used in the numerical tests. For all models, the P- and S-wave symmetry-direction velocities (V_{P0} and V_{S0}) are 2800 m/s and 1700 m/s, respectively.

3.5.2 Normalized Group Attenuation Coefficient

As discussed above, for zero inhomogeneity angle the normalized group attenuation coefficient $\mathcal{A}_g$ coincides with $\mathcal{A}|_{\xi=0^\circ}$ (equation 3.14). This conclusion, which is valid for all wave modes, is supported by Figures 3.7a and 3.7b where the coefficients $\mathcal{A}|_{\xi=0^\circ}$ (gray curve) and $\mathcal{A}_g$ (blue) practically coincide when $\xi = 0^\circ$.

To examine the influence of the angle ξ on $\mathcal{A}_g$, I linearize equation 3.12 in terms of the perturbations of the wave vector:

$$\mathcal{A}_g = \frac{k^{I,0} + \Delta k^I}{k^{R,0} + \Delta k^R} \cos\xi \left(1 + \tan\xi \tan\psi \cos\phi\right)$$

$$= \frac{k^{I,0}}{k^{R,0}} \left(1 + \frac{\Delta k^I}{k^{I,0}} - \frac{\Delta k^R}{k^{R,0}}\right) \cos\xi \left(1 + \tan\xi \tan\psi \cos\phi\right). \tag{3.31}$$

Taking into account that $k^{I,0}/k^{R,0} = 1/(2Q^0 \cos\xi)$ (equation 3.19), I find

$$\mathcal{A}_g = \frac{1}{2Q^0} \left(1 + \frac{\Delta k^I}{k^{I,0}} - \frac{\Delta k^R}{k^{R,0}}\right) (1 + \tan\xi \tan\psi \cos\phi). \tag{3.32}$$

Equation 3.32 is valid in arbitrarily anisotropic media for all wave modes. Substituting equations B.15 and B.16 for Δk^R and Δk^I and equation B.26 for the product $\tan\psi \cos\phi$ into equation 3.32, I obtain the group attenuation coefficient for P-waves linearized in Δa_{ij}:

$$\mathcal{A}_{g,P} = \frac{1}{2Q_{P0}} - \frac{1}{2V_{P0}^2} \left(\frac{\Delta a_{33}^R}{Q_{P0}} - \Delta a_{33}^I\right), \tag{3.33}$$

where Q_{P0} and V_{P0} are the P-wave quality factor and velocity, respectively, in the background. Similar expressions for S_1- and S_2-waves are given in Appendix B (equations B.30 and B.31).

Below I analyze equation 3.33 for the special case of P-wave propagation in TI media with arbitrary symmetry-axis orientation. As mentioned earlier, to express $\mathcal{A}_g$ through the phase angle θ with the symmetry axis, the tensor Δa_{ijkl} in equation 3.33 has to be rotated around the x_2-axis. Then I linearize $\mathcal{A}_g$ in the velocity- and attenuation-anisotropy parameters to obtain

$$\mathcal{A}_{g,P} = \frac{1}{2Q_{P0}} \left(1 + \delta_Q \sin^2\theta \cos^2\theta + \epsilon_Q \sin^4\theta\right). \tag{3.34}$$

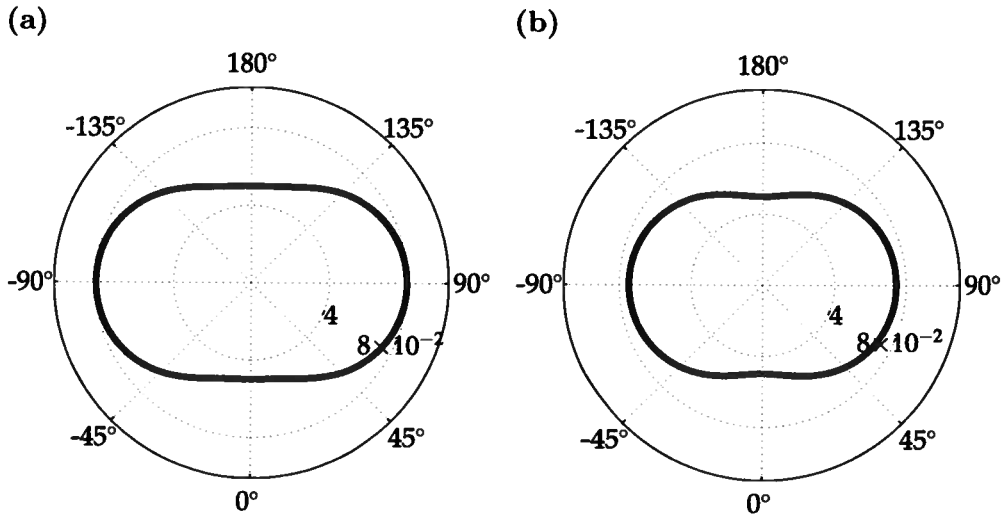

Figure 3.7: Exact P-wave (a) and SH-wave (b) coefficients $\mathcal{A}|_{\xi=0^\circ}$ (gray curves) and $\mathcal{A}_g$ (black curves) in TI media as a function of the phase angle for $\xi = 0^\circ$. Because $\mathcal{A}_g = \mathcal{A}|_{\xi=0^\circ}$, the gray curves are coincident with the black curves. The model parameters are given in Table 3.1.

Similar approximate expressions for the group attenuation coefficient of SV- and SH-waves are given in Appendix C (equations C.10 and C.11).

Therefore, the inhomogeneity angle has no influence on the approximate group attenuation coefficient. Furthermore, $\mathcal{A}_{g,P}$ in equation 3.34 coincides with the linearized P-wave phase attenuation coefficient for a zero inhomogeneity angle ($\mathcal{A}|_{\xi=0^\circ}$) derived by Zhu and Tsvankin (2006). Equation 3.34 deviates from the exact $\mathcal{A}_g$ only when the angle ξ approaches forbidden directions (Figure 3.8); the behavior of $\mathcal{A}_g$ for large inhomogeneity angles is analyzed in more detail below.

Note that the linearized $\mathcal{A}_g$ (equations 3.34, C.10, and C.11) is controlled by attenuation anisotropy and does not depend on the velocity-anisotropy parameters. This conclusion is confirmed by the exact modeling results in Figures 3.9a and 3.9b where the coefficient $\mathcal{A}_g$ remains insensitive even to strong velocity anisotropy with $\epsilon = 0.6$ and $\delta = 0.4$ when $\xi = 60^\circ$ (Figure 3.9c). The presence of attenuation anisotropy, on the other hand, results in a substantial change in $\mathcal{A}_g$ (Figure 3.9d).

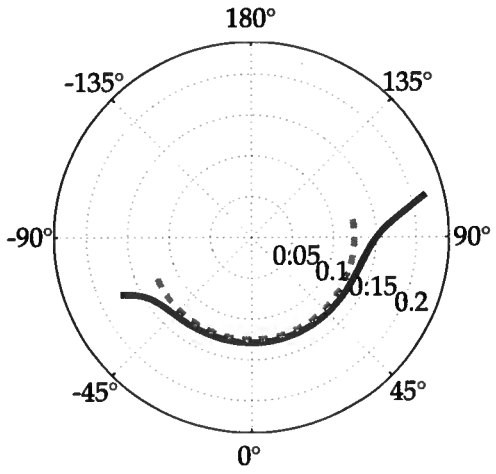

Figure 3.8: Exact P-wave group attenuation coefficient $\mathcal{A}_{g,P}$ (solid line) and approximate $\mathcal{A}_{g,P}$ from equation 3.34 (dashed line) in TI media for $\theta = 45°$ as a function of the angle ξ (numbers on the perimeter). The model parameters are given in Table 3.1.

3.5.3 Relationship Between Group and Phase Attenuation

The normalized phase attenuation coefficient $\mathcal{A}|_{\xi=0°}$ can be obtained from the Christoffel equation and expressed through the attenuation-anisotropy parameters (Zhu & Tsvankin, 2006). As shown above, the coefficient $\mathcal{A}_g$ coincides with $\mathcal{A}|_{\xi=0°}$ for a wide range of ξ in isotropic media and for $\xi = 0°$ in anisotropic media.

Using perturbation analysis, I obtained closed-form expressions for the coefficient $\mathcal{A}|_{\xi=0°}$ in arbitrarily anisotropic media linearized in Δa_{ij} (Appendix B). For P-waves,

$$\mathcal{A}|_{\xi=0°,P} = \frac{1}{2Q_{P0}} - \frac{1}{2V_{P0}^2}\left(\frac{\Delta a_{33}^R}{Q_{P0}} - \Delta a_{33}^I\right). \tag{3.35}$$

Similar expressions for S_1- and S_2-waves are given in Appendix B. Comparison of equations 3.33 and 3.35 shows that for a wide range of angles ξ (except for values close to 90°; see below), the linearized coefficient $\mathcal{A}_g$ coincides with $\mathcal{A}|_{\xi=0°}$. This conclusion is also valid for S_1- and S_2-waves (compare equations B.30 and B.31 with equations B.24 and B.25).

The approximate P-wave phase attenuation coefficient for TI media can be found as a simple function of the attenuation-anisotropy parameters (Zhu & Tsvankin, 2006):

$$\mathcal{A}|_{\xi=0°,P} = \frac{1}{2Q_{P0}}\left(1 + \delta_Q \sin^2\theta\cos^2\theta + \epsilon_Q \sin^4\theta\right). \tag{3.36}$$

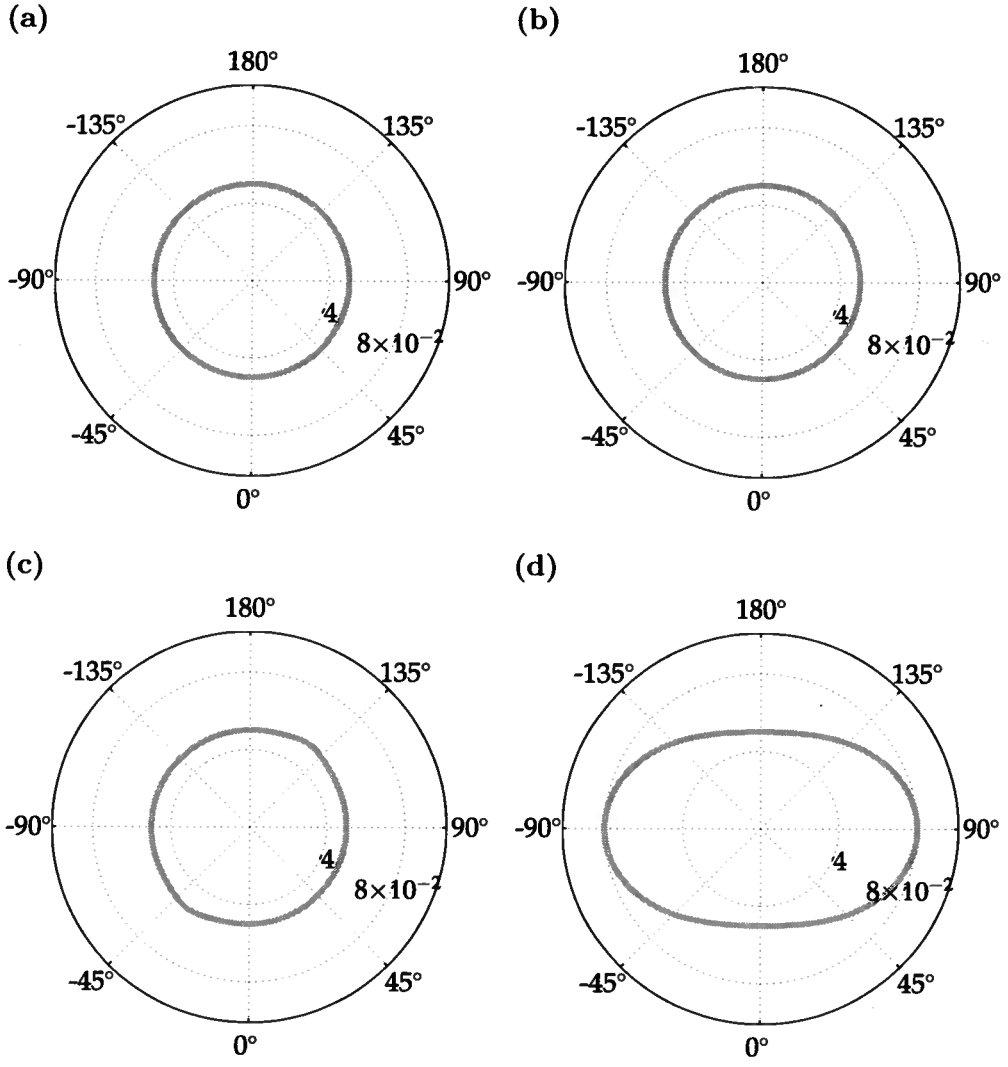

Figure 3.9: Exact P-wave group attenuation coefficient $\mathcal{A}_g$ for $\xi = 60°$ in isotropic (a) and TI (b,c,d) media. In (b,c) only velocity varies with angle, while attenuation is isotropic; in (d) attenuation varies with angle, while velocity is isotropic. The model parameters are given in Table 3.1.

Zhu & Tsvankin (2006) also provide similar linearized expressions for SV- and SH-waves reproduced in Appendix B. As is the case for arbitrary ansisotropy, the coefficient $\mathcal{A}|_{\xi=0^\circ}$ in equation 3.36 coincides with $\mathcal{A}_g$ in equation 3.34.

Figures 3.10a and 3.10b demonstrate that the maximum difference between the exact coefficients $\mathcal{A}_g$ and $\mathcal{A}|_{\xi=0^\circ}$ does not exceed 10% even for strong attenuation ($Q_{33} = 10$) and uncommonly large anisotropy parameters ($\epsilon = \epsilon_Q = 0.6$ and $\delta = \delta_Q = 0.4$). The coefficients $\mathcal{A}_g$ and $\mathcal{A}|_{\xi=0^\circ}$ are also close for SV- and SH-waves, which confirms the analytic results of Appendix C (Figures 3.10c and 3.10d).

3.5.4 Group Attenuation for Large Inhomogeneity Angles

The above conclusions about the influence of the inhomogeneity angle on phase velocity and attenuation no longer hold for large inhomogeneity angles approaching forbidden directions. As shown above for isotropic media, when $(Q\cos\xi) \ll 1$, the group attenuation coefficient varies with the angle ξ and differs from $\mathcal{A}|_{\xi=0^\circ}$.

To study the influence of large ξ analytically, I follow the same perturbation-based approach (Appendix B) but with different background values of the wave vector, group velocity, and group angle (equations 3.23–3.26). For simplicity, here I analyze only the special case of elliptical anisotropy in TI media (i.e., SH-waves); more general solutions for shear waves in arbitrarily anisotropic media are given in Appendix D. Numerical tests demonstrate that our conclusions remain valid for all wave modes and any anisotropic symmetry.

According to equation D.6, the coefficient $\mathcal{A}_g$ for large inhomogeneity angles becomes a function of ξ and cannot serve as a measure of intrinsic attenuation. As was the case for isotropy, $\mathcal{A}_g$ in anisotropic media is always finite (and does not go to zero), even though the real and imaginary parts of the wave vector (equation D.3) become infinite.

When the medium is isotropic, a physical solution of the wave equation exists only for $-90^\circ < \xi < 90^\circ$ [equation A.5; also see Červený & Pšenčík (2005a)]. The bounds for the inhomogeneity angle in arbitrarily anisotropic media depend on both velocity and attenuation anisotropy and can be derived from equation D.3 using the inequalities $k^R > 0$ and $k^I > 0$. For the special case of elliptical anisotropy (equation D.4), the inhomogeneity angle should satisfy

$$\cos\xi + \frac{\gamma \sin 2\theta}{2}\sin\xi > \frac{\gamma_Q \cos 2\theta}{4Q_{S0}}, \tag{3.37}$$

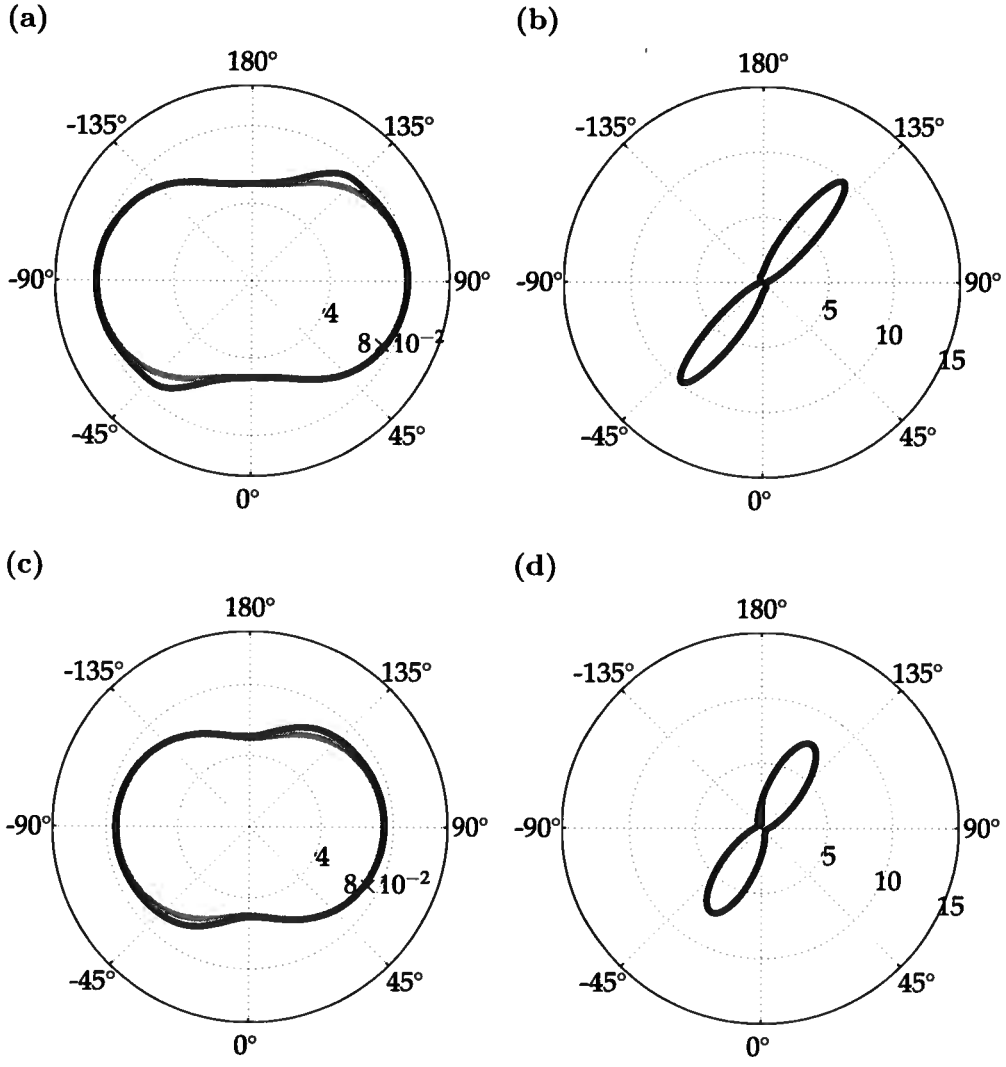

Figure 3.10: Exact P-wave (a) and SH-wave (c) coefficients $\mathcal{A}|_{\xi=0^\circ}$ (gray curve) and $\mathcal{A}_g$ (black curve) and the percentage difference $|\mathcal{A}_g - \mathcal{A}|_{\xi=0^\circ}|$ (b,d) in TI media as a function of the phase angle θ for $\xi = 60^\circ$. The model parameters are listed in Table 3.1.

which yields the following bounds for ξ:

$$-\beta - \alpha < \xi < \beta - \alpha\,, \tag{3.38}$$

where

$$\alpha = \tan^{-1}\left(\frac{-\gamma \sin 2\theta}{2}\right) \tag{3.39}$$

and

$$\beta = \cos^{-1}\left(\frac{\gamma_Q \cos 2\theta}{4Q_{S0}}\right)\,. \tag{3.40}$$

Equivalent expressions for the bounds on ξ for SH-wave propagation in the symmetry plane of a monoclinic medium are given by Červený & Pšenčík (2005a) in terms of the inhomogeneity parameter D.

For wave propagation along the symmetry axis or perpendicular to it ($\theta = 0°$ or $90°$), the angle $\alpha = 0°$ and the bounds on ξ are symmetric with respect to $\xi = 0°$ (equations 3.38 and 4.13; Figure 3.11). It is also clear from equation 4.13 that $\beta \approx 90°$ because the ratio γ_Q/Q_{S0} typically is small. Hence, for $\theta = 0°$ and $90°$ anisotropy does not signficantly change the bounds on ξ, which remain close to $\pm 90°$. As was the case for isotropic media, when the angle ξ approaches the "forbidden directions," the group attenuation coefficient $\mathcal{A}_g$ rapidly increases with $|\xi|$ and reaches values approximately twice as large as $\mathcal{A}|_{\xi=0°}$ (Figure 3.11).

For oblique propagation angles, α does not vanish, and the bounds on ξ become asymmetric with respect to $\xi = 0°$. This asymmetry is controlled by the velocity-anisotropy coefficient γ and reaches its maximum for the phase angle $\theta = 45°$ (equation 4.12). The model in Figure 3.12a, taken from Carcione & Cavallini (1995), has an uncommonly large parameter γ equal to unity, and for $\theta = 45°$ the inhomogeneity angle can vary between only $-64°$ and $116°$. Therefore, strong velocity anisotropy may result in forbidden directions for angles $|\xi|$ much smaller than $90°$.

Still, the range of possible inhomogeneity angles (2β) remains close to $180°$ because the parameter $\beta \approx 90°$ (Figure 3.12a). For more common, smaller values of the parameter γ, the bounds on ξ become more symmetric with respect to $\xi = 0°$ and do not differ significantly from $\pm 90°$ (Figure 3.12b). The behavior of the coefficient $\mathcal{A}_g$ for large angles ξ in Figure 3.12 is similar to that in isotropic media.

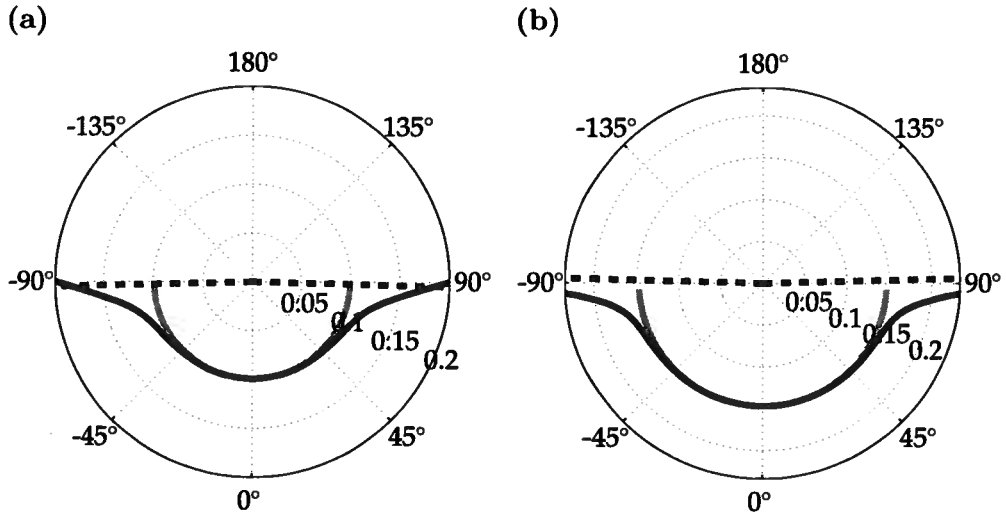

Figure 3.11: Exact SH-wave coefficients $\mathcal{A}|_{\xi=0^\circ}$ (gray curve) and $\mathcal{A}_g$ (black curve) in TI media for propagation in the directions $\theta = 0^\circ$ (a) and $\theta = 90^\circ$ (b) plotted as a function of the inhomogeneity angle ξ (numbers on the perimeter). The black dashed line marks the bounds of ξ computed from equations 3.38–4.13. The model parameters are listed in Table 3.1.

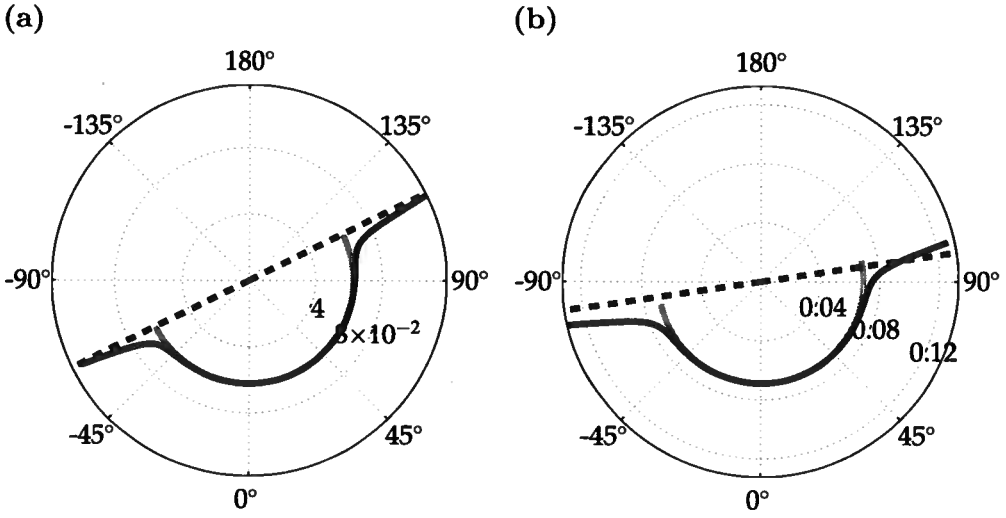

Figure 3.12: Exact SH-wave coefficients $\mathcal{A}|_{\xi=0^\circ}$ (gray curve) and $\mathcal{A}_g$ (blue) as a function of ξ (numbers on the perimeter) for $\theta = 45^\circ$ and $\gamma = 1.0, \gamma_Q = -0.5$ (a) and $\gamma = 0.3, \gamma_Q = -0.5$ (b). The black dashed line marks the bounds of ξ computed from equations 3.38–4.13. The model parameters are listed in Table 3.1.

3.6 Discussion

Our analytic and numerical results for plane-wave propagation prove that the normalized group attenuation coefficient $\mathcal{A}_g$ measured from seismic data is practically independent of the inhomogeneity angle (except for angles ξ approaching the forbidden directions) and is close to the normalized phase attenuation coefficient $\mathcal{A}|_{\xi=0^\circ}$. Behura & Tsvankin (2008) corroborate this conclusion by applying attenuation layer stripping and the spectral-ratio method to full-waveform P-wave synthetic data generated by a point source in layered anisotropic models. The interval coefficients $\mathcal{A}_g$ and $\mathcal{A}|_{\xi=0^\circ}$ estimated by Behura & Tsvankin (2008) from reflection amplitudes practically coincide even at large offsets where the inhomogeneity angle reaches 60°.

The coefficient $\mathcal{A}|_{\xi=0^\circ}$ in TI and orthorhombic media can be inverted for the Thomsen-style attenuation-anisotropy parameters using the formalism developed by Zhu & Tsvankin (2006, 2007). Note that estimation of the attenuation-anisotropy parameters from $\mathcal{A}|_{\xi=0^\circ}$ requires computation of the corresponding phase angle, which depends on the anisotropic velocity field. Even in strongly anisotropic models, however, the influence of attenuation on velocity is of the second order (see above), which implies that velocity analysis can be performed using existing methods. The reconstructed velocity field can then be employed to recompute the known group direction into the phase direction needed in the inversion for the attenuation-anisotropy parameters. Furthermore, given the large uncertainty of amplitude measurements, the difference between the phase and group directions for moderately anisotropic models should not significantly distort the results of attenuation analysis.

3.7 Conclusions

I applied the first-order perturbation theory to study the influence of the inhomogeneity angle on velocity and attenuation in arbitrarily anisotropic media. By adopting an attenuative, isotropic background medium, I was able to specify a background wave vector with an arbitrary inhomogeneity angle ξ. The perturbation analysis yields concise analytic expressions for the complex wave vector $\mathbf{k}$, the phase attenuation coefficient $\mathcal{A}|_{\xi=0^\circ}$ and the group attenuation coefficient $\mathcal{A}_g$ in terms of the perturbations of the complex stiffness coefficients. To gain physical insight into the influence of the inhomogeneity angle, I also derived closed-form expressions for TI media by linearizing the general solutions in the dimensionless velocity- and attenuation-anisotropy parameters.

For a wide range of small and moderate angles ξ, the phase-velocity function is practically independent of attenuation, while the group attenuation coefficient $\mathcal{A}_g$, which is measured from seismic data, is insensitive to the inhomogeneity angle. Furthermore, $\mathcal{A}_g$ practically coincides with the phase attenuation coefficient $\mathcal{A}|_{\xi=0^\circ}$, which is inversely proportional to the angle-dependent quality factor in anisotropic media. This conclusion remains valid even for uncommonly high attenuation ($Q \approx 10$) and strong velocity and attenuation anisotropy. The negligible difference between $\mathcal{A}_g$ and $\mathcal{A}|_{\xi=0^\circ}$ suggests that seismic data can be inverted for the attenuation-anisotropy parameters without knowledge of the inhomogeneity angle.

However, for larger angles ξ approaching the forbidden directions (i.e., the directions of the attenuation vector $\mathbf{k}^I$ for which solutions of the wave equation do not exist) the inhomogeneity angle has a strong influence on both attenuation and phase velocity. While for isotropic media the inhomogeneity angle can vary between -90° and 90°, velocity anisotropy makes the bounds on the inhomogeneity angle asymmetric with respect to $\xi = 0^\circ$. In the vicinity of the forbidden directions the coefficient $\mathcal{A}_g$ rapidly increases with $|\xi|$ and reaches values approximately twice as large as $\mathcal{A}|_{\xi=0^\circ}$. The range of such "anomalous" inhomogeneity angles where $\mathcal{A}_g$ no longer represents a direct measure of the intrinsic attenuation becomes wider for highly attenuative models.

Chapter 4

Reflection coefficients in attenuative anisotropic media

4.1 Summary

Such reservoir rocks as heavy oils are characterized by significant attenuation and, in some cases, attenuation anisotropy. Most existing attenuation studies are focused on plane-wave attenuation coefficients, which determine the amplitude decay along the raypath of seismic waves. Here, I discuss the influence of attenuation on PP- and PS-wave reflection coefficients for anisotropic media with the main emphasis on VTI (transversely isotropic with a vertical symmetry axis) models.

Concise analytic solutions obtained by linearizing the exact plane-wave reflection coefficients are verified by numerical modeling. To make a substantial contribution to reflection coefficients, attenuation has to be strong, with the quality factor Q not exceeding 10. For such highly attenuative media, it is also necessary to take attenuation anisotropy into account if the magnitude of the Thomsen-style attenuation-anisotropy parameters is relatively large. In general, the linearized reflection coefficients in attenuative media include velocity-anisotropy parameters but have almost "isotropic" dependence on attenuation.

Our formalism also helps to evaluate the influence of the inhomogeneity angle (the angle between the real and imaginary parts of the slowness vector) on the reflection coefficients. A nonzero inhomogeneity angle of the incident wave introduces additional terms into the PP- and PS-wave reflection coefficients, which makes conventional AVO (amplitude-variation-with-offset) analysis inadequate for strongly attenuative media. For instance, an incident P-wave with a nonzero inhomogeneity angle generates a mode-converted PS-wave at normal incidence, even if both halfspaces have a horizontal symmetry plane. The linearized solutions developed here can be used in AVO inversion for highly attenuative (e.g., gas-sand and heavy-oil) reservoirs.

4.2 Introduction

Conventional AVO analysis is carried out under the assumption that the subsurface is purely elastic. However, direct measurements using vertical seismic profiling (VSP) (Hauge, 1981; Hedlin *et al.*, 2001), well logs (Schmitt, 1999), and rock samples (Behura *et al.*, 2007; Winkler & Nur, 1982) show that attenuation (and, sometimes, velocity dispersion) can be significant, especially within hydrocarbon-saturated zones. Luh (1988) and Samec *et al.* (1990) attribute some failures of AVO analysis to the influence of attenuation. Furthermore, physical-modeling experiments (Hosten *et al.*, 1987; Maultzsch *et al.*, 2003; Zhu *et al.*, 2007b), rock-physics studies (Behura *et al.*, 2006; Prasad & Nur, 2003; Tao & King, 1990), and analysis of field data (Liu *et al.*, 1993; Lynn *et al.*, 1999; Vasconcelos & Jenner, 2005) indicate that attenuation can be directionally dependent, with attenuation anisotropy being stronger than velocity anisotropy (Arts & Rasolofosaon, 1992; Hosten *et al.*, 1987; Zhu *et al.*, 2007b).

While most attenuation studies are focused on attenuation coefficients, which determine the amplitude decay along the raypath of seismic waves, it is also important to evaluate the influence of attenuation and attenuation anisotropy on plane-wave reflection/transmission coefficients. Reflection coefficients for a boundary between isotropic attenuative halfspaces have been studied both analytically (Krebes, 1983; Ursin & Stovas, 2002) and using numerical modeling (Nechtschein & Hron, 1997; Hearn & Krebes, 1990). Sidler & Carcione (2007) and Stovas & Ursin (2003) discuss the influence of anisotropy on reflection/transmission coefficients in attenuative VTI media. Existing results for anisotropic models, however, do not provide physical insight into the dependence of plane-wave reflectivity on the medium properties, in particular on the anisotropy parameters that govern both velocity and attenuation.

Here, I develop linearized approximations for PP- and PS-wave reflection coefficients at a boundary between arbitrarily anisotropic, attenuative halfspaces. Then the general solutions are simplified for vertical transverse isotropy and expressed through the Thomsen-style parameters introduced by Zhu & Tsvankin (2006). It should be emphasized that our formalism takes into account the inhomogeneity angle (the angle between the real and the imaginary parts of the slowness vector) of the incident wave. Finally, I compute exact reflection coefficients for a realistic range of the velocity- and attenuation-anisotropy parameters and assess the accuracy of the linearized expressions.

4.3 Perturbation Analysis of Reflection/Transmission Coefficients

For a welded contact between two arbitrary anisotropic, attenuative halfspaces, the boundary conditions of the continuity of traction and displacement result in the following system of six linear equations (e.g., Vavryčuk & Psencík, 1998):

$$\tilde{\mathbf{C}}\,\tilde{\mathbf{U}} = \tilde{\mathbf{B}}, \tag{4.1}$$

where the accent "˜" denotes a complex quantity, $\tilde{\mathbf{C}}$ corresponds to the displacement-stress matrix for the reflected and transmitted plane waves P, S_1 and S_2, $\tilde{\mathbf{B}}$ is the displacement-stress vector of the incident wave, and $\tilde{\mathbf{U}}$ is the vector of the reflection (R) and transmission (T) coefficients. The matrix $\tilde{\mathbf{C}}$ and the vectors $\tilde{\mathbf{U}}$ and $\tilde{\mathbf{B}}$ are composed of complex elements because the stiffness tensor in attenuative media is complex. Exact reflection/transmission coefficients ($\tilde{\mathbf{U}}$) can be computed by solving the system of equations 4.1 numerically.

Following Vavryčuk & Psencík (1998) and Jílek (2002a,b), I apply the first-order perturbation theory to a background homogeneous medium, which is taken to be isotropic and attenuative. Linearization of the boundary conditions (equation 4.1) yields the perturbation $\delta\tilde{\mathbf{U}}$ in the form

$$\delta\tilde{\mathbf{U}} = (\tilde{\mathbf{C}}^0)^{-1}\,(\delta\tilde{\mathbf{B}} - \delta\tilde{\mathbf{C}}\,\tilde{\mathbf{U}}^0)\,. \tag{4.2}$$

Here, $\tilde{\mathbf{C}}^0$ is the displacement-stress matrix for the reflected/transmitted waves in the background medium and $\delta\tilde{\mathbf{C}}$ represents the perturbation of $\tilde{\mathbf{C}}^0$. Similarly, $\delta\tilde{\mathbf{B}}$ is the perturbation of the displacement-stress vector of the incident wave. $\tilde{\mathbf{U}}^0$, the vector of the amplitudes of the reflected and transmitted waves in the homogeneous background, is given by

$$\tilde{\mathbf{U}}^0 = [0,\, 0,\, 0,\, 0,\, 0,\, 1]^T\,; \tag{4.3}$$

the only nonzero term in equation 4.3 represents the P-wave transmission coefficient. A similar perturbation approach is adopted by Ursin & Stovas (2002) to derive reflection/transmission coefficients for isotropic attenuative media. (Their formalism introduces a weak contrast in parameters across the interface while keeping both halfspaces isotropic.) The change in the slownesses and polarizations of the scattered waves, required for obtaining $\delta\tilde{\mathbf{C}}$ and $\delta\tilde{\mathbf{B}}$ in equation 4.2, can be computed by perturbing the isotropic background medium (Jech & Pšenčík, 1989). I extend their method, developed for purely elastic media, to attenuative

models by taking the background attenuation into account.

The density-normalized complex stiffness tensor $\tilde{a}_{ijkl}$ of the perturbed medium can be written as

$$\tilde{a}_{ijkl} = \tilde{a}^0_{ijkl} + \delta\tilde{a}_{ijkl}, \tag{4.4}$$

where the tensor $\tilde{a}^0_{ijkl} = a^0_{ijkl} + i\, a^{0,I}_{ijkl}$ corresponds to the background medium, and the perturbation $\delta\tilde{a}_{ijkl}$ is responsible for both the velocity and attenuation anisotropy of the perturbed medium.

The quality-factor (Q) matrix (in the two-index Voigt notation) is defined as (e.g., Carcione, 2007)

$$Q_{ij} = \frac{a^R_{ij}}{a^I_{ij}}. \tag{4.5}$$

For isotropic media, the Q-matrix takes the form

$$Q = \begin{bmatrix} Q_{P0} & Q_{13} & Q_{13} & 0 & 0 & 0 \\ Q_{13} & Q_{P0} & Q_{13} & 0 & 0 & 0 \\ Q_{13} & Q_{13} & Q_{P0} & 0 & 0 & 0 \\ 0 & 0 & 0 & Q_{S0} & 0 & 0 \\ 0 & 0 & 0 & 0 & Q_{S0} & 0 \\ 0 & 0 & 0 & 0 & 0 & Q_{S0} \end{bmatrix}, \tag{4.6}$$

where Q_{P0} and Q_{S0} control the P- and the S-wave attenuation, respectively, and Q_{13} is the following function of Q_{P0} and Q_{S0} (Zhu & Tsvankin, 2006):

$$Q_{13} = Q_{P0}\frac{a_{33} - 2a_{55}}{a_{33} - 2a_{55}\frac{Q_{P0}}{Q_{S0}}}. \tag{4.7}$$

If the medium is attenuative, the wave vector becomes complex, and its real ($\mathbf{k}^R$) and imaginary ($\mathbf{k}^I$) parts may have different orientations. The angle ξ between $\mathbf{k}^R$ and $\mathbf{k}^I$ is usually called the inhomogeneity angle (Figure 5.2b). For $\xi = 0$ (so-called "homogeneous wave propagation, " Figure 5.2a), the phase direction coincides with the direction of maximum

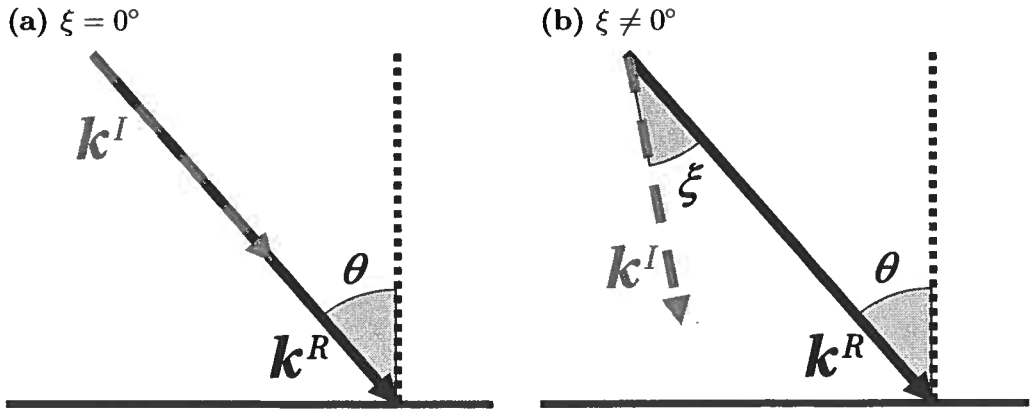

Figure 4.1: Incident plane wave with (a) zero inhomogeneity angle and (b) nonzero inhomogeneity angle ξ. $\mathbf{k}^R$ and $\mathbf{k}^I$ are the real and imaginary components (respectively) of the wave vector, and θ is the incidence phase angle.

attenuation.

Plane-wave propagation in anisotropic media is described by the Christoffel equation, which can be solved for the phase velocity, polarization vector, and phase attenuation coefficient. The Christoffel equation for a zero inhomogeneity angle can be written as

$$(\tilde{a}_{ijkl}\,\tilde{k}^2\,n_i n_l - \omega\,\delta_{jk})\,\tilde{\mathrm{g}}_j = 0\,, \tag{4.8}$$

where $\mathbf{n}$ is the unit slowness vector, ω is the frequency, $\tilde{\mathbf{g}}$ is the polarization vector, and

$$\tilde{k} = k^R - i\,k^I; \tag{4.9}$$

$k^R = |\mathbf{k}^R|$ controls the phase velocity and $k^I = |\mathbf{k}^I|$ is responsible for the phase attenuation. The ratio of k^I and k^R defines the normalized attenuation coefficient $\mathcal{A}$, which yields the rate of amplitude decay per wavelength (Zhu & Tsvankin, 2006):

$$\mathcal{A} = \frac{k^I}{k^R}. \tag{4.10}$$

When attenuation is weak or moderate ($1/Q \ll 1$) and isotropic,

$$\mathcal{A} \approx \frac{1}{2Q}. \tag{4.11}$$

The perturbations of the wave ($\delta\tilde{\mathbf{k}}$) and polarization ($\delta\tilde{\mathbf{g}}$) vectors, obtained by substituting the perturbed tensor $\tilde{a}_{ijkl}$ (equation 4.4) into the Christoffel equation 4.8, are used in equation 4.2 to derive the perturbation $\delta\tilde{\mathbf{U}}$ of the reflection/transmission coefficients (Jech & Pšenčík, 1989; Vavryčuk & Psencík, 1998; Jílek, 2002b). Note that the perturbation analysis based on equation 4.8 is strictly valid only for plane waves with a zero inhomogeneity angle ξ. Nevertheless, as shown below, our results can be extended in a straightforward way to waves with moderate angles ξ, even if the model has strong attenuation with $Q < 10$.

The complex P- and S-wave velocities ($\tilde{V}_{P0}$ and $\tilde{V}_{S0}$) in the background attenuative isotropic medium have the form

$$\tilde{V}_{P0} = \frac{\omega}{\tilde{k}_{P0}} \approx V_{P0}\,(1 + i\mathcal{A}_{P0}), \tag{4.12}$$

$$\tilde{V}_{S0} = \frac{\omega}{\tilde{k}_{S0}} \approx V_{S0}\,(1 + i\mathcal{A}_{S0}), \tag{4.13}$$

where V_{P0} and V_{S0} are the phase velocities of P- and S-waves, respectively, and $\mathcal{A}_{P0}$ and $\mathcal{A}_{S0}$ are the corresponding normalized attenuation coefficients. In equations 4.12 and 4.13, terms of the second and higher order in $1/Q$ are neglected.

4.4 Incident P-wave with a Zero Inhomogeneity Angle

If the angle ξ is set to zero, all terms in equation 4.2 coincide with those given in Vavryčuk & Psencík (1998) and Jílek (2002a,b) for non-attenuative media, but they become complex quantities. Hence, the linearized reflection coefficients for P-waves (Vavryčuk & Psencík, 1998) and PS-waves (Jílek, 2002a) can be adapted in a straightforward way for attenuative media.

4.4.1 PP-wave Reflection Coefficient

Arbitrarily Anisotropic Media The linearized PP-wave reflection coefficient in arbitrarily anisotropic media obtained from equation 4.2 is given by

$$R_{\mathrm{PP}}^{\mathrm{H}} = \frac{\Delta\rho}{2\rho_0} + \frac{\Delta\tilde{a}_{33}}{4\tilde{V}_{P0}^2} + \left(\frac{\Delta\tilde{a}_{13}}{2\tilde{V}_{P0}^2} - \frac{\Delta\tilde{a}_{33}}{4\tilde{V}_{P0}^2} - \frac{\Delta\tilde{a}_{55}}{\tilde{V}_{P0}^2} - \frac{2\tilde{V}_{S0}^2}{\tilde{V}_{P0}^2}\frac{\Delta\rho}{\rho_0}\right)\sin^2\theta$$

$$+ \frac{\Delta\tilde{a}_{11}}{4\tilde{V}_{P0}^2}\sin^2\theta\tan^2\theta, \tag{4.14}$$

where the superscript "H" ("homogeneous") indicates that the incident wave has a zero inhomogeneity angle, Δ is the contrast in a certain parameter across the interface, ρ_0 is the density of the background medium, $\tilde{a}_{ij}$ are the density-normalized complex stiffness coefficients in Voigt notation (i.e., the stiffness matrix), and θ the incidence angle (Figure 5.2a).

Equation 4.14 is derived under the assumption that the contrasts in the medium properties across the interface are small ($|\Delta\tilde{a}_{ijkl}| \ll \|\tilde{a}^0_{ijkl}\|, |\Delta\rho| \ll \rho^0$, $\tilde{a}^0_{ijkl}$ and ρ^0 are the background stiffness tensor and density). The linearized reflection coefficient in equation 4.14 reduces to that in purely elastic media, if all complex quantities are made real. Although equation 4.14 is strictly valid only if all waves have a zero inhomogeneity angle, it remains sufficiently accurate for a wide range of ξ values, unless the medium is strongly attenuative (see below).

VTI Media Next, I analyze equation 4.14 for the special case of attenuative VTI media using Thomsen-style notation. In addition to the well-known Thomsen velocity parameters V_{P0}, V_{S0}, ϵ, δ, and γ, I employ the attenuation parameters $\mathcal{A}_{P0}$, $\mathcal{A}_{S0}$, ϵ_Q, δ_Q, and γ_Q introduced by Zhu & Tsvankin (2006). $\mathcal{A}_{P0} \approx 1/(2Q_{P0})$ and $\mathcal{A}_{S0} \approx 1/(2Q_{S0})$ are the normalized symmetry-direction (vertical) attenuation coefficients of P- and S-waves, respectively, ϵ_Q and δ_Q control the angular variation of the P- and SV-wave attenuation coefficients, and γ_Q governs SH-wave attenuation anisotropy.

To simplify the reflection coefficient, it is convenient to assume that terms proportional to $1/Q^2_{P0}$ and $1/Q^2_{S0}$ are sufficiently small to be dropped. Then equation 4.14 takes the form:

$$R^{\mathrm{H}}_{\mathrm{PP}} = R^{\mathrm{H}}_{\mathrm{PP}}(0) + G^{\mathrm{H}}_{\mathrm{PP}} \sin^2\theta + C^{\mathrm{H}}_{\mathrm{PP}} \sin^2\theta \tan^2\theta\,, \tag{4.15}$$

where $R^{\mathrm{H}}_{\mathrm{PP}}(0)$ is the normal-incidence PP-wave reflection coefficient (AVO intercept), $G^{\mathrm{H}}_{\mathrm{PP}}$ is the AVO gradient, and $C^{\mathrm{H}}_{\mathrm{PP}}$ is the curvature term. Equation 4.15 is a Shuey-type approximation for the PP reflection coefficient in attenuative media, in which all three terms are complex:

$$R^{\mathrm{H}}_{\mathrm{PP}}(0) = \frac{\Delta\rho}{2\rho_0} + \frac{\Delta V_{P0}}{2V_{P0}} + \frac{\Delta\mathcal{A}_{P0}}{2}\left(i + \frac{1}{Q_{P0}}\right), \tag{4.16}$$

$$G_{\rm PP}^{\rm H} = \frac{-2}{g^2}\frac{\Delta\rho}{\rho_0} + \frac{\Delta V_{P0}}{2V_{P0}} - \frac{4}{g^2}\frac{\Delta V_{S0}}{V_{S0}} + \frac{\Delta\delta}{2} + i\left(\frac{\Delta\mathcal{A}_{P0}}{2} - \frac{4\Delta\mathcal{A}_{S0}}{g^2}\right)$$
$$+ \frac{i}{Q_{P0}}\left(\frac{2}{g^2}\frac{\Delta\rho}{\rho_0} + \frac{4}{g^2}\frac{\Delta V_{S0}}{V_{S0}} - \frac{i}{2}\Delta\mathcal{A}_{P0} + \frac{4i}{g^2}\Delta\mathcal{A}_{S0} + \frac{\Delta\delta_Q}{4}\right)$$
$$- \frac{i}{Q_{S0}}\frac{2}{g^2}\left(\frac{\Delta\rho}{\rho_0} + 2\frac{\Delta V_{S0}}{V_{S0}}\right), \tag{4.17}$$

and

$$C_{\rm PP}^{\rm H} = \frac{\Delta V_{P0}}{2V_{P0}} + \frac{\Delta\epsilon}{2} + \frac{i}{2}\Delta\mathcal{A}_{P0} + \frac{1}{Q_{P0}}\left(\frac{\Delta\mathcal{A}_{P0}}{2} + \frac{i}{4}\Delta\epsilon_Q\right); \tag{4.18}$$

$g \equiv V_{P0}/V_{S0}$.

Eliminating the influence of attenuation on $R_{\rm PP}^{\rm H}(0)$, $G_{\rm PP}^{\rm H}$, and $C_{\rm PP}^{\rm H}$ in equations 4.16–4.18 reduces them to the expressions for the PP-wave intercept, gradient, and curvature (respectively) for purely elastic VTI media (Rüger, 2002). As illustrated by Figure 4.2, the linearized approximation stays close to the exact reflection coefficient for a wide range of θ values, even when Q_{P0} is as low as 10. The decrease in the accuracy of equation 4.15 with incidence angle (Figure 4.2) is typical for weak-contrast, weak-anisotropy approximations for reflection coefficients.

Since the attenuation coefficient $\mathcal{A} \sim 1/2Q$, it is clear from equations 4.16–4.18 that the influence of attenuation on the reflection coefficient is comparable to that of the velocity and density contrasts only if the quality factor is small (e.g., $Q_{P0}, Q_{S0} < 10$). This conclusion is confirmed by the test in Figure 4.3 with the model parameters simulating an interface between purely elastic shale and attenuative oil sand. When the attenuation in the sand is moderate ($Q_{P,2} = 2Q_{S,2} = 50$), the coefficient $R_{\rm PP}^{\rm H}$ is almost identical to that in the elastic case. Even a small Q-value of 10 does not noticeably change the reflection coefficient. However, when the attenuation is extremely strong ($Q_{P,2} = 2Q_{S,2} = 2.5$ or 5), the reflection coefficient substantially deviates from that for the purely elastic model.

The "isotropic" parameter $\Delta\mathcal{A}_{P0}$ in equation 4.16 is responsible for the influence of attenuation on the normal-incidence reflection coefficient. Also, $\Delta\mathcal{A}_{P0}$ makes a more significant contribution to $G_{\rm PP}^{\rm H}$ and $C_{\rm PP}^{\rm H}$ than do ϵ_Q and δ_Q because the attenuation-anisotropy parameters in equations 4.17 and 4.18 are scaled by $1/Q_{P0}$. In general, the contribution of the terms multiplied with $1/Q_{P0}$ and $1/Q_{S0}$ in equations 4.16–4.18 is of the second order,

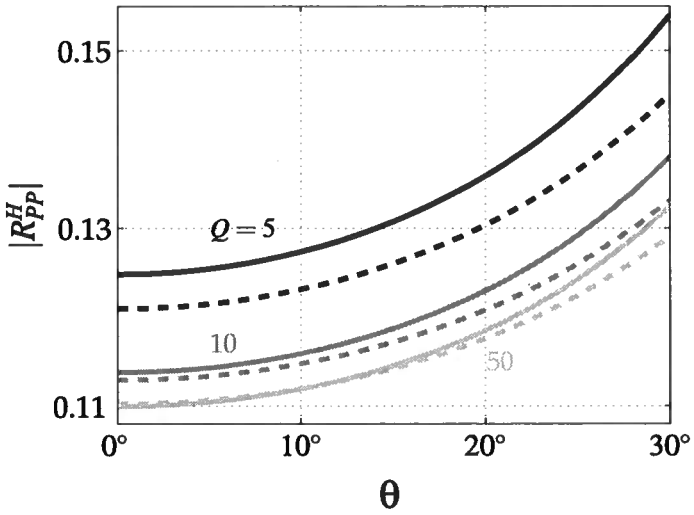

Figure 4.2: Magnitude of the PP-wave reflection coefficient at the ocean floor for different values of the quality factor Q of the ocean-floor sediments ($Q = Q_{P0,2} = 2Q_{S0,2}$). The solid lines are the exact coefficients; the dashed lines mark the linearized approximation 4.15. The model parameters are listed in Table 4.1.

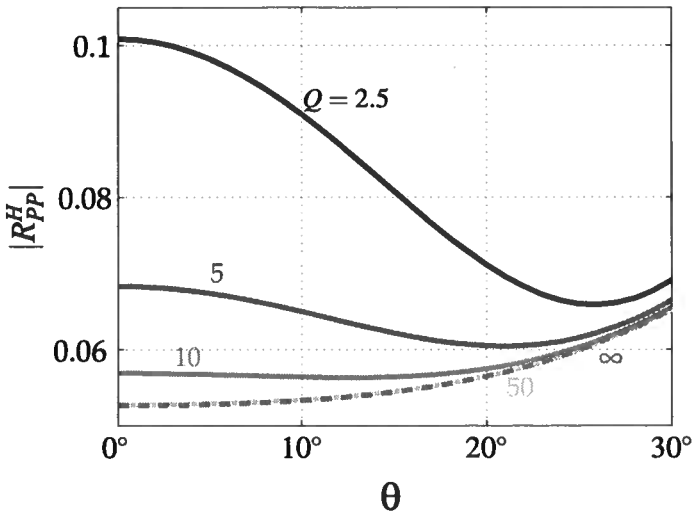

Figure 4.3: Magnitude of the exact PP-wave reflection coefficient for an interface between VTI shale with negligible attenuation and attenuative isotropic oil sand (Table 4.1). The solid lines correspond to different Q-values in the sand ($Q = Q_{P0,2} = 2Q_{S0,2}$); the dashed line corresponds to zero attenuation ($Q_{P0,2} = Q_{S0,2} = \infty$).

Parameters	Fig. 2	Fig. 3	Fig. 4	Figs. 5 & 6	Fig. 8	Fig. 9
ρ_1	1.0	2.0	2.0	2.0	2.3	2.3
$V_{P0,1}$	1.5	2.0	2.0	2.0	3.3	3.3
$V_{S0,1}$	0	1.1	1.1	1.1	1.9	1.9
δ_1	0	0.2	0.2	0.2	0	0
ϵ_1	0	0.1	0.1	0.1	0	0
$Q_{P0,1}$	∞	500	500	-	5	-
$Q_{S0,1}$	∞	250	250	-	2.5	-
$\delta_{Q,1}$	0	0.8	0.8	0.8	0	0
$\epsilon_{Q,1}$	0	-0.4	-0.4	-0.4	0	0
ρ_2	1.1	2.0	2.0	2.0	2.0	2.0
$V_{P0,2}$	1.7	1.8	1.8	1.8	2.5	2.5
$V_{S0,2}$	0.1	1.0	1.0	1.0	1.3	1.3
δ_2	0	0	0	0	0	0.1
ϵ_2	0	0	0	0	0	0.2
$Q_{P0,2}$	-	-	-	-	10	-
$Q_{S0,2}$	-	-	-	-	5	-
$\delta_{Q,2}$	0	0	-	0	0	0.8
$\epsilon_{Q,2}$	0	0	0	0	0	-0.4

Table 4.1: Medium parameters used in the numerical tests. For all models, the symmetry-direction velocities (V_{P0} and V_{S0}) are in km/s and density (ρ) is in gm/cm^3. A dash means that the parameter value is shown on the plot.

unless the medium has extremely high attenuation.

As is the case for purely elastic VTI media, the linearized P-wave AVO gradient (equation 4.17) is sensitive to the velocity-anisotropy parameter δ. Although the attenuation-anisotropy parameter δ_Q governs the P-wave attenuation near the symmetry axis, the scaling factor $1/Q_{P0}$ makes its influence on $G^{\mathrm{H}}_{\mathrm{PP}}$ less significant than that of δ. Similarly, the curvature term $C^{\mathrm{H}}_{\mathrm{PP}}$ (equation 4.18) is more sensitive to the parameter ϵ than to ϵ_Q (note that ϵ_Q does not contribute to the linearized AVO gradient). The parameters γ and γ_Q control only the anisotropy of SH-waves, which are decoupled from P- and SV-waves analyzed here. On the whole, the reflection coefficient for typical subsurface formations with $Q > 10$ is more sensitive to velocity anisotropy than to attenuation anisotropy.

The influence of the parameter δ_Q on the AVO gradient is illustrated in Figure 4.4 where the model is similar to that in Figure 4.3, but the oil sand (reflecting medium) exhibits attenuation anisotropy. When attenuation is weak ($Q = 50$), the AVO gradient barely varies with δ_Q. However, as the magnitude of attenuation increases ($Q \leq 10$), the influence of attenuation anisotropy becomes pronounced; strong attenuation can even change the sign of the AVO gradient. Our results confirm the common view that moderate attenuation does not substantially distort reflection coefficients. For highly attenuative media with $Q < 10$, however, it is necessary to take not just attenuation, but also attenuation anisotropy into account.

4.4.2 PS-wave Reflection Coefficient for VTI Media

Using the approach outlined above, I obtained the following closed-form linearized expression for the PS-wave reflection (conversion) coefficient in attenuative VTI media:

$$R^{\mathrm{H}}_{\mathrm{PS}} = B^{\mathrm{H}}_{\mathrm{PS}} \sin\theta + K^{\mathrm{H}}_{\mathrm{PS}} \sin^3\theta, \tag{4.19}$$

where the coefficients $B^{\mathrm{H}}_{\mathrm{PS}}$ and $K^{\mathrm{H}}_{\mathrm{PS}}$ (the gradient and curvature terms, respectively, in conventional PS-wave AVO analysis) are given by

$$B^{\mathrm{H}}_{\mathrm{PS}} = -\frac{2+g}{2g}\frac{\Delta\rho}{\rho_0} - \frac{2}{g}\frac{\Delta V_{S0}}{V_{S0}} + \frac{g}{2(1+g)}\Delta\delta - i\frac{2}{g}\Delta\mathcal{A}_{S0}$$

$$+ \frac{i}{Q_{P0}} f_1 - \frac{i}{Q_{S0}} f_2\,, \tag{4.20}$$

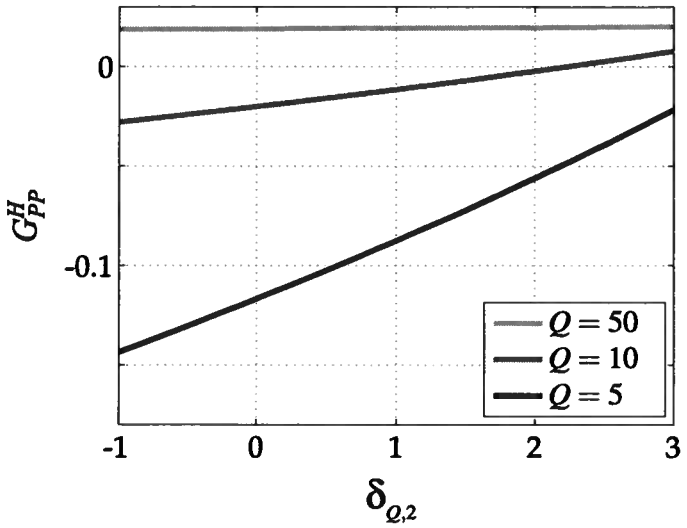

Figure 4.4: PP-wave AVO gradient as a function of the attenuation-anisotropy parameter $\delta_{Q,2}$ in the reflecting halfspace. The gradient is estimated numerically as the initial slope of the exact PP-wave reflection coefficient computed as a function of $\sin^2\theta$. The model is similar to that in Figure 4.3, but the attenuation in the reflecting oil sand is anisotropic (Table 4.1). The curves correspond to different Q-values in the sand ($Q = Q_{P0,2} = 2Q_{S0,2}$).

$$K^{\mathrm{H}}_{\mathrm{PS}} = \frac{(3+2g)}{4g^2}\frac{\Delta\rho}{\rho_0} + \frac{2+g}{g^2}\frac{\Delta V_{S0}}{V_{S0}} + \frac{1-4g}{2(1+g)}\Delta\delta + \frac{g}{1+g}\Delta\epsilon + i\frac{2+g}{g^2}\Delta\mathcal{A}_{S0}$$

$$- \frac{i}{2Q_{P0}}f_3 + \frac{i}{2Q_{S0}}f_4\,. \tag{4.21}$$

Here, f_1, f_2, f_3, and f_4 are linear combinations of the parameter contrasts across the interface listed in Appendix E. The contributions of $f_{1,2,3,4}$ to the reflection coefficient are of the second order because these functions are scaled by $1/Q_{P0}$ or $1/Q_{S0}$.

The real part of the reflection coefficient in equation 4.19 coincides with the corresponding linearized expression for PS-waves in a purely elastic VTI medium. Most conclusions drawn above for PP-waves remain valid for the PS-wave reflection coefficient as well. In particular, the influence of the attenuation contrasts on $R^{\mathrm{H}}_{\mathrm{PS}}$ becomes comparable to that of the velocity and density contrasts only when $Q_{P0}, Q_{S0} < 10$. The attenuation-related part of $R^{\mathrm{H}}_{\mathrm{PS}}$ is controlled primarily by the contrast in the vertical S-wave attenuation coefficient $\mathcal{A}_{S0}$ because $\Delta\epsilon_Q$ and $\Delta\delta_Q$ contribute only to the functions $f_{1,3}$ multiplied with $1/Q_{P0}$

(equations E.1 and E.3).

4.5 Incident P-wave with a Nonzero Inhomogeneity Angle

If the upper halfspace is attenuative, the incident P-wave can have a nonzero inhomogeneity angle ξ (Figure 5.2b). This situation may be typical, for example, for the bottom of an attenuative reservoir. Since the angle ξ is determined by the medium properties along the whole raypath, the imaginary part $\mathbf{k}^I$ of the wave vector may even deviate from the vertical incidence plane. However, for simplicity I assume that this deviation can be ignored.

For a nonzero angle ξ, the real and imaginary parts of the wave vector $\tilde{\mathbf{k}}$ are not parallel, and the Christoffel equation becomes

$$(\tilde{a}_{ijkl}\,\tilde{k}_i\,\tilde{k}_l - \omega\,\delta_{jk})\,\tilde{g}_j = 0\,. \tag{4.22}$$

Although the perturbation analysis of Jech & Pšenčík (1989) is not strictly valid for equation 4.22, it remains sufficiently accurate for moderate values of ξ, if the quality factor is not uncommonly small (Zhu & Tsvankin, 2006). Therefore, the formulation of Vavryčuk & Psencík (1998) and Jílek (2002a,b) can be applied in a straightforward way to linearize the reflection coefficient for an incident wave with a nonzero ξ. The numerical results below confirm that this approach yields an accurate approximation for most plausible attenuative models.

4.5.1 PP-wave Reflection Coefficient

The linearized PP-wave reflection coefficient $R_{\mathrm{PP}}^{\mathrm{IH}}$ for arbitrarily anisotropic media and the incident wave with $\xi \neq 0°$ represents a linear function f_0 of the following parameters:

$$R_{\mathrm{PP}}^{\mathrm{IH}} = f_0(\Delta\rho/\rho^0, \tilde{V}_{P0}, \tilde{V}_{S0}, \Delta\tilde{a}_{11}, \Delta\tilde{a}_{13}, \Delta\tilde{a}_{15}, \Delta\tilde{a}_{33}, \Delta\tilde{a}_{35}, \Delta\tilde{a}_{55}, \theta, \xi)\,. \tag{4.23}$$

Due to the complicated form of f_0, it is not shown in the paper explicitly. The reflection coefficient in equation 4.23 depends on three additional stiffness contrasts ($\Delta\tilde{a}_{11}, \Delta\tilde{a}_{15}$, and $\Delta\tilde{a}_{35}$) compared to that for $\xi = 0°$ (equation 4.14).

For VTI media, the perturbation result 4.23 reduces to

$$R_{\mathrm{PP}}^{\mathrm{IH}} = R_{\mathrm{PP}}^{\mathrm{IH}}(0) + B_{\mathrm{PP}}^{\mathrm{IH}} \sin\theta + G_{\mathrm{PP}}^{\mathrm{IH}} \sin^2\theta\,, \tag{4.24}$$

where

$$R_{\mathrm{PP}}^{\mathrm{IH}}(0) = R_{\mathrm{PP}}^{\mathrm{H}}(0) + \frac{\sin^2\xi}{4Q_{P0}} f_5\,, \tag{4.25}$$

$$B_{\mathrm{PP}}^{\mathrm{IH}} = \frac{-i\sin\xi}{Q_{P0}} f_6\,, \tag{4.26}$$

$$G_{\mathrm{PP}}^{\mathrm{IH}} = G_{\mathrm{PP}}^{\mathrm{H}} + \frac{i\sin^2\xi}{8Q_{P0}} f_7\,. \tag{4.27}$$

Here, $R_{\mathrm{PP}}^{\mathrm{H}}(0)$ and $G_{\mathrm{PP}}^{\mathrm{H}}$ are the solutions for $\xi = 0°$ (superscript "H") given by equations 4.16 and 4.17, respectively, and f_5, f_6, and f_7 are linear functions listed in Appendix E.

As illustrated by Figure 4.5, equation 4.24 remains accurate for moderate inhomogeneity angles reaching 30°. Even for $Q = 2.5$ and $\xi = 30°$ (Figure 4.5i), approximation 4.24 deviates from the exact reflection coefficient by less than 10%.

In contrast to the conventional AVO equation for pure (non-converted) waves, which represents an even function of θ (e.g., equation 4.15), equation 4.24 includes the $\sin\theta$-term. Therefore, the contribution of the inhomogeneity angle makes the basic equation of conventional PP-wave AVO analysis inadequate, which may have significant implications for AVO inversion and interpretation.

However, since the angle ξ is associated with the terms f_5, f_6, and f_7, which are scaled by $1/Q_{P0}$, its influence becomes pronounced only in strongly attenuative media. Indeed, the variation of the inhomogeneity angle from 0° to 50° does not significantly change the exact reflection coefficient for $Q \geq 10$ (Figure 4.6a,b). Only when $Q = 5$ and the inhomogeneity angle exceeds 30°, its contribution to the reflection coefficient (in particular, to the term $B_{\mathrm{PP}}^{\mathrm{IH}}$) becomes substantial (Figure 4.6c).

The asymmetry of the reflection coefficient with respect to $\theta = 0°$ (Figures 4.6b and 4.6c), which increases with the inhomogeneity angle, is explained in Figure 4.7. In our modeling, the inhomogeneity angle of the incident wave is fixed (i.e., it is independent of θ), which implies that the imaginary part $\mathbf{k}^I$ of the wave vector makes different angles with the vertical for the incidence angles θ and $-\theta$. As a result, the reflection coefficient for positive incidence angles differs from that for negative angles.

In reality, it is unlikely for the incident wave to have a constant inhomogeneity angle for a wide range of θ. A more plausible scenario is depicted in Figure 4.8a. The model includes an attenuative reservoir beneath a purely elastic cap rock. Because the cap rock is

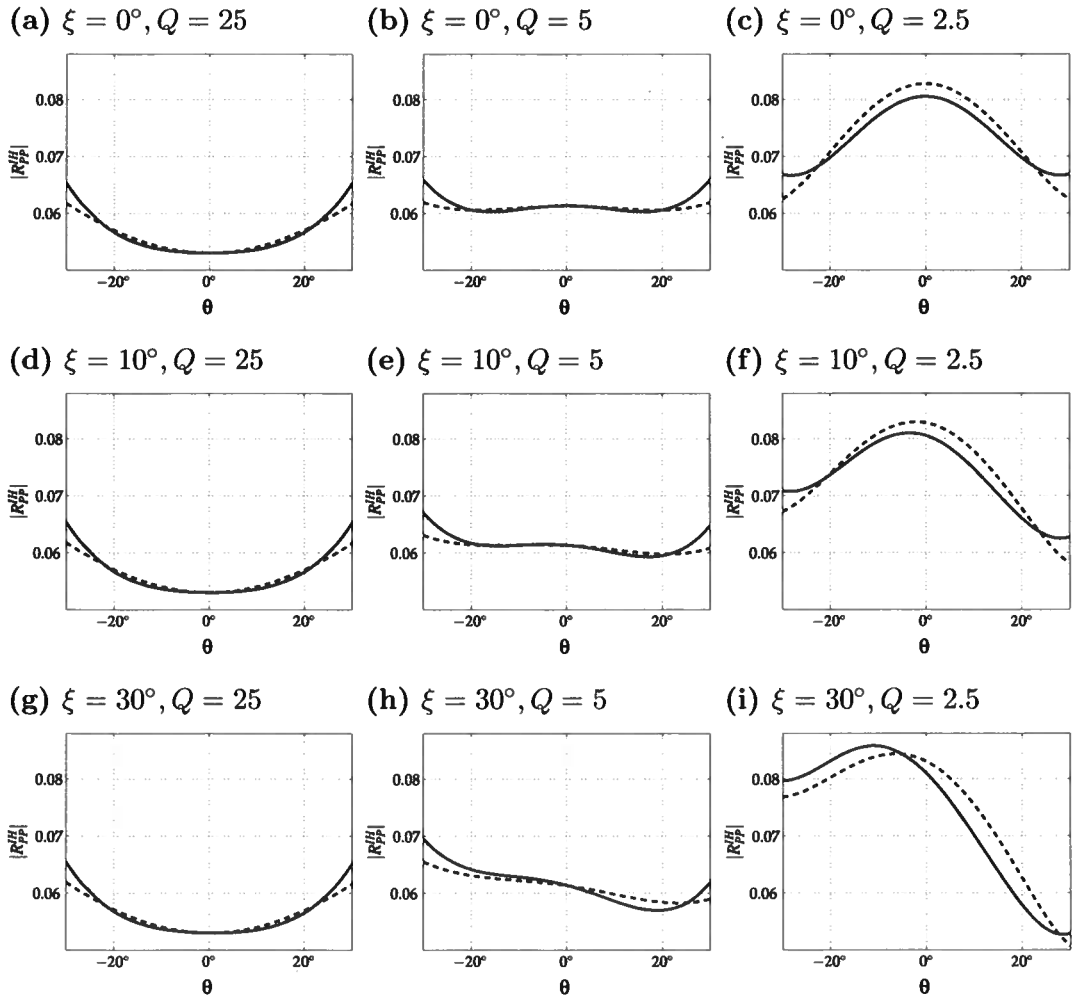

Figure 4.5: Magnitude of the exact (solid lines) and approximate (dashed lines, equation 4.24) PP-wave reflection coefficient at a VTI/isotropic interface for different inhomogeneity angles. The quality factors are $Q = Q_{P0,1} = 2Q_{S0,1} = Q_{P0,2}/2 = Q_{S0,2}$; the other model parameters are listed in Table 4.1.

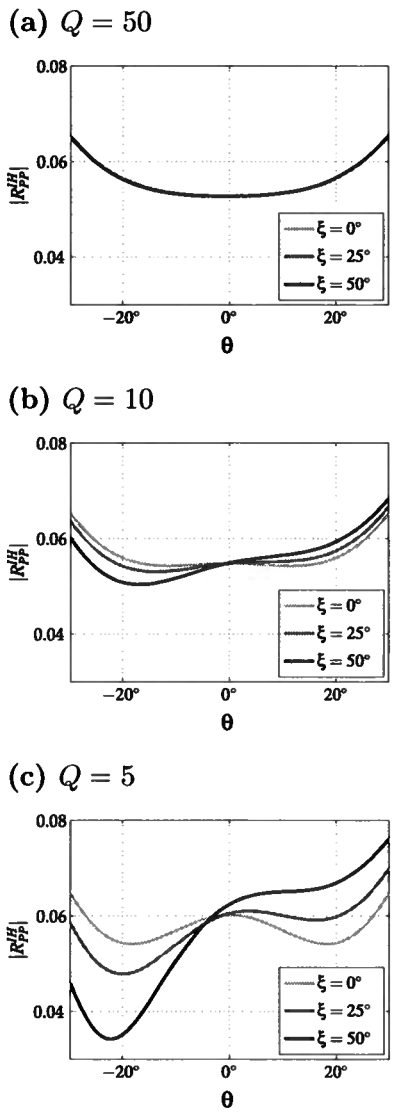

Figure 4.6: Magnitude of the exact PP-wave reflection coefficient at a VTI/isotropic interface for different inhomogeneity angles. The quality factors are $Q = Q_{P0,1} = 2Q_{S0,1} = 2Q_{P0,2} = 4Q_{S0,2}$; the other model parameters are listed in Table 4.1.

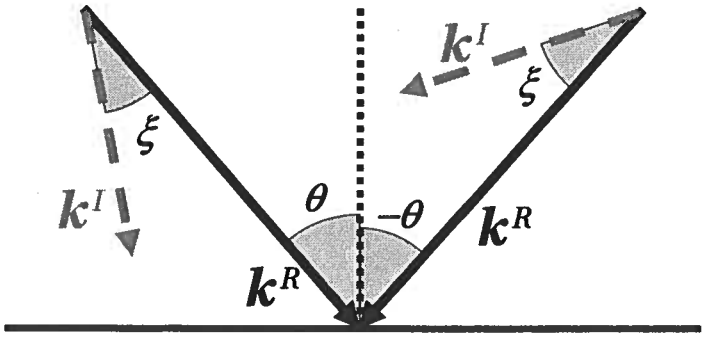

Figure 4.7: PP-wave reflection coefficient may become asymmetric with respect to $\theta = 0°$ for a nonzero inhomogeneity angle ξ. As before, $\mathbf{k}^R$ and $\mathbf{k}^I$ are the real and imaginary parts, respectively, of the wave vector of the incident P-wave.

non-attenuative, the wave incident upon the reservoir has a real wave vector. According to Snell's law, the horizontal slowness (and the horizontal component of the wave vector) has to be preserved during reflection and transmission. Therefore, the imaginary part $\mathbf{k}^I$ of the wave vector in the reservoir cannot have a horizontal component, and the inhomogeneity angle of the transmitted wave is equal to the transmission angle θ_T (Figure 4.8a). For the reflection from the bottom of the reservoir, θ_T becomes the incidence angle. Therefore, the vector $\mathbf{k}^I$ for both positive and negative incidence angles remains vertical (i.e., the wave vector as a whole is symmetric with respect to the reflector normal), and the PP-wave reflection coefficient is an even function of θ (Figure 4.8b, gray line). However, for more complicated overburden models, the inhomogeneity angle can be different from the incidence angle, which makes the reflection coefficient asymmetric with respect to θ (Figure 4.8b, black line; $\xi = 50°$ was held constant).

4.5.2 PS-wave Reflection Coefficient

As is the case for PP-waves, the influence of the inhomogeneity angle of the incident P-wave changes the conventional PS-wave AVO equation. The linearized PS-wave coefficient for $\xi \neq 0$ becomes

$$R_{\mathrm{PS}}^{\mathrm{IH}} = R_{\mathrm{PS}}^{\mathrm{IH}}(0) + B_{\mathrm{PS}}^{\mathrm{IH}} \sin\theta + G_{\mathrm{PS}}^{\mathrm{IH}} \sin^2\theta\,, \tag{4.28}$$

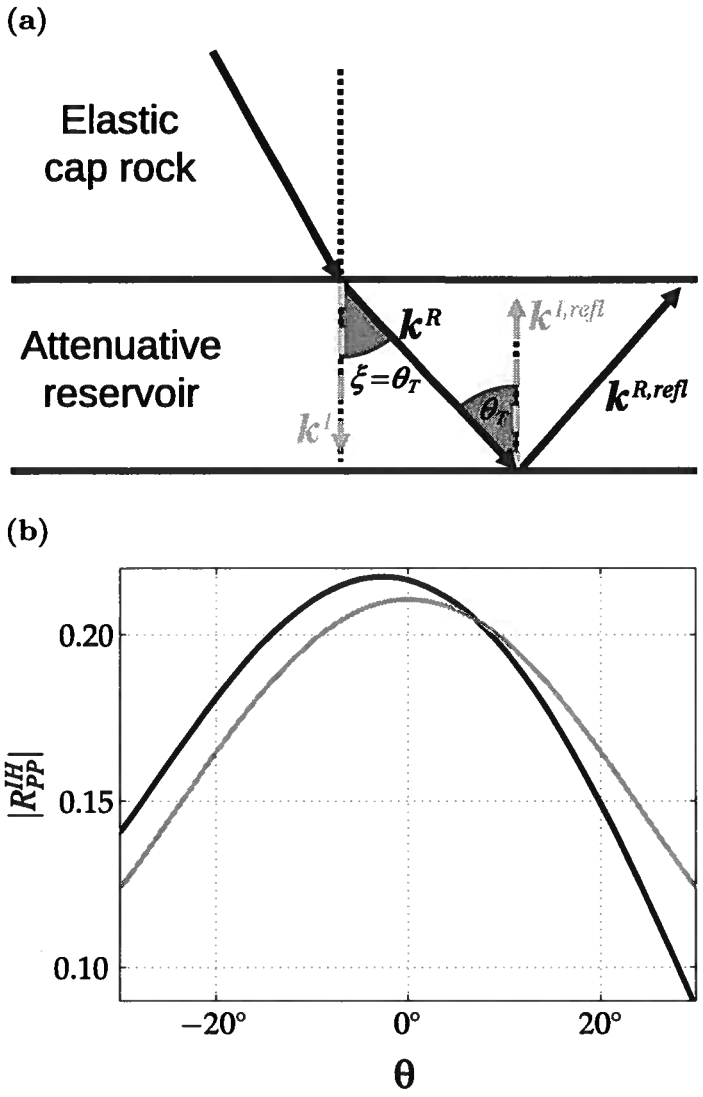

Figure 4.8: (a) Wave vectors of the incident and reflected waves in an attenuative layer (reservoir) overlaid by a purely elastic medium (cap rock). The inhomogeneity angle ξ of the wave transmitted through the top of the reservoir is equal to the transmission angle θ_T. $\mathbf{k}^{R,ref}$ and $\mathbf{k}^{I,ref}$ are the real and imaginary components, respectively, of the wave vector for the reflection from the bottom of the reservoir. (b) Magnitude of the exact PP-wave reflection coefficient from the reservoir bottom for $\xi = \theta_T$ (gray line) and for a constant inhomogeneity angle $\xi = 50°$ (black line). The model parameters are listed in Table 4.1.

where

$$R_{\rm PS}^{\rm IH}(0) = i\frac{\sin\xi}{Q_{P0}} f_8\,, \tag{4.29}$$

$$B_{\rm PS}^{\rm IH} = B_{\rm PS}^{\rm H}\,, \tag{4.30}$$

$$G_{\rm PS}^{\rm IH} = -i\frac{\sin\xi}{Q_{P0}} f_9\,. \tag{4.31}$$

Equations 4.28–4.31 do not include cubic and higher-order terms in $\sin\theta$ and $\sin\xi$. $B_{\rm PS}^{\rm H}$ is the PS-wave AVO gradient for an incident wave with a zero inhomogeneity angle (equation 4.20), and the terms f_8 and f_9 are linear combinations of the parameter contrasts across the interface (Appendix A).

Equation 4.28 is different from equation 4.19 for $\xi = 0°$, in which only the coefficients of odd powers in $\sin\theta$ are nonzero (i.e., the reflection coefficient is an odd function of θ). The deviation of equation 4.28 from the conventional PS-wave AVO equation is illustrated in Figure 4.9, where the absolute value of the PS-wave reflection coefficient in strongly attenuative media ($Q = 2.5$) for $\xi = 50°$ is visibly asymmetric with respect to $\theta = 0°$. While the coefficient $R_{\rm PS}^{\rm IH}$ for $Q = 50$ almost coincides with that for a purely elastic medium, the influence of attenuation and the inhomogeneity angle becomes pronounced for low values of Q.

Because the linearized AVO gradient $B_{\rm PS}^{\rm IH}$ (equation 4.30) does not depend on ξ, the inhomogeneity angle has a greater influence on $R_{\rm PS}^{\rm IH}(0)$ and $G_{\rm PS}^{\rm IH}$ than on $B_{\rm PS}^{\rm IH}$. For a zero inhomogeneity angle of the incident wave, $R_{\rm PS}^{\rm IH}(0)$ and $G_{\rm PS}^{\rm IH}$ vanish and equation 4.28 reduces to the term proportional to $\sin\theta$ in equation 4.19.

For $\xi \neq 0$ and small Q-values, the magnitude of the normal-incidence PS-wave reflection coefficient $R_{\rm PS}^{\rm IH}(0)$ can be substantial (Figure 4.9). A nonzero inhomogeneity angle of the vertically traveling P-wave makes its wave vector asymmetric with respect to the reflector normal, which generates the PS conversion. Note that generation of reflected or transmitted PS-waves at normal incidence can be also caused by such factors as lateral heterogeneity, the deviation of the reflector from the symmetry planes of the model (Behura & Tsvankin, 2006), and the influence of additional terms of the ray-series expansion on point-source radiation (Tsvankin, 1995). Here, however, the model is composed of homogeneous VTI halfspaces with a common horizontal symmetry plane, and I consider only plane-wave reflection coefficients.

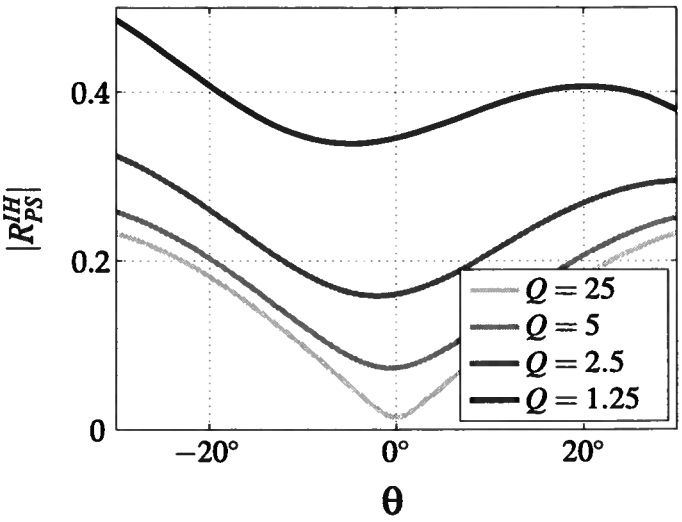

Figure 4.9: Magnitude of the exact PS-wave reflection coefficient at an isotropic/VTI interface for a nonzero inhomogeneity angle ($\xi = 50°$) of the incident P-wave and variable quality factor $Q = Q_{P0,1} = 2Q_{S0,1} = Q_{P0,2}/2 = Q_{S0,2}$. The other model parameters are listed in Table 4.1.

4.6 Discussion

The plane-wave reflection coefficients analyzed here are derived for plane interfaces and, therefore, break down in the presence of significant reflector curvature (van der Baan & Smit, 2006; Ayzenberg *et al.*, 2008). Reflections from curved interfaces can be analyzed by employing so-called "effective reflection coefficients (ERC)" extended to anisotropic media by Ayzenberg *et al.* (2008). Plane-wave reflection coefficients are often incorporated into the geometrical-seismics approximation to describe wavefields generated by point sources. Geometrical seismics, however, loses accuracy for near- and post-critical incidence angles and for source/receiver locations near the reflector. If the interface is plane, the exact scattered wavefields can be modeleled using Weyl-type integrals, which include plane-wave reflection/transmission coefficients (Tsvankin, 1995).

In contrast to most previous publications, our formalism takes into account the inhomogeneity angle ξ of the incident wave. As demonstrated above, reflection coefficients of both PP- and PS-waves become sensitive to the angle ξ only when it is relatively large and the medium is highly attenuative. This result facilitates AVO analysis in attenuative

media because the inhomogeneity angle is extremely difficult to evaluate from seismic data. Indeed, the group attenuation coefficient (i.e., the attenuation along the raypath) measured from seismic amplitudes is independent of ξ for a wide range of small and moderate inhomogeneity angles (Behura & Tsvankin, 2009). Potentially, the inhomogeneity angle can be estimated from the reflection coefficient provided *a priori* information about the parameter contrasts is available and ξ is sufficiently large. However, the increase in the group attenuation coefficient for large values of ξ (Behura & Tsvankin, 2009) reduces the reflection amplitude and makes AVO analysis less reliable.

The stiffness tensor in attenuative media is not only complex, but also varies with frequency, which makes velocity, normalized attenuation coefficient and other quantities frequency-dependent. Our analytic expressions are derived for a fixed frequency of the harmonic plane wave and can be applied to arbitrarily dispersive models by treating the stiffnesses or Thomsen-style parameters as functions of frequency.

4.7 Conclusions

To analyze PP- and PS-wave reflection coefficients in attenuative anisotropic media, I developed linearized approximations using perturbation theory. For an incident P-wave with a zero inhomogeneity angle, the form of the linearized PP- and PS-wave reflection coefficients in arbitrarily anisotropic media is the same as in purely elastic models, but all terms become complex. The general solutions were simplified for VTI symmetry to obtain simple closed-form expressions in Thomsen-style notation.

Both analytic and numerical results show that only in the presence of strong attenuation ($Q < 10$) does the contribution of the imaginary part of the stiffness tensor (which is responsible for attenuation) become comparable to that of the real part. In particular, the influence of the attenuation-anisotropy parameters ϵ_Q and δ_Q on the PP-wave reflection coefficient typically is much weaker than that of the velocity-anisotropy parameters ϵ and δ. As expected from the parameter definitions, the PP-wave AVO gradient in attenuative media includes δ_Q, while the large-angle reflection coefficient also depends on ϵ_Q. However, the largest attenuation-related terms in the reflection coefficients for both PP- and PS-waves are proportional to the contrasts in the normalized symmetry-direction attenuation coefficients $\mathcal{A}_{P0}$ and $\mathcal{A}_{S0}$ because the contrasts in the attenuation-anisotropy parameters are scaled by the inverse quality factor $1/Q_{P0}$. Therefore, the contribution of ϵ_Q and δ_Q becomes significant only for models with uncommonly high attenuation ($Q < 10$), such as

heavy-oil-saturated rocks.

If the incident wave has a nonzero inhomogeneity angle ξ, the form of the linearized reflection coefficients is different from the conventional AVO expression. In particular, the PP-wave reflection coefficient is no longer an even function of the incidence angle θ and includes a term proportional to $\sin\theta$. Likewise, when $\xi \neq 0$, the normal-incidence PS-wave reflection coefficient (i.e., AVO intercept) does not vanish and may even attain values comparable to the AVO intercept for the PP reflection. However, the inhomogeneity angle makes a substantial contribution to the AVO response only for strongly attenuative media with $Q < 10$.

Despite the presence of a number of attenuation-related terms, our linearized AVO equations have an easily interpretable form that provides useful physical insight into the reflectivity of anisotropic attenuative media. Their application can help to avoid errors in AVO analysis and, potentially, invert prestack reflection amplitudes for the attenuation parameters.

Chapter 5

Estimation of interval anisotropic attenuation from reflection data

5.1 Summary

Knowledge of interval attenuation can be highly beneficial in reservoir characterization and lithology discrimination. Here, I combine the spectral-ratio method with velocity-independent layer stripping to develop a technique for estimation of the interval attenuation coefficient from reflection seismic data. The layer-stripping procedure is based on identifying the reflections from the top and bottom of the target layer that share the same ray segments in the overburden. The algorithm is designed for heterogeneous, arbitrarily anisotropic target layers, but the overburden is assumed to be laterally homogeneous with a horizontal symmetry plane. Although no velocity information about the overburden is needed, interpretation of the computed anisotropic attenuation coefficient involves the phase angle in the target layer. Tests on synthetic P-wave data from layered transversely isotropic and orthorhombic media confirm the high accuracy of both 2D and 3D versions of the algorithm. I also demonstrate that the interval attenuation estimates are independent of the inhomogeneity angle of the incident and reflected waves.

5.2 Introduction

The attenuation coefficient of subsurface rocks is closely linked to their lithology and physical properties. In particular, attenuation may serve as an indicator of permeability, mobility of fluids, and fluid saturation (e.g., Winkler & Nur, 1982; Batzle *et al.*, 2006; Behura *et al.*, 2007). A number of laboratory measurements (Hosten *et al.*, 1987; Tao & King, 1990; Prasad & Nur, 2003; Behura *et al.*, 2006) and field studies (Ganley & Kanasewich, 1980; Liu *et al.*, 2007; Maultzsch *et al.*, 2007) indicate that attenuation can be strongly anisotropic

(directionally-dependent) because of the preferential alignment of fractures, interbedding of thin attenuative layers, and/or nonhydrostatic stress. Furthermore, the symmetry of attenuation anisotropy may be different from that of velocity anisotropy (Maultzsch *et al.*, 2007; Zhu *et al.*, 2007a). Therefore, measurements of attenuation anisotropy may provide valuable additional information about the properties of anisotropic (e.g., fractured) reservoirs (Liu *et al.*, 2007).

Most existing attenuation estimates from reflection data (e.g., Vasconcelos & Jenner, 2005) are obtained for the whole section above the reflecting interface. Dasgupta & Clark (1998) introduce a technique for estimating interval attenuation from reflection data based on the spectral-ratio method. Their algorithm, however, is restricted to zero-offset reflections and requires knowledge of the source signature. Moreover, they suggest to apply the NMO stretch prior to attenuation analysis, which may distort the estimated attenuation values.

Here, I present a method for computing the *interval* attenuation coefficient using an extension of the layer-stripping technique originally introduced by Dewangan & Tsvankin (2006) for reflection traveltimes. Our algorithm reconstructs the offset-dependent interval attenuation in a heterogeneous, arbitrarily anisotropic target layer without knowledge of the velocity and attenuation in the overburden. Synthetic examples for layered VTI (transversely isotropic with a vertical symmetry axis) and orthorhombic media confirm the accuracy of our method and its high potential in the inversion for the interval attenuation-anisotropy parameters.

5.3 Methodology

I consider a pure-mode (PP or SS) reflection in a medium that includes an anisotropic, heterogeneous target layer under a laterally homogeneous overburden with a horizontal symmetry plane (Figure 5.1). For simplicity, the layer-stripping technique is introduced here in 2D, although I have also implemented it for 3D wide-azimuth data (see below). To make wave propagation two-dimensional, the vertical incidence plane has to coincide with a plane of symmetry in all layers including the target. As discussed by Dewangan & Tsvankin (2006), this restriction becomes unnecessary in the 3D extension of the layer-stripping method.

The exact interval traveltime-offset function in the target layer can be constructed by combining the target event with reflections from the bottom of the overburden (Fig-

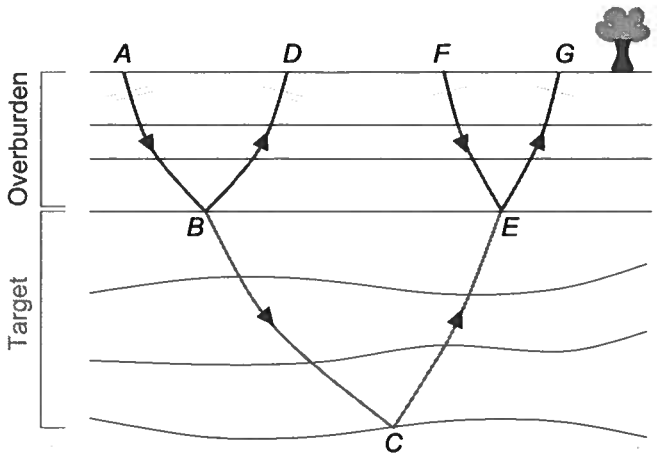

Figure 5.1: 2D ray diagram of the layer-stripping algorithm. Points B and E are located at the bottom of the overburden. The target reflection $ABCEG$ and the reflection ABD from the bottom of the overburden share the same downgoing leg AB. The upgoing leg EG of the target event coincides with a leg of another overburden reflection, GEF.

ure 5.1). Dewangan & Tsvankin (2006) show that by matching the time slopes (slownesses) on common-receiver gathers, it is possible to identify the overburden reflections ABD and GEF that share the downgoing (AB) and upgoing (EG) legs with the target event $ABCEG$. Under the assumptions made above, any reflection point at the bottom of the overburden (e.g., points B and E in Figure 5.1) coincides with the common midpoint for the corresponding source-receiver pair, and the traveltimes along the downgoing and upgoing segments of the reflected ray are equal to each other. Therefore, the interval traveltime in the target layer along the path BCE can be found from

$$t_{BCE} = t_{ABCEG} - \frac{t_{ABD} + t_{GEF}}{2}, \tag{5.1}$$

where t_{ABCEG}, t_{ABD}, and t_{GEF} are the traveltimes along the raypaths $ABCEG$, ABD, and GEF, respectively. Implementation of the kinematic velocity-independent layer-stripping algorithm is described in more detail by Dewangan & Tsvankin (2006).

Here, I extend this layer-stripping technique to attenuation analysis by applying the spectral-ratio method to a specific combination of the target and overburden events. Since the overburden is laterally homogeneous and has a horizontal symmetry plane, $l_{AB} = l_{BD}$

and $l_{EG} = l_{FE}$, where l_{XY} is the distance along the raypath XY. The ray-theory amplitudes of the target and overburden reflections in the frequency domain can be written as

$$|U_{ABCEG}(\omega)| = S(\omega)\,\mathcal{G}_{ABCEG}\,e^{-k^I_{g,O}(l_{AB}+l_{EG})}\,e^{-k^I_{g,T}(l_{BC}+l_{CE})}, \tag{5.2}$$

$$|U_{ABD}(\omega)| = S(\omega)\,\mathcal{G}_{ABD}\,e^{-k^I_{g,O}(l_{AB}+l_{BD})} = S(\omega)\,\mathcal{G}_{ABD}\,e^{-2k^I_{g,O}\,l_{AB}}; \tag{5.3}$$

and

$$|U_{GEF}(\omega)| = S(\omega)\,\mathcal{G}_{GEF}\,e^{-k^I_{g,O}(l_{EG}+l_{EF})} = S(\omega)\,\mathcal{G}_{GEF}\,e^{-2k^I_{g,O}\,l_{EG}}, \tag{5.4}$$

where $k^I_{g,T}$ and $k^I_{g,O}$ ("I" stands for the imaginary part of the wavenumber) are the average group attenuation coefficients in the target layer and overburden, respectively, $S(\omega)$ is the spectrum of the source wavelet, and the parameters $\mathcal{G}_{ABD}$, $\mathcal{G}_{GEF}$, and $\mathcal{G}_{ABCEG}$ include the source/receiver radiation patterns as well as the plane-wave reflection/transmission coefficients and geometrical spreading along the corresponding raypaths. The frequency-domain amplitudes of the target and overburden reflections are obtained by windowing the corresponding arrivals and applying the Fourier transform.

To eliminate the contribution of the overburden along with the source wavelet, equations 5.2, 5.3, and 5.4 can be combined in the following way:

$$ln\left(\frac{|U_{ABCEG}(\omega)|^2}{|U_{ABD}(\omega)|\,|U_{GEF}(\omega)|}\right) = ln(\mathcal{G}) - 2k^I_{g,T}(l_{BC}+l_{CE}), \tag{5.5}$$

where the term $\mathcal{G} = \mathcal{G}^2_{ABCEG}/(\mathcal{G}_{ABD}\mathcal{G}_{GEF})$ is assumed to be independent of frequency. Equation 5.5 can be used to estimate the interval attenuation coefficient in the target layer without knowledge of the source wavelet and overburden parameters.

For an arbitrarily heterogeneous target layer, the attenuation coefficient varies along the ray, and $k^I_{g,T}$ in equation 5.5 represents the average value along the raypath BCE. However, if the target layer is horizontal, homogeneous, and has a horizontal symmetry plane (or is purely isotropic), then $l_{BC}+l_{CE} = V_g\,t_{BCE}$, where V_g is the group velocity along the rays BC and CE. Then equation 5.5 takes the form

$$ln\left(\frac{|U_{ABCEG}(\omega)|^2}{|U_{ABD}(\omega)|\,|U_{GEF}(\omega)|}\right) = ln(\mathcal{G}) - 2\,k^I_{g,T}\,V_g\,t_{BCE}. \tag{5.6}$$

The coefficient k^I_g generally differs from the phase attenuation coefficient k^I, which can

be obtained analytically from the Christoffel equation (e.g., Zhu & Tsvankin, 2006). If the inhomogeneity angle (the angle between the real and imaginary parts of the wave vector; see Figure 5.2) is zero, the group and phase attenuation coefficients are related by $k_g^I = k^I \cos\psi$, where ψ is the angle between the group- and phase-velocity vectors (Zhu, 2006; Behura & Tsvankin, 2009). Using this relationship and expressing V_g through the phase velocity V ($V_g = V/\cos\psi$), the attenuation-related term in equation 5.6 can be represented as follows (hereafter, the subscript "T" is omitted):

$$k_g^I V_g t_{BCE} = k^I V t_{BCE} = \omega \frac{k^I}{k^R} t_{BCE} = \omega \mathcal{A} t_{BCE}, \tag{5.7}$$

where $\mathcal{A} = k^I/k^R$ ($k^R = \omega/V$) is the normalized phase attenuation coefficient responsible for the rate of amplitude decay per wavelength (Zhu & Tsvankin, 2006). For isotropic media $\mathcal{A} = 1/2Q$, where Q is the quality factor widely used as a measure of intrinsic attenuation. Substitution of equation 5.7 into equation 5.6 yields

$$ln\left(\frac{|U_{ABCEG}(\omega)|^2}{|U_{ABD}(\omega)|\,|U_{GEF}(\omega)|}\right) = ln(\mathcal{G}) - 2\omega \mathcal{A} t_{BCE}. \tag{5.8}$$

To relate the group and phase attenuation coefficients, I assumed a zero inhomogeneity angle ξ in the target layer (Figure 5.2a). However, as shown by Behura & Tsvankin (2009), equation 5.8 yields the coefficient $\mathcal{A}|_{\xi=0^\circ}$ (i.e., the intrinsic attenuation) for a wide range of inhomogeneity angles. This result, explained in more detail in the discussion section, is confirmed by the synthetic examples below.

The slope of the logarithmic spectral ratio in equation 5.8 expressed as a function of ω yields the product $2\mathcal{A}t_{BCE}$. Since the interval traveltime t_{BCE} is obtained from the layer-stripping algorithm (equation 5.1), application of the spectral-ratio method to the amplitude combination in equation 5.8 can be used to compute the phase attenuation coefficient $\mathcal{A}$. In the current analysis, I assume that $\mathcal{A}$ is independent of frequency (i.e., Q is constant), and the slope of the logarithmic spectral ratio does not change within the frequency band of the signal. However, if $\mathcal{A}$ is a function of frequency, then the instantaneous slope would produce a frequency-dependent quality factor. Unless the medium exhibits anomalously strong velocity dispersion, as that in heavy oils (Behura *et al.*, 2007), the spectral-ratio method should give reliable attenuation estimates.

Therefore, our method makes it possible to obtain the normalized phase attenuation coefficient $\mathcal{A} = \mathcal{A}|_{\xi=0^\circ}$ – the quantity dependent on attenuation-anisotropy parameters. The

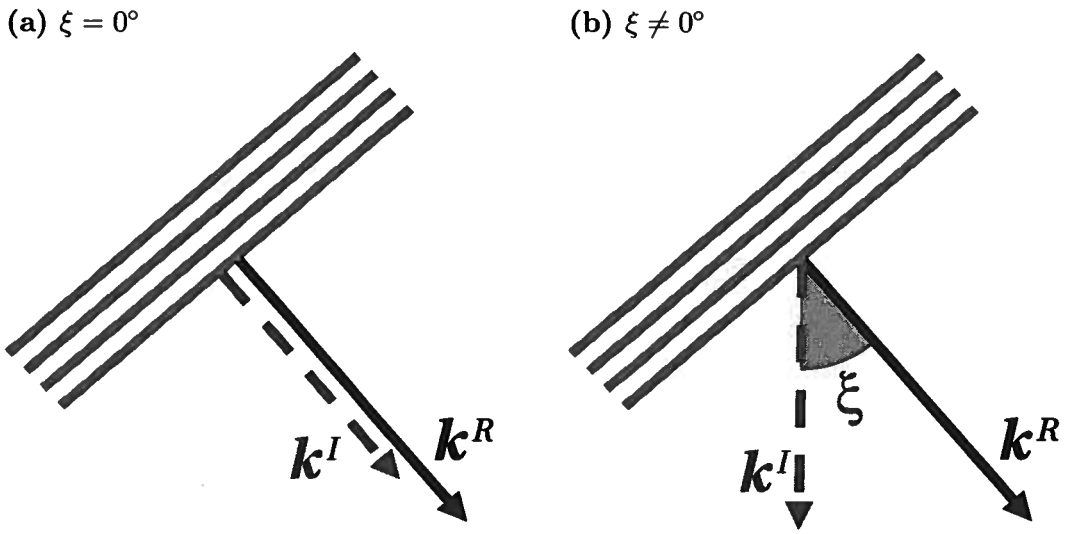

Figure 5.2: Inhomogeneity angle ξ of a plane wave in attenuative media. $\mathbf{k}^R$ and $\mathbf{k}^I$ are the real and imaginary components (respectively) of the wave vector, and θ is the phase angle with the vertical.

coefficient $\mathcal{A}$, however, is expressed analytically as a function of the corresponding phase direction (Zhu & Tsvankin, 2006). Hence, inversion of $\mathcal{A}$ for the relevant attenuation-anisotropy parameters requires knowledge of the phase angle for each source-receiver pair. This issue is addressed in more detail in the discussion section.

Computation of the interval values of $\mathcal{A}$ for different source-receiver pairs along the acquisition line can help to evaluate both the in-plane anisotropy and the lateral variation of attenuation. I also extended the methodology described here to wide-azimuth data (see the synthetic example below) using the 3D version of the layer-stripping algorithm presented by Dewangan & Tsvankin (2006) and Wang & Tsvankin (2009). In particular, Wang & Tsvankin (2009) employed the nonhyperbolic moveout equation to develop an efficient implementation of kinematic layer-stripping for wide-azimuth P-wave data from horizontally layered orthorhombic media.

5.4 Synthetic Examples

First, I test the method on synthetic P-wave reflection data generated for a horizontally stratified VTI model (Figure 5.3). Attenuation in VTI media can be conveniently charac-

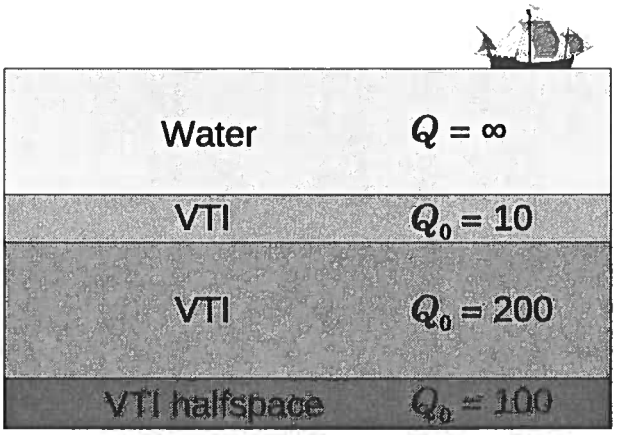

Figure 5.3: Model used to test the attenuation layer-stripping algorithm. The first layer is water (purely elastic and isotropic) with the P-wave velocity $V_P = 1500$ m/s and thickness $d = 1000$ m; the other three layers are VTI. For the second layer, the vertical P- and S-wave velocities are $V_{P0} = 1600$ m/s and $V_{S0} = 200$ m/s, $d = 300$ m, and Thomsen velocity-anisotropy parameters are $\epsilon = 0.3$ and $\delta = -0.2$; the attenuation parameters are $Q_{P0} = 10$, $Q_{S0} = 10$, $\epsilon_Q = -0.5$, and $\delta_Q = -1.0$. The third layer has $V_{P0} = 2000$ m/s, $V_{S0} = 1000$ m/s, $d = 1000$ m, $\epsilon = 0.1$, $\delta = 0.6$, $Q_{P0} = 200$, $Q_{S0} = 200$, $\epsilon_Q = -0.3$, and $\delta_Q = 1.0$. For the bottom halfspace, $V_{P0} = 2200$ m/s, $V_{S0} = 1100$ m/s, $\epsilon = 0$, $\delta = -0.2$, $Q_{P0} = 100$, $Q_{S0} = 100$, $\epsilon_Q = 0.5$, and $\delta_Q = 0.5$.

terized using the Thomsen-style parameters ($\mathcal{A}_{P0} \approx 1/2Q_{P0}$, $\mathcal{A}_{S0} \approx 1/2Q_{S0}$, ϵ_Q, δ_Q, γ_Q) introduced by Zhu & Tsvankin (2006). $\mathcal{A}_{P0}$ and $\mathcal{A}_{S0}$ are the normalized symmetry-direction attenuation coefficients of P- and S-waves, respectively, ϵ_Q and δ_Q control the angular variation of the P- and SV-wave attenuation coefficients, and γ_Q governs SH-wave attenuation anisotropy.

Figure 5.4a displays a shot gather computed for the model in Figure 5.3 by an anisotropic reflectivity code (Schmidt & Tango, 1986). Note that the reflections from the bottom of the attenuative layers have a much lower frequency content than the water-bottom event (Figure 5.4b). Although the second layer has uncommonly strong attenuation ($\mathcal{A}_{P0} = 1/2Q_{P0} = 0.05$), the estimated interval attenuation coefficient is close to the exact values for a wide range of propagation directions (Figure 5.5a). Attenuation coefficients for phase angles exceeding 40° are missing because of the limited acquisition aperture. The estimated interval attenuation in the third layer (Figure 5.5b) is accurate only up to 30°. For larger

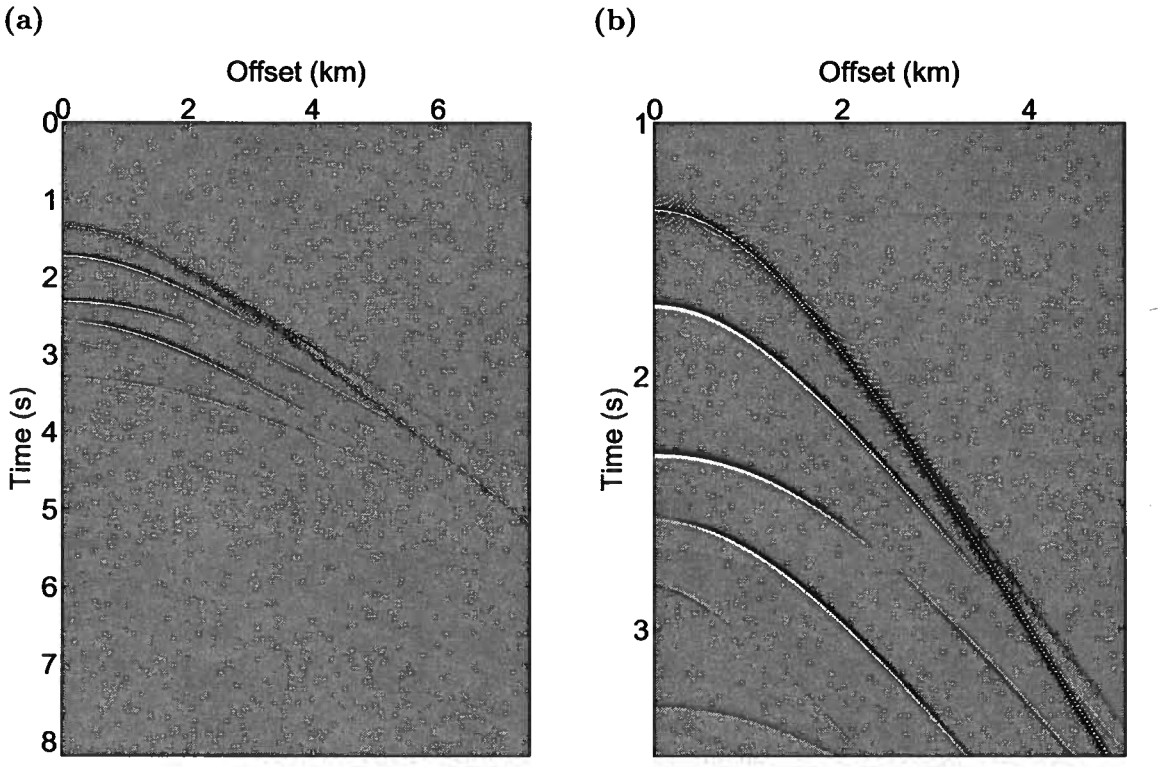

Figure 5.4: (a) Shot gather computed for the model in Figure 5.3. (b) A blow-up of the gather showing reflections with different frequency content.

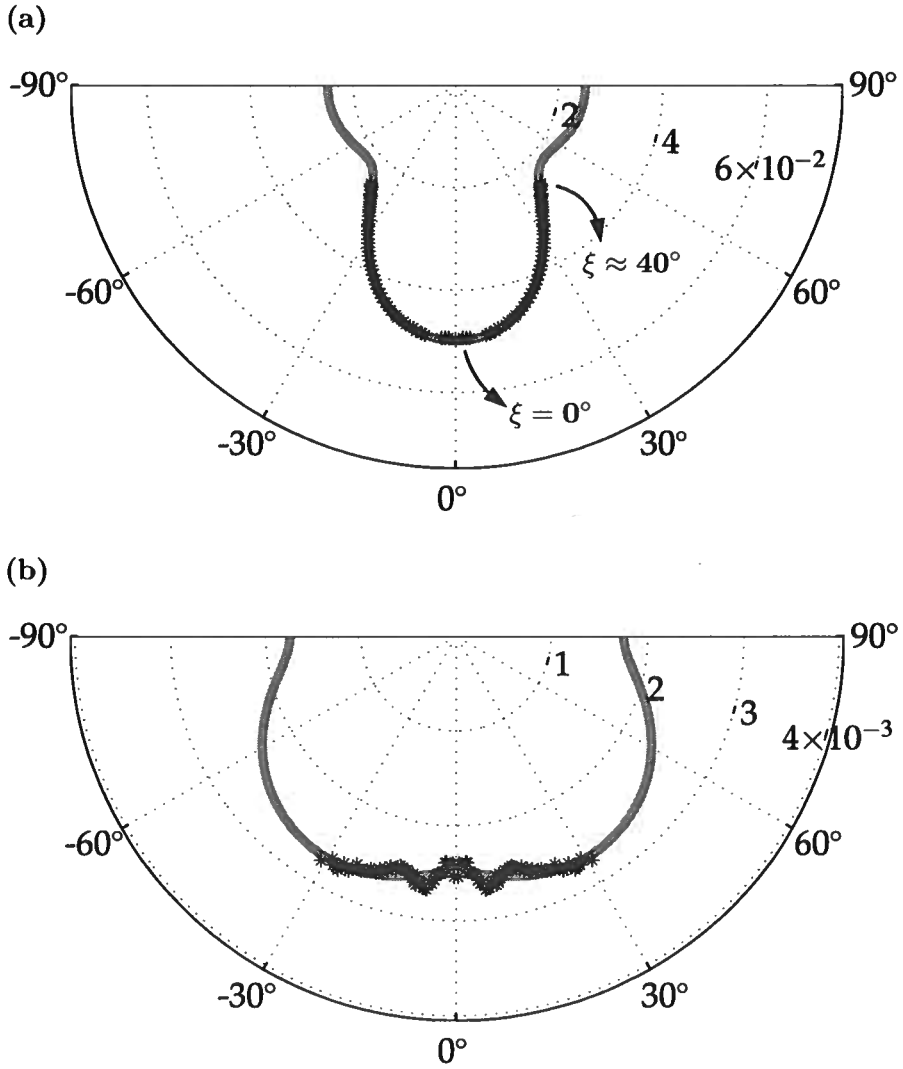

Figure 5.5: Normalized interval phase attenuation coefficient $\mathcal{A}$ (stars) estimated as a function of the phase angle (in degrees) for the second (a) and third (b) layers of the model from Figure 5.3. The solid gray lines mark the exact values of $\mathcal{A}|_{\xi=0°}$.

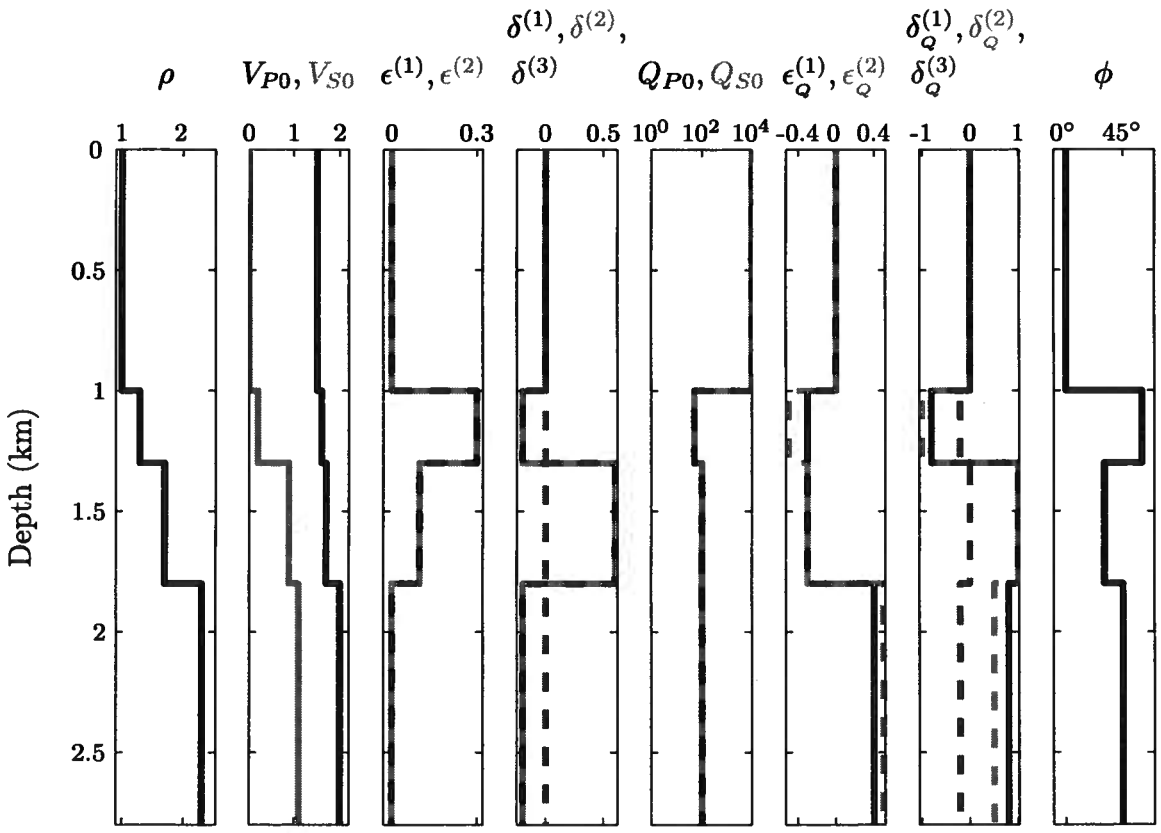

Figure 5.6: Horizontally layered model used to test the 3D attenuation layer-stripping algorithm. The velocity and density are in km/s and g/cm^3. ϕ is the azimuth of the $[x_1, x_3]$ symmetry plane in the orthorhombic layers. The values of different parameters are shown by the corresponding colors.

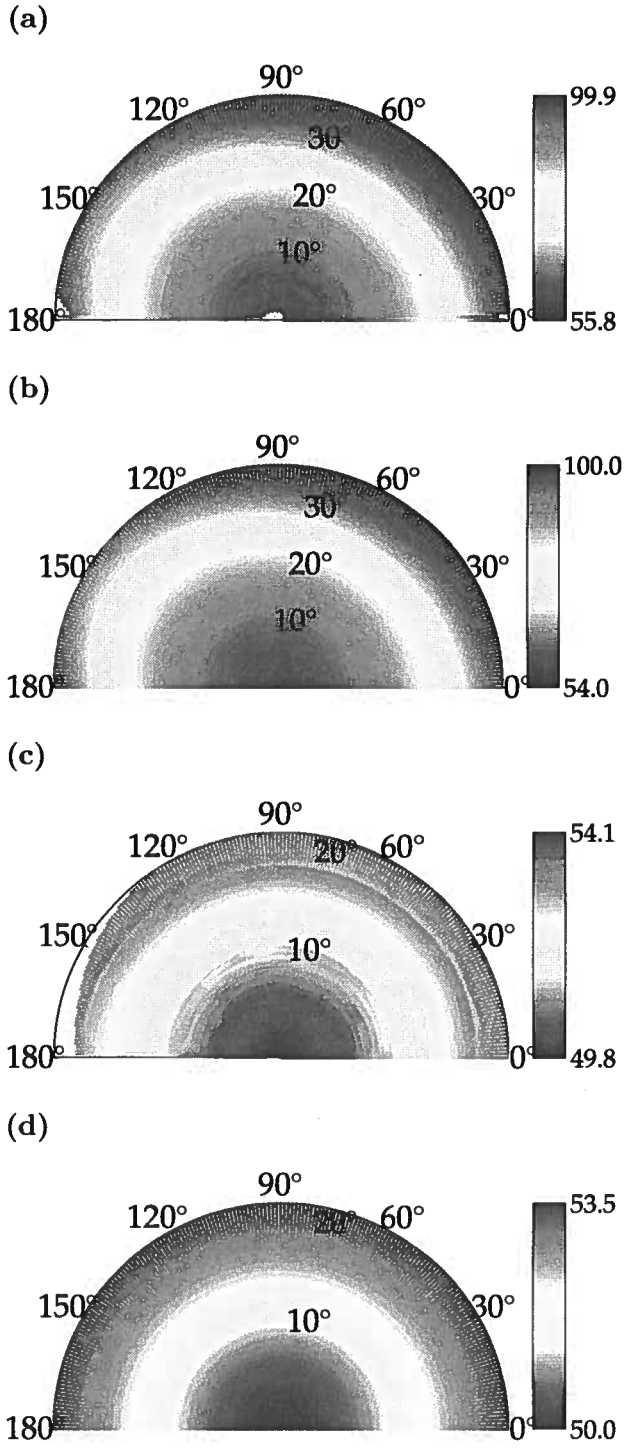

Figure 5.7: Estimated interval phase attenuation coefficient $\mathcal{A}$ as a function of the phase direction for the second (a) and third (c) layers of the model from Figure 5.6. The exact $\mathcal{A}|_{\xi=0^\circ}$ in the second (b) and third (d) layers is shown for comparison. All attenuation coefficients are multiplied by 100. The radial axis represents the polar phase angle, and the azimuth is marked on the perimeter.

angles the target reflection interferes with the direct arrival and other events, which impairs the performance of the spectral-ratio method. Interference-related distortions can be mitigated by operating in the τ–p domain or suppressing the direct arrival and ground roll before layer stripping.

The 3D version of the layer-stripping method was applied to wide-azimuth P-wave data computed for the model in Figure 5.6. The second and fourth layers exhibit orthorhombic attenuation anisotropy with different azimuths of the vertical symmetry planes, while the third layer is VTI. Directionally-dependent attenuation coefficients in orthorhombic media can be described using a notation similar to that developed by Tsvankin (1997) for the velocity function. This parameter set includes the P- and S-wave vertical attenuation coefficients ($\mathcal{A}_{P0}$ and $\mathcal{A}_{S0}$) and seven anisotropy parameters - $\epsilon_Q^{(1,2)}$, $\delta_Q^{(1,2,3)}$, and $\gamma_Q^{(1,2)}$ (Zhu & Tsvankin, 2007).

The estimated interval attenuation coefficient $\mathcal{A}$ in the second (orthorhombic) layer (Figure 5.7a) practically coincides with the exact $\mathcal{A}$ (Figure 5.7b) for the whole range of the polar and azimuthal phase angles. The interval attenuation in the third layer (VTI) is also reconstructed with high accuracy (Figures 5.7c,d). As was the case for the 2D example, the minor difference between the exact and computed attenuation coefficients is caused primarily by interference of the overburden and target reflections with other events.

5.5 Discussion

Although the relationship between the group and phase attenuation coefficients used in our derivation was originally proved for a zero inhomogeneity angle ξ (Figure 5.2a), our method remains accurate for a wide range of ξ. Indeed, as shown by Behura & Tsvankin (2009), application of equations 5.6 and 5.7 for nonzero inhomogeneity angles yields the normalized phase attenuation coefficient $\mathcal{A}$ corresponding to $\xi = 0°$ ($\mathcal{A}|_{\xi=0°}$). This conclusion, which remains valid even for large angles ξ up to 80° and media with the quality factor Q as low as 10, is confirmed by the tests in Figures 5.5 and 5.7. Our algorithm produces accurate values of $\mathcal{A}|_{\xi=0°}$ even for long offsets where the inhomogeneity angle ξ of the incident and reflected waves reaches 40°.

The coefficient $\mathcal{A}|_{\xi=0°}$ quantifies the intrinsic angle-dependent attenuation of a particular wave mode. For P-waves in TI media, the phase attenuation coefficient linearized in

the anisotropy parameters is given by (Zhu & Tsvankin, 2006)

$$\mathcal{A}|_{\xi=0^\circ} = \mathcal{A}_{P0}\left(1 + \delta_Q \sin^2\theta \cos^2\theta + \epsilon_Q \sin^4\theta\right), \tag{5.9}$$

where θ is the phase angle with the symmetry axis. Equation 5.9 has the same form as the well-known Thomsen (1986) weak-anisotropy approximation for the P-wave phase-velocity function. Zhu & Tsvankin (2007) present a similar linearized expression for the coefficient $\mathcal{A}|_{\xi=0^\circ}$ of P-waves in attenuative orthorhombic media.

As demonstrated by Zhu *et al.* (2007b) on physical-modeling data, equation 5.9 can be used to invert attenuation measurements for the anisotropy parameters ϵ_Q and δ_Q. In the presence of strong velocity anisotropy, the inversion should be based on the exact solution for $\mathcal{A}|_{\xi=0^\circ}$ obtained from the Christoffel equation.

Note that estimation of the angle θ in an anisotropic target layer generally requires knowledge of the velocity field. Because the influence of attenuation on velocity for a fixed frequency typically is of the second order (Zhu & Tsvankin, 2006), velocity analysis can be performed prior to attenuation processing using the interval traveltime. Anisotropic velocity estimation, however, is often ill-posed without *a priori* information (e.g., the layer thickness). For example, P-wave reflection moveout in a horizontal VTI layer does not constrain reflector depth and, therefore, the group or phase angle for a given source-receiver pair. Still, given typical uncertainties in amplitude measurements, errors in the phase angle are not expected to produce substantial distortions in the attenuation coefficients for moderately anisotropic media.

5.6 Conclusions

I extended velocity-independent layer stripping to amplitude analysis and employed the spectral-ratio method to estimate interval offset- and azimuth-dependent attenuation from reflection data. While there are no restrictions on heterogeneity and anisotropy in the target horizon, the overburden has to be composed of laterally homogeneous layers with a horizontal symmetry plane (e.g., layers may be orthorhombic). It should be emphasized that our attenuation layer stripping is data-driven and does not require knowledge of the overburden velocity and attenuation parameters. In general, the algorithm estimates the average interval group attenuation coefficient along the raypath of a reflected wave. However, for homogeneous target layers it is possible to reconstruct the normalized phase attenuation

coefficient $\mathcal{A}$ for each source-receiver pair. The coefficient $\mathcal{A}$ represents a measure of intrinsic attenuation and can be inverted for the interval attenuation-anisotropy parameters.

Numerical examples for horizontally layered VTI and orthorhombic media confirm that the method yields accurate interval phase attenuation coefficients even for models with uncommonly strong attenuation and substantial velocity and attenuation anisotropy. The algorithm is designed to process isolated overburden and target reflections, so the results may be distorted by interference with other events. As any other layer-stripping technique, the interval attenuation coefficient may become inaccurate for relatively thin layers.

The attenuation coefficient in a reservoir can help to predict the presence and distribution of hydrocarbons (e.g., to distinguish between steam and heat fronts in heavy-oil reservoirs). The 3D version of the method can be used to estimate the azimuthally varying interval attenuation coefficient, which represents a sensitive attribute for fracture characterization and reconstruction of the stress field.

Chapter 6

A case study of interval attenuation analysis

6.1 Summary

Attenuation can be extremely valuable in characterizing gas sands. In fractured reservoirs, attenuation anisotropy can provide additional information about the distribution of fractures. Here, I apply the layer-stripping approach to wide-azimuth P-wave data acquired over a gas reservoir in the Coronation Field, Alberta. The main processing steps involve estimation of traveltimes from the top and bottom of the target layer followed by computation of the interval attenuation using the spectral-ratio technique.

The lower half of the survey area shows strong azimuthal velocity anisotropy with the vertical symmetry planes aligned consistently along the NS- and EW-directions. The vertical attenuation coefficient shows a reasonable correspondence with existing gas-producing well locations. The interval attenuation anisotropy is anomalously strong and much higher than velocity anisotropy. More comprehensive reservoir characterization requires additional data.

6.2 Introduction

Laboratory studies clearly indicate that attenuation is closely related to fluid saturation and mobility (Spencer, 1979; Gautam *et al.*, 2003). Well-log analysis by Klimentos (1995) shows that P-wave attenuation is higher in gas-bearing rocks than in those saturated with oil or water. He observed extremely low P-wave quality factors (Q), ranging between 5 and 10, in a gas reservoir. Similar low Q-values in gas sands are observed by Mavko & Dvorkin (2005) in well-logs from the Gulf Coast.

Attenuation anisotropy might carry a wealth of information about fluid- or gas-filled fractures. In fact, preferential flow of fluids in rocks is believed to be the primary cause of attenuation anisotropy (e.g., Mavko & Nur, 1979; Akbar *et al.*, 1993; Parra, 1997; MacBeth,

1999; Brajanovski *et al.*, 2005). Using different fluid-flow models, Pointer *et al.* (2000) show that aligned fluid-filled cracks can result in anisotropic attenuation. The poroelastic model of Chapman (2003) can explain strong anisotropic attenuation in the seismic bandwidth. Vasco *et al.* (1996) observe attenuation anomalies coinciding with highly fractured zones in a borehole near Raymond, California. Parra *et al.* (2002) make similar observation of low Q-values from cross-well studies in fractured zones of a shale-sand sequence. They also record strong attenuation anisotropy with the vertical attenuation coefficient five times larger than the horizontal coefficient. Vertical seismic profiling (VSP) studies by Varela *et al.* (2006) and Maultzsch *et al.* (2007) show attenuation anisotropy which they attribute to fluid-filled fractures.

In Chapter 5 I introduced a layer-stripping technique to extract interval attenuation from reflection data that implements a variation of the spectral-ratio method (Johnston & Toksöz, 1981). While no information about velocity and attenuation anywhere in the medium is required, the overburden has to be laterally homogeneous with a horizontal symmetry plane. Using synthetic examples for VTI and orthorhombic models, I demonstrated that this algorithm can successfully estimate the interval anisotropic attenuation in 2D and 3D. Here, I apply this technique to wide-azimuth data acquired at Coronation Field, Alberta and investigate the distribution of gas accumulation and fracturing using the obtained velocity and attenuation fields. The preliminary results of the velocity and attenuation analysis are presented here.

6.3 Geologic Setting

The Coronation field is a gas reservoir located in East Central Alberta (Figure 6.1). The reservoir is part of the Western Canadian Sedimentary Basin with the hydrocarbon production mostly from the Mannville Group. The Mannville Group is of Cretaceous age and corresponds to a major episode of subsidence and sedimentation following a long period of uplift, exposure, and erosion of older strata (Putnam, 1982; Hayes *et al.*, 2008). It overlies a Paleozoic unconformity and is unconformably overlain by the marine shales of Joli Fou Formation (Colorado Group). The Joli Fou shales form the cap rock and the Lower Cretaceous shales and coals are believed to be the source of the hydrocarbons (Masters, 1984). The Mannville Group is usually divided into the Upper and Lower Mannville units based on sandstone lithology (Figure 6.2); the Lower unit is more rich in quartz and chert while the Upper unit has a more feldspathic and volcanic composition. Besides sandstones,

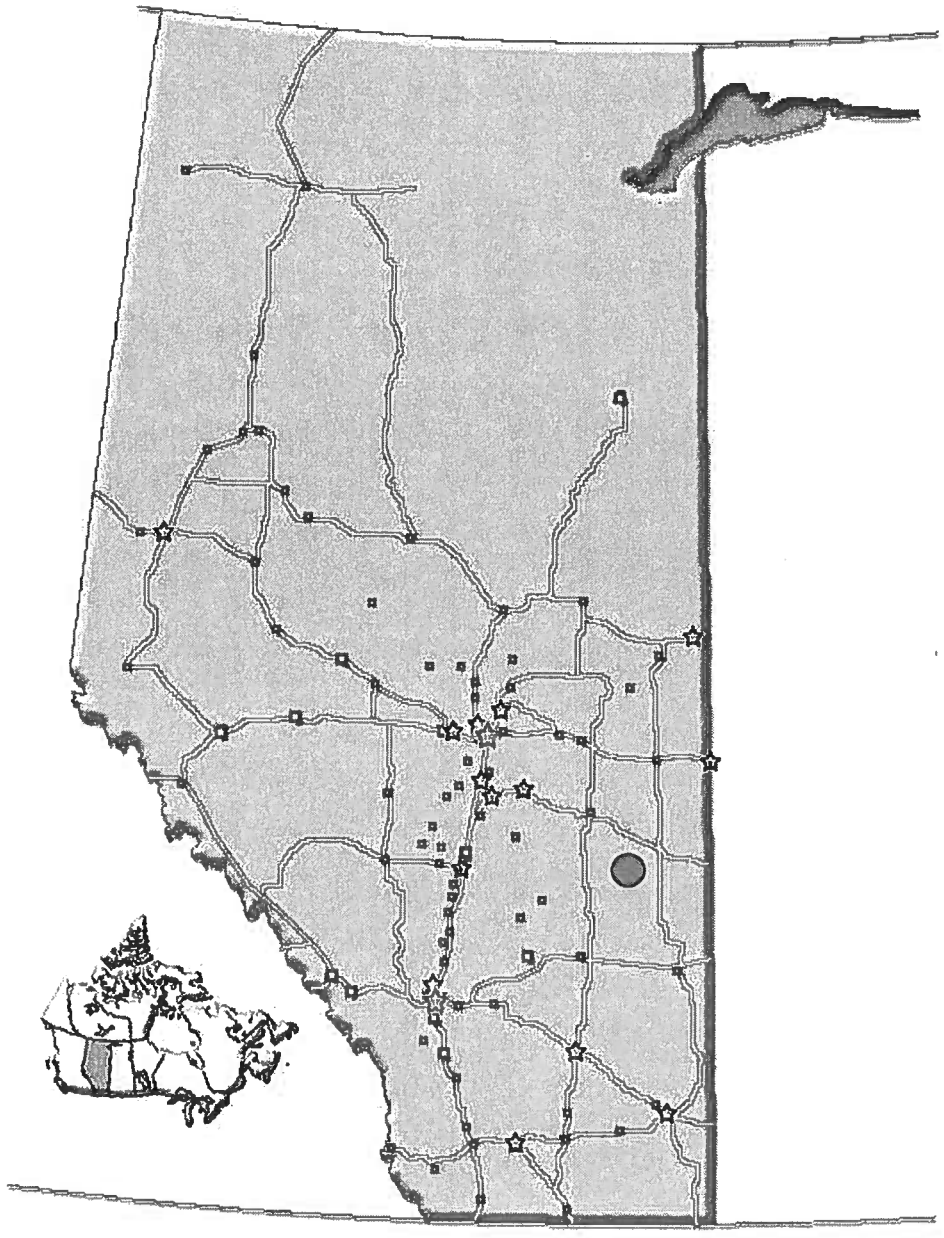

Figure 6.1: Location of the Coronation Field (red dot) in Alberta, Canada.

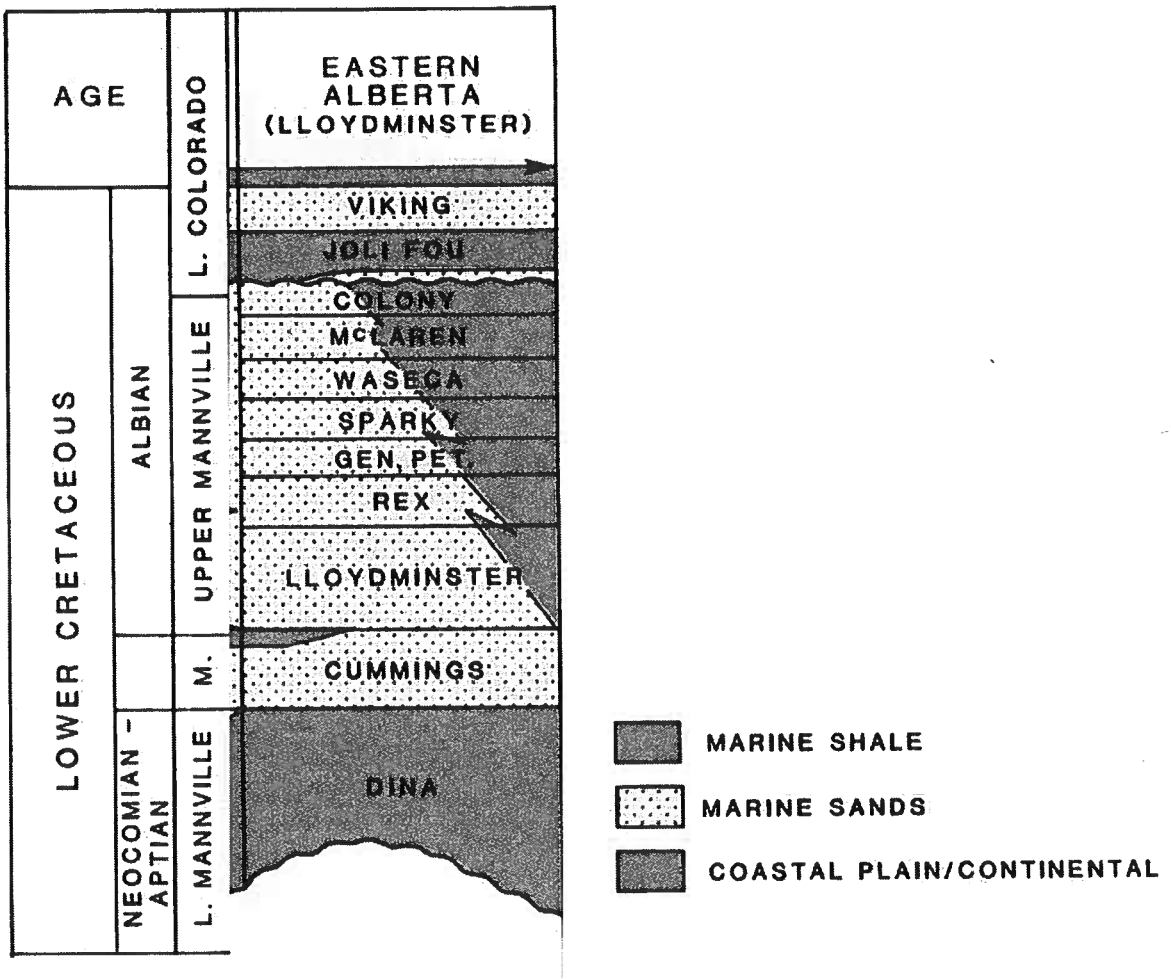

Figure 6.2: Stratigraphic column of the regional geology at Coronation Field (Jackson, 1984). The reservoir sandstones of Mannville are bounded by the Joli Fou shales above and the Paleozoic unconformity below.

the lithology of the Mannville Group comprises non-marine shales, coal seams, and minor marine shale (Putnam, 1982). Light oil and gas are usually trapped in numerous fluvial and valley-fill reservoir sandstones, while heavy oil is found in more regionally extensive shoreline sand complexes in the northern and central parts of Alberta and Saskatchewan.

The interval of primary interest at Coronation Field is the Rex member of the Mannville Group (Monk *et al.*, 2006). The sand channels immediately underlie the coals of the Rex member and could vary in thickness from 4 m to 10 m. The width of these channel systems ranges between 200 m and 300 m. Good producers yield approximately 500 MCF of gas per day with the total production of nearly 0.7 BCF per well. Because of the high cost of developing this field, drilling success needs to be high.

6.4 Data Acquisition and Processing

To understand the lithology of the channel sands and help optimize well placement, Apache Corporation acquired a 3D multicomponent seismic survey. In this study, I use only the vertical-component data to estimate the P-wave velocity and attenuation fields. The entire survey was shot using single-hole dynamite on a "shoot and roll" template of 12×94 receivers (Table 6.1) with the source at the center of the patch. This shooting template is roughly square yielding an excellent azimuthal and offset distribution. The shot lines are oblique to the receiver lines, as shown in Figure 6.3. The subsurface structure is fairly close to layer-cake (no structural dip, Figure 6.4), which facilitates the layer-stripping technique described in Chapter 5.

Prior to attenuation analysis, refraction statics corrections were applied to the data, which were shifted to a smooth floating datum. Some traces were subsequently edited to remove spikes and random noise. Denoising was followed by three passes of residual statics corrections. The ground roll was suppressed using f-k filtering followed by a surface-consistent median-gain process applied to account for the variation in the dynamite source strength.

The most critical step in estimating interval parameters is to pick traveltimes of reflections from the top and bottom of the target layer which can be done using either an auto-picker or semblance analysis. Here, I use the 3D nonhyperbolic semblance algorithm

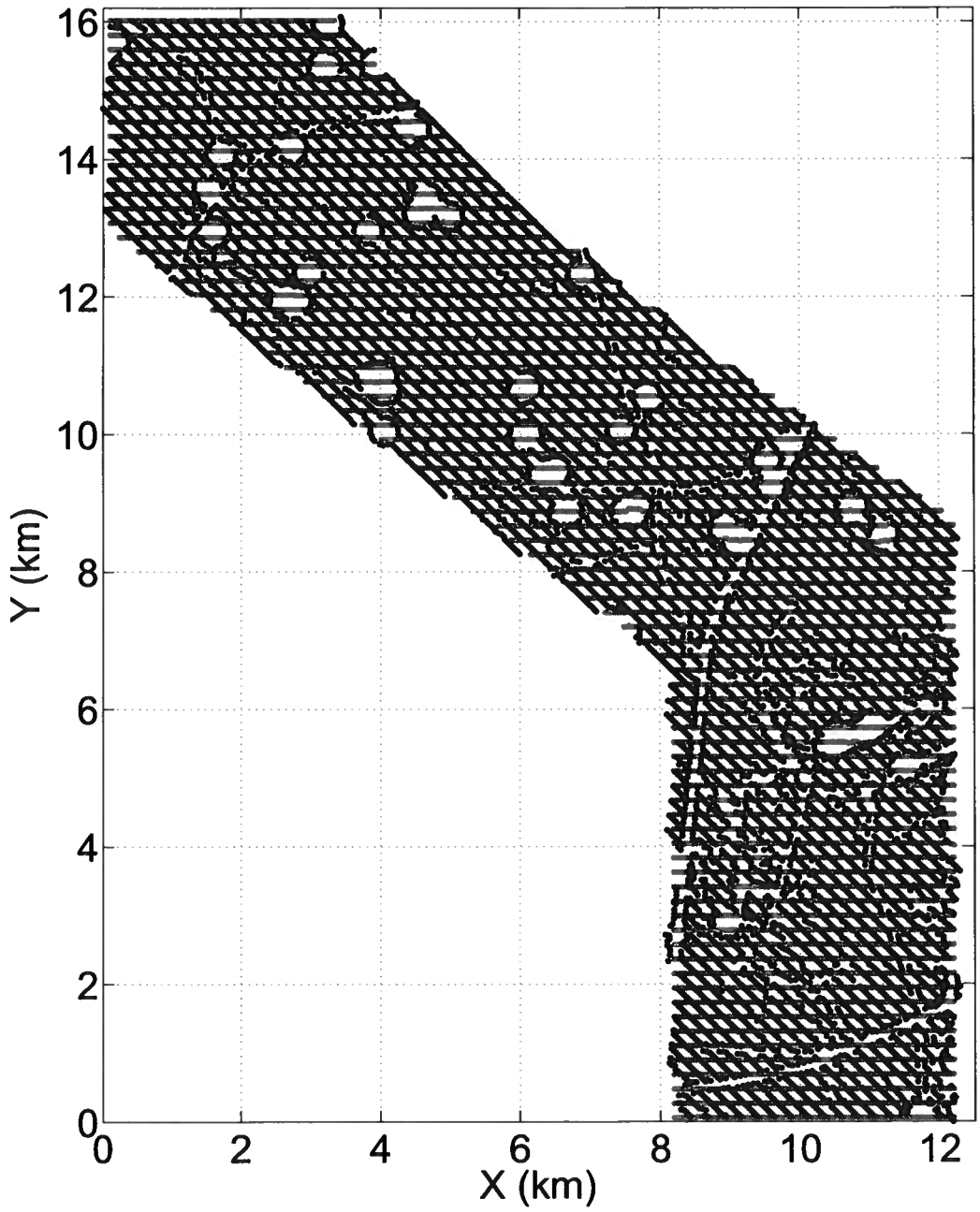

Figure 6.3: Seismic acquisition grid for the 3-C survey at Coronation Field. The black dots represent the shot locations while the receiver locations are marked with red dots.

Survey type	3D 3-C
Shot interval	42.43 m; single hole dynamite
Shot line interval	240 m
Receiver interval	30 m
Receiver line interval	210 m
Receiver patch	12 × 94 receivers
Total survey shots	11174
Total survey receivers	11255
Nominal fold (30 m × 30 m bins)	140
Maximum offset	2060 m

Table 6.1: Acquisition parameters of the survey (Monk *et al.*, 2006).

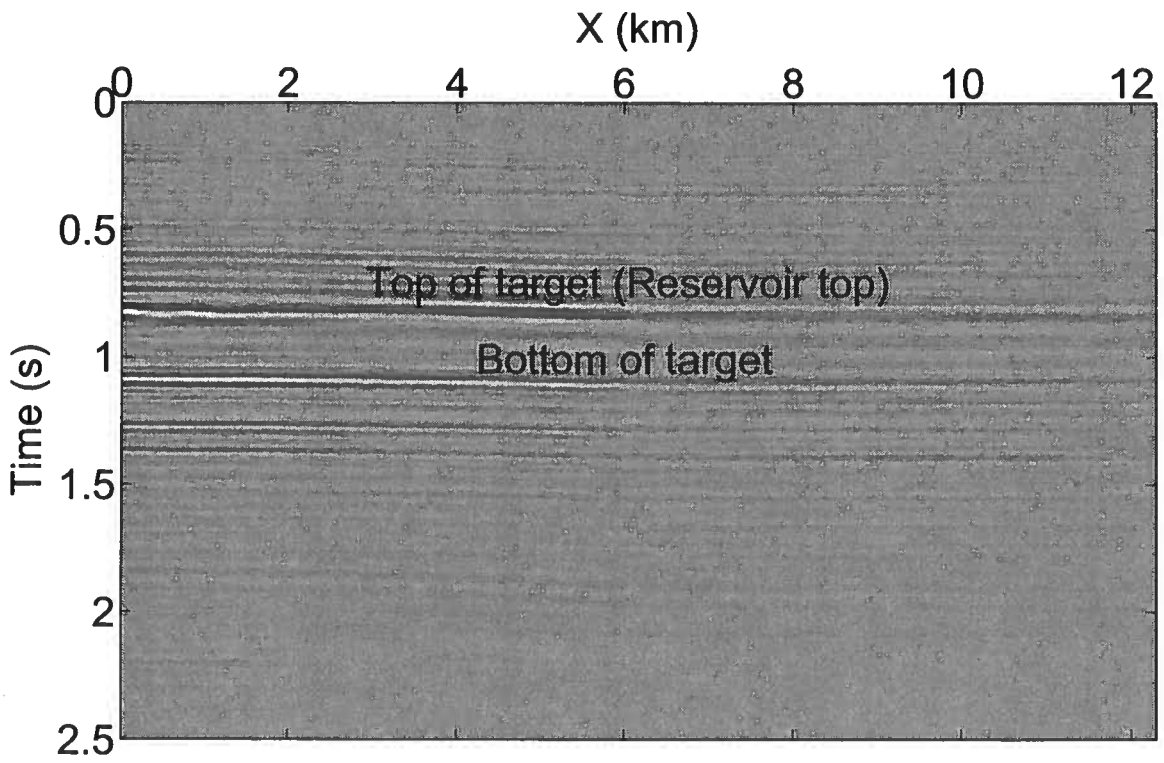

Figure 6.4: Seismic section spanning the whole length of the survey. The reflectors bounding the interval of interest are marked.

of Vasconcelos & Tsvankin (2006) for orthorhombic media based on the following equation:

$$t^2(x,\alpha) = t_0^2 + \frac{x^2}{V_{\rm nmo}^2(\alpha)} - \frac{2\eta(\alpha)\,x^4}{V_{\rm nmo}^2(\alpha)[t_0^2\,V_{\rm nmo}^2(\alpha) + (1+2\eta(\alpha))x^2]}\,, \tag{6.1}$$

where x is the offset, t_0 is the two-way zero-offset reflection traveltime, α is the source-to-receiver azimuth, $V_{\rm nmo}(\alpha)$ is the azimuthally-varying normal-moveout velocity, and $\eta(\alpha)$ is the "anellipticity" coefficient responsible for the deviation from hyperbolic moveout at long offsets. The velocity $V_{\rm nmo}(\alpha)$ is obtained from the equation of the NMO ellipse:

$$V_{\rm nmo}^{-2}(\alpha) = \frac{\sin^2(\alpha-\varphi)}{\left[V_{\rm nmo}^{(1)}\right]^2} + \frac{\cos^2(\alpha-\varphi)}{\left[V_{\rm nmo}^{(2)}\right]^2}\,; \tag{6.2}$$

φ is the azimuth of the $[x_1, x_3]$ symmetry plane, and $V_{\rm nmo}^{(1)}$ and $V_{\rm nmo}^{(2)}$ are the NMO velocities in the vertical symmetry planes $[x_2, x_3]$ and $[x_1, x_3]$, respectively. The parameter η is approximately given by (Pech & Tsvankin, 2004; Xu & Tsvankin, 2006):

$$\eta(\alpha) = \eta^{(1)}\sin^2(\alpha-\varphi) + \eta^{(2)}\cos^2(\alpha-\varphi) - \eta^{(3)}\sin^2(\alpha-\varphi)\cos^2(\alpha-\varphi)\,, \tag{6.3}$$

where $\eta^{(1)}$, $\eta^{(2)}$, and $\eta^{(3)}$ are the anellipticity coefficients defined in the $[x_2, x_3]$, $[x_1, x_3]$, and $[x_1, x_2]$ symmetry planes, respectively.

For stratified media, however, equation 6.3 is no more valid. Xu *et al.* (2005) modify equation 6.3 by introducing an additional angle φ_η:

$$\eta(\alpha) = \eta^{(1)}\sin^2(\alpha-\varphi_\eta) + \eta^{(2)}\cos^2(\alpha-\varphi_\eta) - \eta^{(3)}\sin^2(\alpha-\varphi_\eta)\cos^2(\alpha-\varphi_\eta)\,. \tag{6.4}$$

For aligned vertical symmetry planes in all layers, $\varphi_\eta = \varphi$. The semblance algorithm estimates the parameters of the NMO ellipse ($V_{\rm nmo}^{(1,2)}$ and φ) and the anellipticity parameters $\eta^{(1,2,3)}$ and φ_η.

The semblance algorithm of Vasconcelos & Tsvankin (2006) is designed to operate strictly on CMP gathers. Implementation of the layer-stripping algorithm described in Chapter 5, however, requires traveltime surfaces on source and receivers gathers. By assuming not just the overburden, but also the target layer to be laterally homogeneous, one can apply the above semblance analysis to source and receiver gathers. Since we need the horizontal slowness at both the source and receiver locations, the best-fit effective moveout

parameters are computed for the source gathers gathers as well as receiver gathers. The wide-azimuth reflection traveltimes for the top and bottom of the target layer are used for estimating the interval traveltime, as described by Dewangan & Tsvankin (2006) in 2D and Wang & Tsvankin (2009) for 3D wide-azimuth data.

The interval traveltime and windowed events along the moveout curves serve as the input data to estimate the interval attenuation estimation using the technique described in Chapter 5. The presence of notches in the source amplitude spectra complicates the Q-estimation using the spectral-ratio method. To overcome this problem, I compute the instantaneous Q at every frequency followed by median filtering to eliminate spikes. The resulting average over the Q values is taken as a measure of attenuation along the raypath. The additional advantage of computing the instantaneous Q is that it provides a measure of the variance of the normalized attenuation coefficient $\mathcal{A}$.

To improve the azimuthal and offset coverage, I gather all traces with common mid-points lying within the Fresnel zone of a given CMP location. The radius of the Fresnel zone corresponding to the reservoir depth at the Coronation Field is about 70 m.

Assuming velocity anisotropy to have orthorhombic symmetry, I invert for the moveout parameters by fitting equation 6.1 to the interval traveltimes. The attenuation-anisotropy parameters are estimated by fitting the P-wave phase attenuation function in orthorhombic media (Zhu & Tsvankin, 2007) to the interval attenuation coefficients $\mathcal{A}_P$:

$$\mathcal{A}_P(\theta,\phi) = \mathcal{A}_{P0}\left[1 + \delta_Q(\phi)\sin^2\theta\cos^2\theta + \epsilon_Q(\phi)\sin^4\theta\right], \tag{6.5}$$

where $\mathcal{A}_{P0}$ is the attenuation coefficient along the vertical direction, θ and ϕ are the polar and azimuthal phase angles, respectively, and

$$\delta_Q(\phi) = \delta_Q^{(1)}\sin^2(\phi-\varphi_Q) + \delta_Q^{(2)}\cos^2(\phi-\varphi_Q), \tag{6.6}$$

$$\begin{aligned}\epsilon_Q(\phi) =& \epsilon_Q^{(1)}\sin^4(\phi-\varphi_Q) + \epsilon_Q^{(2)}\cos^4(\phi-\varphi_Q) \\ &+ (2\epsilon_Q^{(2)} + \epsilon_Q^{(3)})\sin^2(\phi-\varphi_Q)\cos^2(\phi-\varphi_Q).\end{aligned} \tag{6.7}$$

The angle φ_Q is the azimuth of the $[x_1, x_3]$ symmetry plane and the parameters $\delta_Q^{(1)}$, $\delta_Q^{(2)}$, $\epsilon_Q^{(1)}$, $\epsilon_Q^{(2)}$, and $\epsilon_Q^{(3)}$ govern the angular variation of the P-wave attenuation coefficient (Zhu & Tsvankin, 2007).

Although equation 6.5 describes the angular variation of the phase attenuation co-

efficient $\mathcal{A}$, it is valid for the group attenuation coefficient $\mathcal{A}_g$ estimated from seismic data because $\mathcal{A}_g = \mathcal{A}|_{\xi=0^\circ}$ (see Chapter 3). As mentioned in Chapter 5, inversion for the attenuation-anisotropy parameters requires knowledge of the anisotropic velocity field which can be used to compute the phase angle from the measured group angle. I use a well-log derived interval vertical P-wave velocity V_{P0} of 3200 m/s (Monk *et al.*, 2006) to estimate the velocity anisotropy parameters $\delta^{(1,2,3)}$ and $\epsilon^{(1,2)}$ from the moveout parameters. Using these velocity anisotropy parameters, I estimate the phase angles from the computed group angles. Note that it is possible to perform velocity analysis prior to attenuation processing using the interval traveltime because the influence of attenuation on velocity for a fixed frequency typically is of the second order (Zhu & Tsvankin, 2006; Behura & Tsvankin, 2009).

6.4.1 Error Analysis

To compute the variance of the estimated moveout parameters, I assume a 4 ms standard deviation (two times the sampling interval) of the semblance-derived traveltimes. Applying the method of error propagation to equation 6.1, I calculate the standard deviation of the parameters $V_{\rm nmo}^{(1,2)}$, $\eta^{(1,2,3)}$, φ, and φ_η.

Since the variance is available for every estimated value of $\mathcal{A}$, I use the method of weighted least squares (e.g., Bates & Watts, 2007) to estimate the attenuation-anisotropy parameters and their variances. By using the inverse of the variances as weights, variables with a smaller variance are given relatively larger weights. The method of error propagation is then used to calculate the variance-covariance matrix of the attenuation-anisotropy parameters.

6.5 Results

Here, I discuss the results of azimuthal velocity and attenuation analysis for an interval containing the reservoir at about 0.8 s (Figure 6.4). The interval NMO ellipse of the target layer is represented by its eccentricity (Figure 6.5a) and the azimuth of φ^{fast} (Figure 6.5b) for each common midpoint. The nmo eccentricity is defined as $|V_{\rm nmo}^{(1)} - V_{\rm nmo}^{(2)}|/V_{\rm nmo}^{fast}$ where $V_{\rm nmo}^{fast} = max\{|V_{\rm nmo}^{(1)}, V_{\rm nmo}^{(2)}\}$ and φ^{fast} is the azimuth of $V_{\rm nmo}^{fast}$. The lower half of the survey area shows strong azimuthal velocity anisotropy within the target layer, while in the upper half it is significantly weaker. The axes of the NMO ellipses have azimuths that show an

even distribution about 90°. If the field has only one dominant fracture set, it most likely has a strike parallel to the NS-direction. This would also imply that in the lower half of the survey area, the target layer is more intensely fractured than it is in the upper half. In the presence of more than one fracture set, however, interpretation becomes more complicated.

The vertical attenuation coefficient $\mathcal{A}_0$ is shown in Figure 6.6a and its standard deviation is in Figure 6.6b. Note that the standard deviation of $\mathcal{A}_0$ in most of the survey area is below 0.02 (Figure 6.6b) which is much smaller than the average value of $\mathcal{A}_0$ (0.07). Zones of higher attenuation (hot colors) in the lower half of the survey area show a reasonable correspondence with locations of existing gas-producing wells (Figure 6.7; Monk *et al.*, 2006). Therefore, $\mathcal{A}_0$ could possibly be used as a reliable measure of gas distribution. This would also mean that the area in the vicinity of $x = 7$ km, $y = 10$ km possibly has large gas accumulations. The coefficient $\mathcal{A}_0$ should be sensitive to gas present in pores and is not influenced by vertical fractures; it should, therefore, be used as an indicator of gas accumulation in porous sands. Note that $\mathcal{A}_0$ corresponds to the effective attenuation of the whole target layer and therefore is influenced also by lithologies other than gas sands.

The magnitude of the attenuation-anisotropy parameters $\delta_Q^{(1)}$ and $\delta_Q^{(2)}$ (Figure 6.8) can be extremely high with maximum absolute values approaching 30. Thus, the attenuation anisotropy is significantly higher than velocity anisotropy characterized by average δ values about 0.4. Similar observations of stronger anisotropy of attenuation than that of velocity have also been made by Hosten *et al.* (1987), Arts & Rasolofosaon (1992), and Zhu *et al.* (2007b). Zones of strong attenuation anisotropy in the NW portion of the survey area might also correspond to gas accumulations.

To obtain a measure of azimuthal attenuation anisotropy, I compute the difference $|\delta_Q^{(1)} - \delta_Q^{(2)}|$ (Figure 6.9a). Although the azimuthal variation of attenuation anisotropy is strong, it shows no large-scale spatially coherent patterns within the survey area. The azimuth of the symmetry plane φ_Q^{max} corresponding to δ_Q^{max} is shown in Figure 6.9b. The lack of a consistent pattern in φ_Q^{max} suggests that attenuation is azimuthally isotropic or the azimuthal variation is below the noise level.

6.6 Conclusions

P-wave interval attenuation analysis provides valuable information for reservoir characterization at the Coronation Field. The interval anisotropic velocity and attenuation fields within a subsurface zone containing the reservoir sands are estimated using the layer-

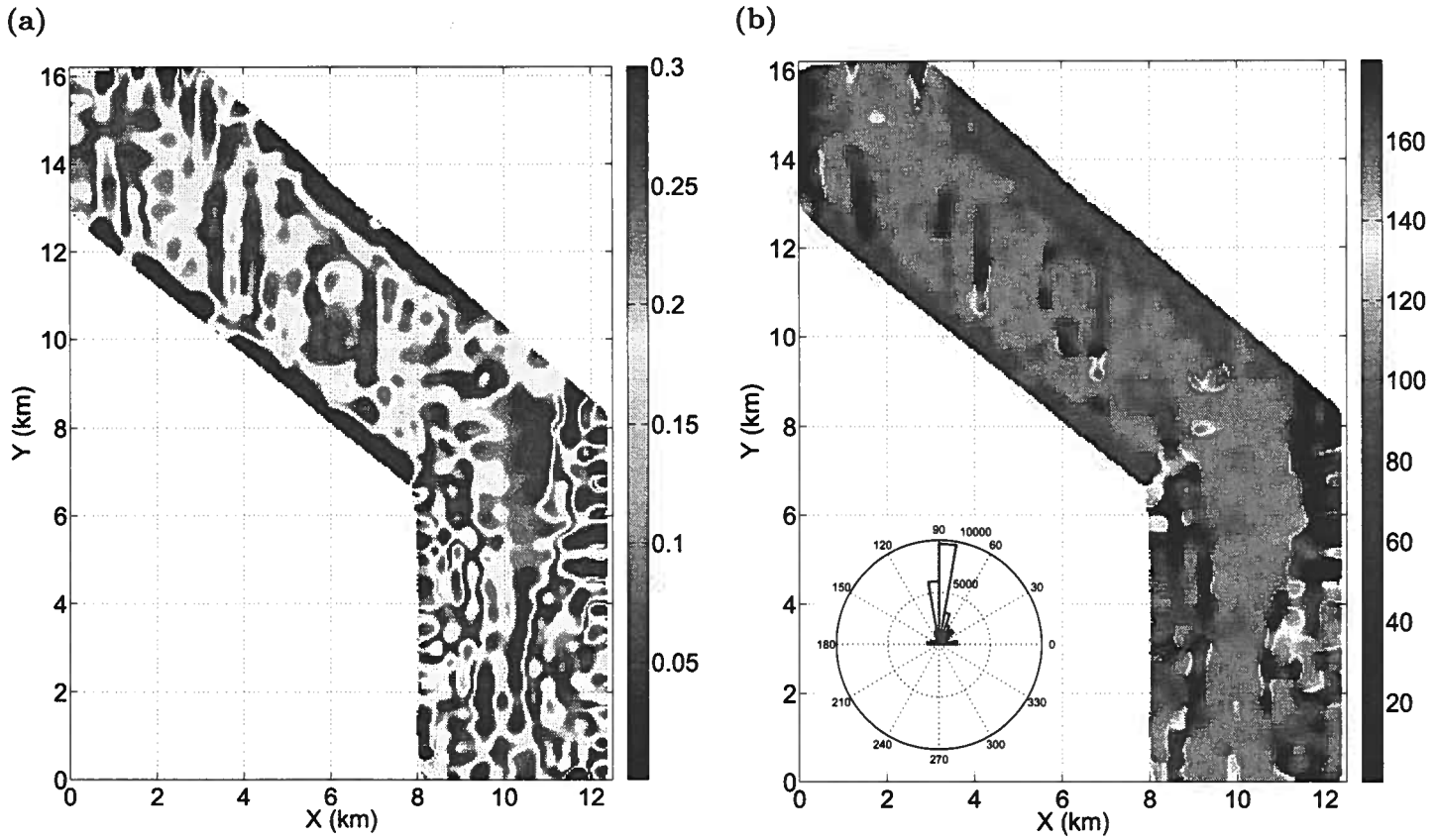

Figure 6.5: Eccentricity (a) and azimuth φ^{fast} (b) of the interval NMO ellipses of the target layer. The inset in (b) is the rose diagram of the azimuths. The NMO eccentricity is calculated by subtracting unity from the ratio of the semi-major axis and the semi-minor axis. The azimuths in (b) are computed with respect to the x-axis.

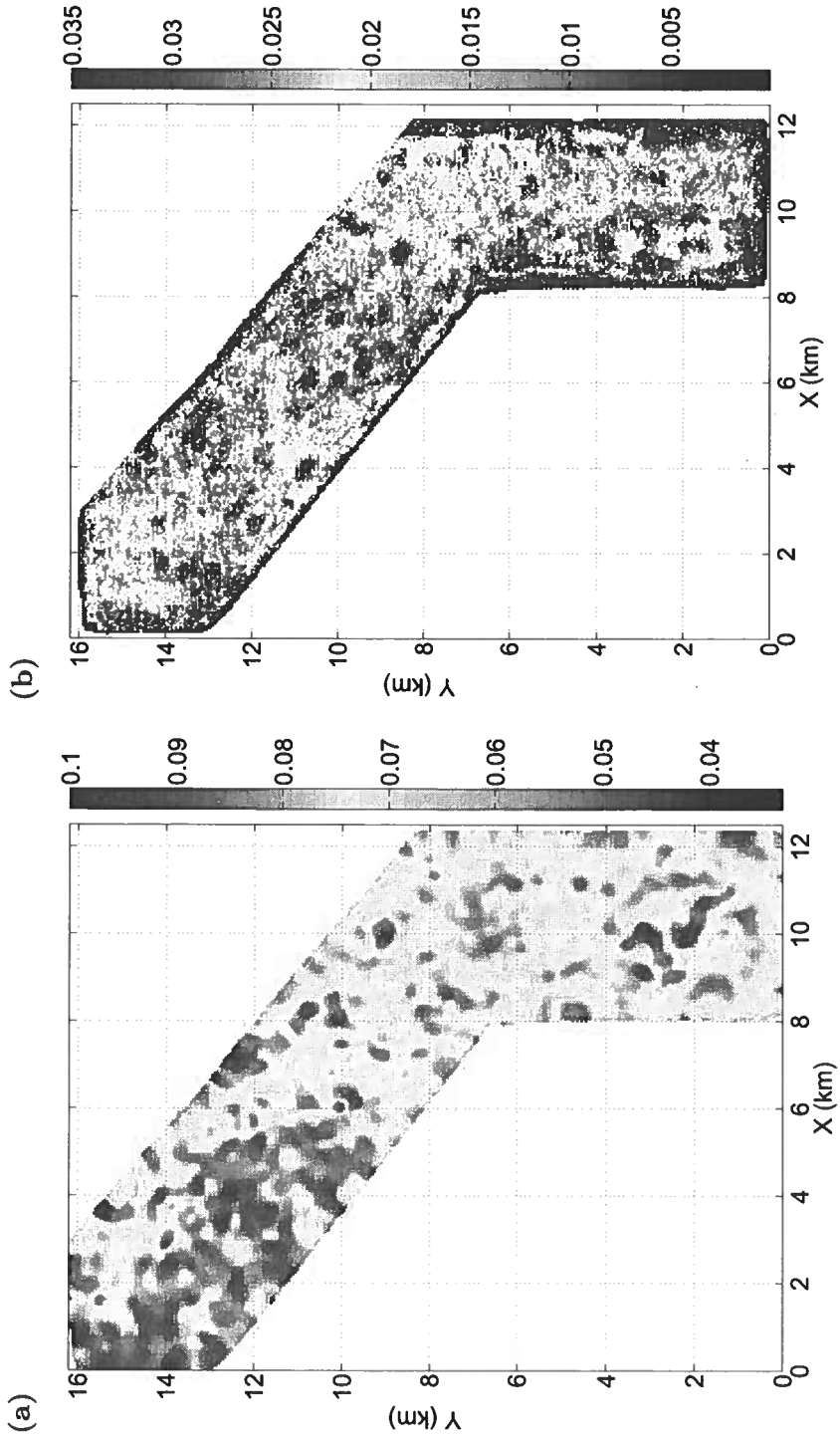

Figure 6.6: Interval vertical attenuation coefficient $\mathcal{A}_0$ (a) its standard deviation (b) for the target layer.

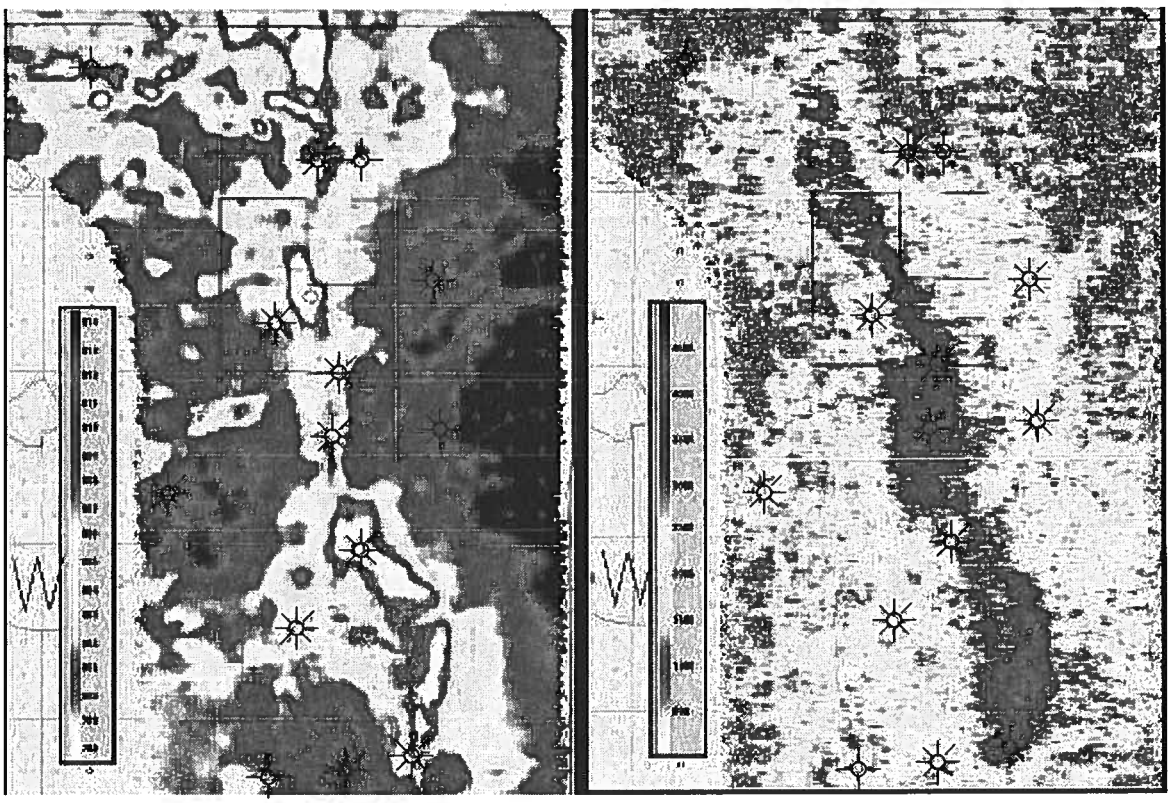

Figure 6.7: Location of gas-producing (circles with eight lines) and dry wells (circles with four lines) in the Coronation Field (modified from Monk *et al.*, 2006). The area shown is centered about $x = 9.5$ km, $y = 5.5$ km.

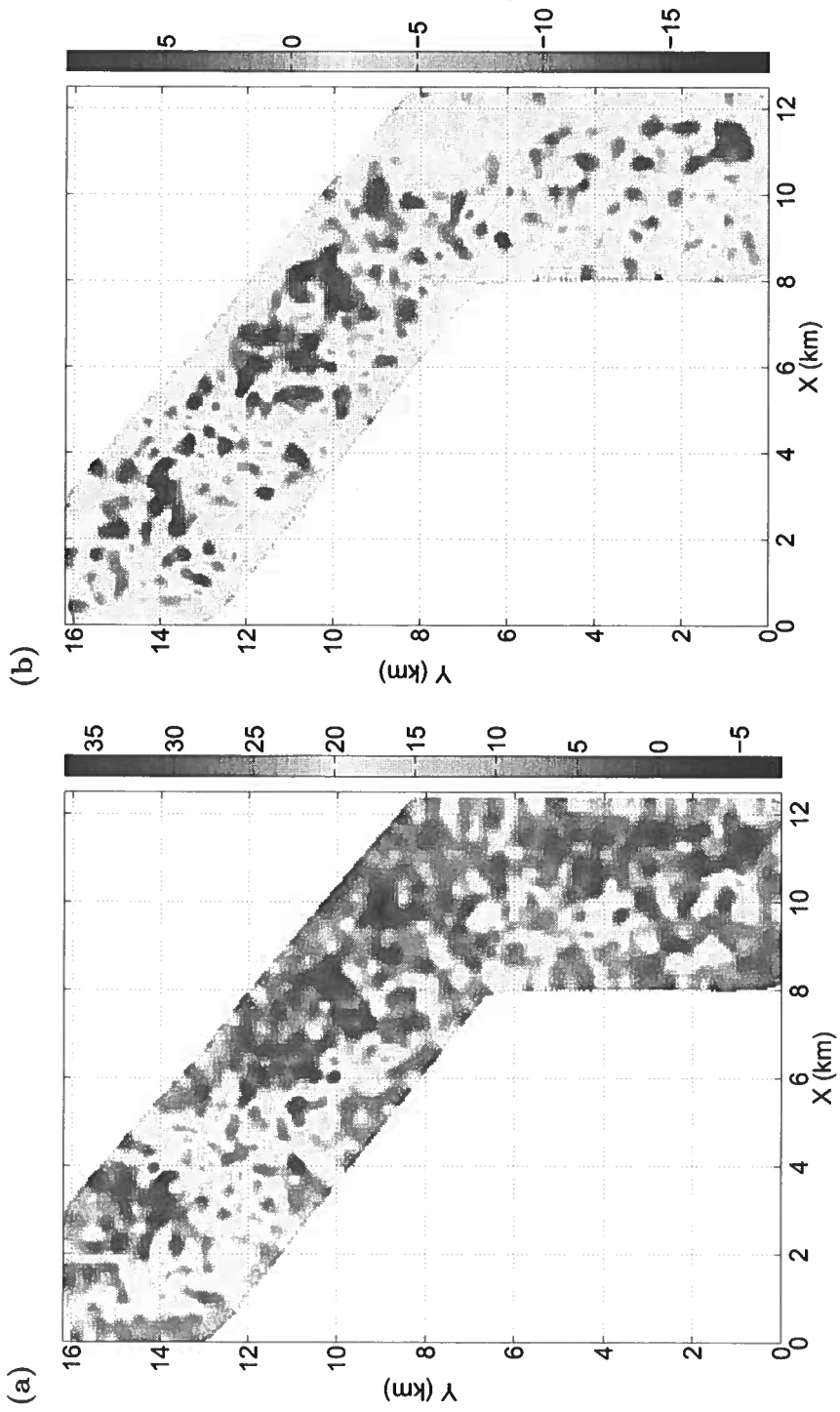

Figure 6.8: Larger (a) and smaller (b) of the two attenuation-anisotropy parameters $\delta_Q^{(1)}$ and $\delta_Q^{(2)}$ of the target layer.

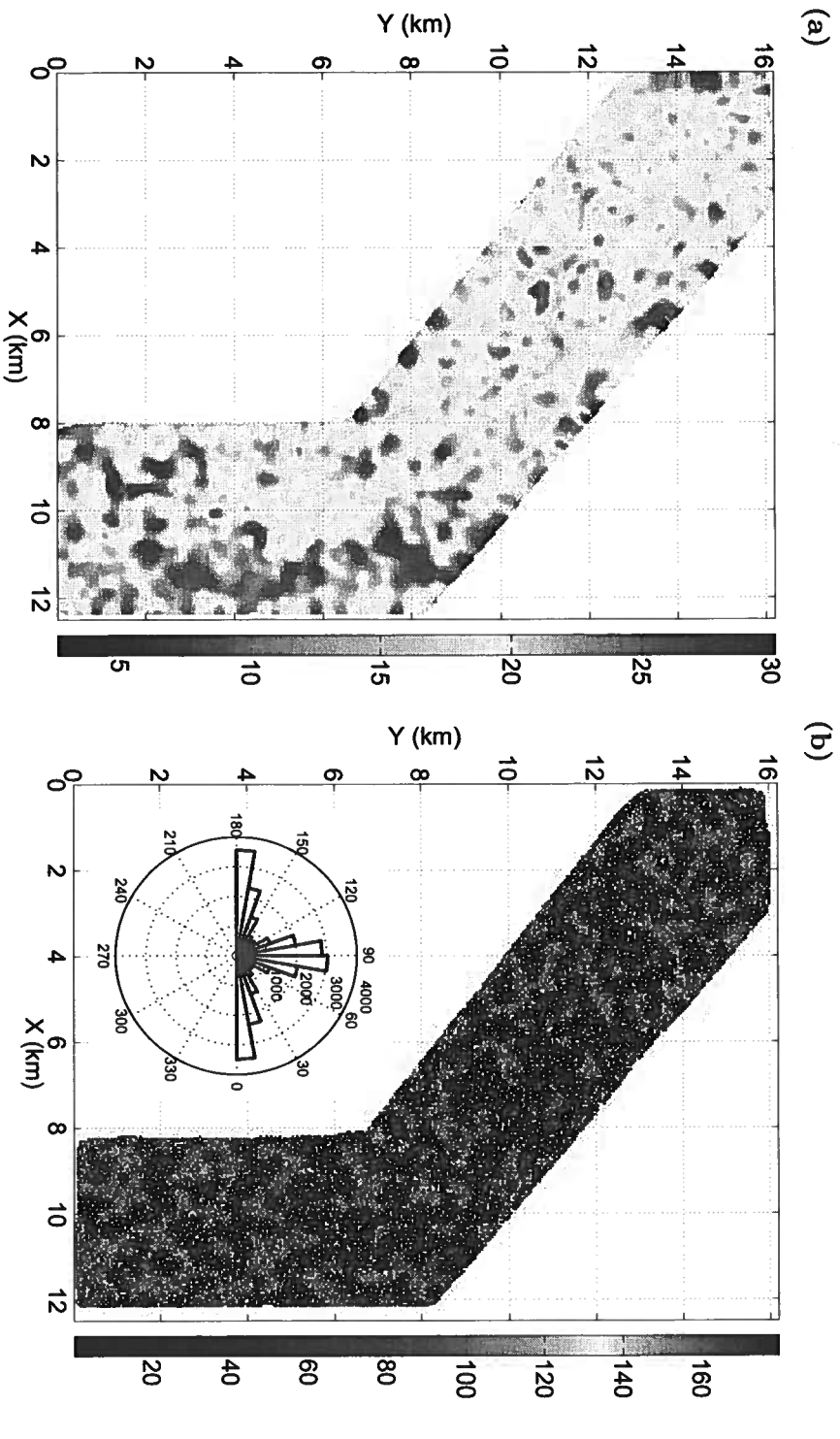

Figure 6.9: Difference $|\delta_Q^{(1)} - \delta_Q^{(2)}|$ (a) and the azimuth φ_Q^{max} (b). The inset in (b) is the rose diagram of the angles φ_Q^{max}.

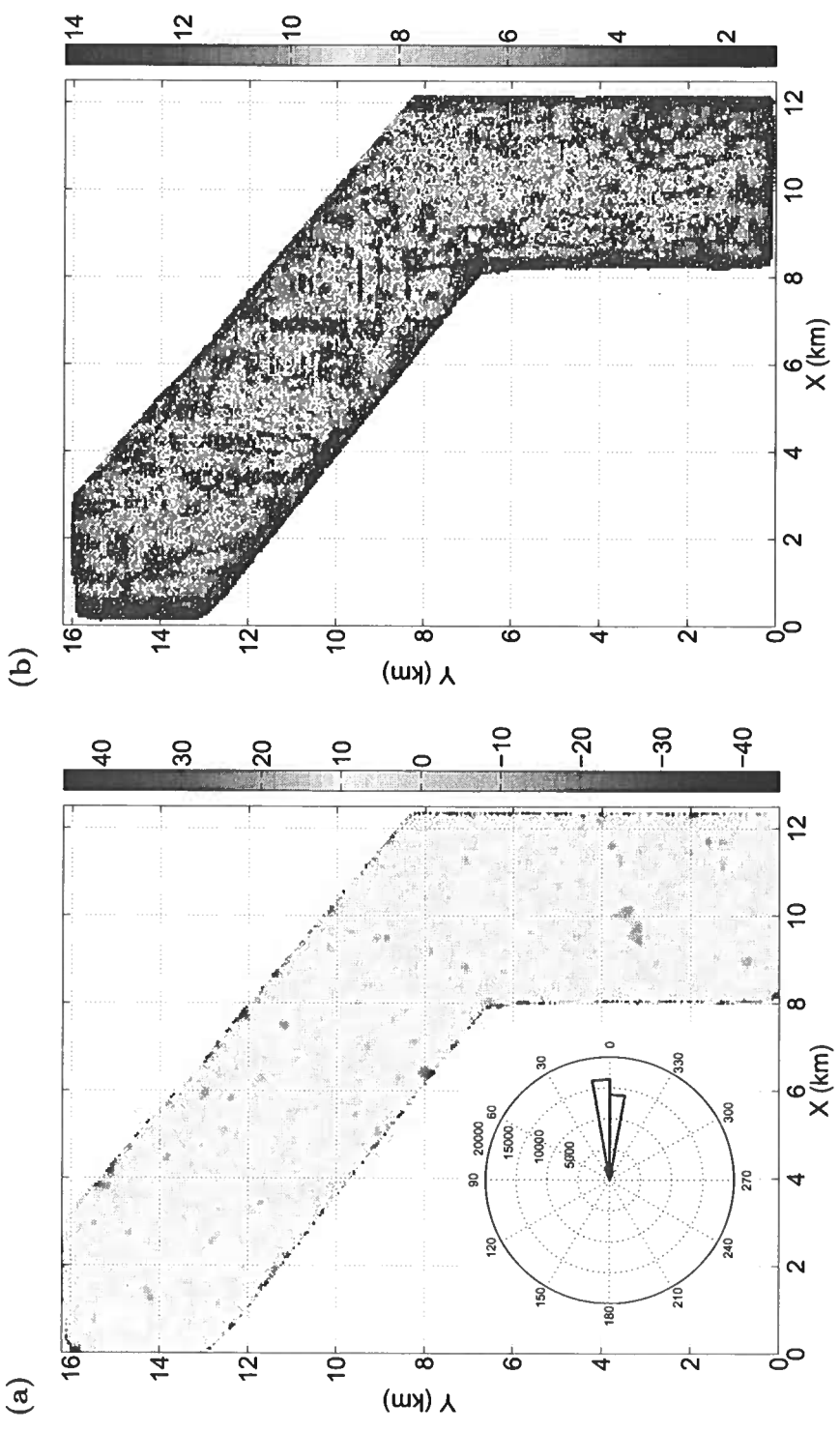

Figure 6.10: Difference between the azimuths $\varphi_Q^{max} - \varphi^{fast}$ (a) and its standard deviation (b). The inset in (a) is the rose diagram of the angles $\varphi_Q^{max} - \varphi^{fast}$.

stripping approach introduced in Chapter 5. Nonhyperbolic semblance analysis yields the wide-azimuth traveltimes of the reflectors bounding the target interval, while the windowed events along the moveout curves are used for computing the interval anisotropic attenuation.

The lower half of the survey area shows strong azimuthal velocity anisotropy with the azimuth of V_{nmo}^{fast} consistently oriented close to the NS-direction. Areas of high interval vertical attenuation coefficient $\mathcal{A}_0$ correlate with location of existing gas-producing wells, which makes $\mathcal{A}_0$ a reliable indicator of gas sands. The interval attenuation anisotropy is anomalously strong and much higher than velocity anisotropy. This is a work in progress and requires additional analysis, especially with respect to fracture characterization. Additional (e.g., production) data, however, are necessary to verify the above analysis and understand its limitations for reservoir characterization.

Chapter 7

Conclusions and recommendations

7.1 Conclusions

Knowledge of attenuation and attenuation anisotropy can be highly beneficial in lithology discrimination, fracture and fluid characterization, and in evaluating the physical properties of rocks. In this thesis I addressed different aspects of attenuation analysis ranging from rock-physics studies of attenuative rocks such as oil-shales, to describing wave propagation in attenuative anisotropic media to extracting interval attenuation parameters from reflection seismic data.

To understand the changes occurring in oil shales during a thermal recovery process, I studied their seismic properties in the laboratory for a wide range of temperatures. The physical state of the kerogen in the shales is extremely sensitive to heat, which makes estimation of shear-wave properties of oil shales particularly attractive. Moreover, as oil shales are strongly viscoelastic, I conducted experiments within the seismic frequency band (0.01 to 80 Hz) where the shale properties are significantly different from those in the well-log and ultrasonic bands.

The laboratory measurements show weak velocity dispersion and a negligible variation in Q with frequency, which corroborates the commonly used assumption of constant Q within the seismic bandwidth. On the other hand, these shales are extremely sensitive to changes in temperature. The melting of kerogen can reduce the shear-wave velocity significantly (by a factor as five). The quality factor can also drop by a factor of 10 when temperature is increased from room conditions to about 150°C. Therefore, reservoir rocks affected by heat should show a noticeable decrease in shear-wave velocities accompanied by significant increase in attenuation. Velocity and attenuation anisotropy of these rocks are also highly sensitive to heating. In my measurements, the SH-wave velocity anisotropy parameter γ increased from 0.2 at room temperature to 2.5 at 200°C. Similarly, the maxi-

mum change in attenuation-anisotropy parameter γ_Q was 0.8 for the temperature range of investigation; even the sign of γ_Q changed with heating. The whole suite of measurements is directly applicable to seismic analysis of oil-shale reservoirs during their exploration, development, and production. The high sensitivity of shear waves to temperature changes in these reservoirs makes 4D multicomponent seismic analysis promising.

To analyze the influence of the inhomogeneity angle ξ (the angle between the real and imaginary parts of the wave vector) on velocity and attenuation in arbitrarily anisotropic media, I used the first-order perturbation theory. The perturbation analysis yields concise analytic expressions for the complex wave vector $\mathbf{k}$, the phase attenuation coefficient $\mathcal{A}|_{\xi=0^\circ}$, and the group attenuation coefficient $\mathcal{A}_g$ in terms of the perturbations of the complex stiffness coefficients. For a wide range of small and moderate angles ξ, the group attenuation coefficient $\mathcal{A}_g$ practically coincides with the phase attenuation coefficient $\mathcal{A}|_{\xi=0^\circ} = 1/2Q$, which is proportional to the angle-dependent inverse quality factor. This conclusion remains valid even for uncommonly high attenuation ($Q \approx 10$) and strong velocity and attenuation anisotropy. The negligible difference between $\mathcal{A}_g$ and $\mathcal{A}|_{\xi=0^\circ}$ suggests that seismic data can be inverted for the attenuation-anisotropy parameters without knowledge of the inhomogeneity angle.

To gain physical insight into reflected/transmission at boundaries between attenuative anisotropic media, I developed linearized expressions for plane-wave reflection/transmission coefficients in terms of the velocity- and attenuation-anisotropy parameters, as well as the velocity and attenuation contrasts across the interface. For an incident P-wave with a zero inhomogeneity angle, the form of the linearized PP- and PS-wave reflection coefficients in arbitrarily anisotropic media is the same as in purely elastic models, but all terms become complex.

Both analytic and numerical results show that only in the presence of strong attenuation ($Q < 10$) does the contribution of the imaginary part of the stiffness tensor (which is responsible for attenuation) become comparable to that of the real part. In particular, the influence of the attenuation-anisotropy parameters ϵ_Q and δ_Q on the PP-wave reflection coefficient for VTI media typically is much weaker than that of the velocity-anisotropy parameters ϵ and δ. The largest attenuation-related terms in the reflection coefficients for both PP- and PS-waves are proportional to the contrasts in the normalized symmetry-direction attenuation coefficients of P- and S-waves because the contrasts in the attenuation-anisotropy parameters are scaled by the inverse quality factor $1/Q_{P0}$.

If the incident wave has a nonzero inhomogeneity angle ξ, the form of the linearized reflection coefficients is different from the conventional AVO expression. In particular, the PP-wave reflection coefficient is no longer an even function of the incidence angle θ and includes a term proportional to $\sin\theta$. Likewise, when $\xi \neq 0°$, the normal-incidence PS-wave reflection coefficient (i.e., the AVO intercept) does not vanish and may even attain values comparable to the AVO intercept for the PP reflection. However, the inhomogeneity angle makes a substantial contribution to the AVO response only for strongly attenuative media with $Q < 10$.

Since most existing attenuation estimates from reflection data are obtained for the whole section above the reflecting interface, I introduced a method to estimate interval offset- and azimuth-dependent attenuation from reflection data. This technique is based on combining a velocity-independent layer-stripping approach with a modified version of the spectral-ratio method. While there are no restrictions on heterogeneity and anisotropy of the target layer, the overburden has to be composed of laterally homogeneous layers with a horizontal symmetry plane (e.g., layers may be orthorhombic). It should be emphasized that this attenuation layer stripping is data-driven and does not require knowledge of the overburden velocity and attenuation parameters. In general, the algorithm estimates the average interval group attenuation coefficient along the raypath of a reflected wave. However, for homogeneous horizontal target layers it is possible to reconstruct the normalized phase attenuation coefficient $\mathcal{A}$ for each source-receiver pair. The coefficient $\mathcal{A}$ represents a measure of intrinsic attenuation and can be inverted for the interval attenuation-anisotropy parameters. Numerical examples for horizontally layered VTI and orthorhombic media confirm that the method yields accurate interval phase attenuation coefficients even for models with uncommonly strong attenuation and substantial velocity and attenuation anisotropy.

The attenuation coefficient in a reservoir can help to predict the presence and distribution of hydrocarbons (e.g., to distinguish between steam and heat fronts in heavy-oil reservoirs). The 3D version of the method can be used to estimate the azimuthally varying interval attenuation coefficient, which represents a sensitive attribute for fracture characterization and reconstruction of the stress field.

I applied the layer-stripping method to wide-azimuth P-wave data acquired over a gas reservoir in the Coronation Field, Alberta. The lower half of the survey area shows strong azimuthal velocity anisotropy with the vertical symmetry planes aligned consistently along the NS- and EW-directions. The vertical attenuation coefficient shows a reasonable corre-

spondence with existing gas-producing well locations. The interval attenuation anisotropy is anomalously strong and much higher than velocity anisotropy.

7.2 Recommendations

The rock-physics study in this thesis was limited to shear-wave properties of oil shales. The majority of the existing seismic data, however, is P-waves, which generally have a higher quality than S-waves and can be processed in a more robust way. P-wave anisotropy of oil shales needs more attention because of the large sensitivity of shales to temperature changes. Moreover, the in-situ pressure during thermal stimulation of oil shales should be substantially different from the atmospheric pressure. Such pressure differences are expected to have a significant influence on the shale properties, in particular their velocity and attenuation anisotropy. It is, therefore, important to study the P-wave properties for oil shales under variable pressure with particular emphasis on velocity and attenuation anisotropy.

The algorithm for estimating interval anisotropic attenuation from seismic data is limited to a laterally homogeneous overburden with a horizontal symmetry plane. Although the target layer can be arbitrarily anisotropic and heterogeneous, the assumption on the overburden limits its applicability to simple layer-cake sections such as most tight-gas plays. In order to tackle more complicated subsurface structures, we need an algorithm that can handle strong lateral heterogeneity and, possibly, arbitrary anisotropy. A potentially promising option would be waveform inversion, which has been applied mostly to isotropic media to estimate density, velocities, and in some cases, attenuation. The layer-stripping derived attenuation coefficients could be used as the initial guess in the waveform inversion algorithm.

P-wave attenuation in combination with S-wave attenuation coefficient can be extremely valuable in locating gas-sands and condensate accumulations and distinguishing them from water- and oil-saturated zones. This is because $Q_P < Q_S$ in gas reservoirs, while in oil zones, $Q_P > Q_S$. Therefore, it would be useful to extend the layer-stripping method to estimating the S-wave attenuation coefficient from mode-converted data. Shear-wave attenuation could also be extracted from pure shear data without any modification to the algorithm. Since traveltime picking plays a crucial role in estimating interval attenuation using the layer-stripping method, a more accurate method of tracing reflections (e.g., automatic picking using cross-correlations) could be implemented.

The high sensitivity of attenuation to the presence of hydrocarbons makes time-lapse

attenuation analysis extremely valuable. Laboratory measurements clearly indicate that P- and S-wave attenuations are extremely sensitive to water saturation while velocities are not. Therefore, attenuation analysis can complement traditional velocity analysis and add to the understanding of the reservoir. The influence of fluid-filled cracks on attenuation anisotropy might be different from their influence on velocity anisotropy. For example, dry cracks would result in velocity anisotropy but have no influence on attenuation. 4D monitoring could benefit immensely from attenuation analysis. For instance, CO_2 sequestration would have a significant attenuation imprint on seismic data. Oil production through primary or secondary recovery processes could potentially benefit from attenuation analysis.

Another problem of significant interest is the influence of scattering vis-à-vis intrinsic attenuation and their separation. Many field experiments suggest that intrinsic attenuation usually dominates scattering effects. Techniques for separating scattering effects from intrinsic attenuation, however, are not yet developed and should be of primary focus.

The ultimate goal of attenuation analysis is to evaluate rock properties that can be used for fluid, lithology, and fracture characterization. Although there have been numerous laboratory studies and theoretical advances in understanding wave propagation in attenuative anisotropic media, physical mechanisms responsible for attenuation anisotropy are not yet fully understood. New experiments and models have to be explored to better explain the complex phenomenon of attenuation anisotropy.

With increasing demand for hydrocarbons comes strong demand for novel technologies, such as attenuation analysis, to enhance our knowledge of reservoir properties. Attenuation ought to be viewed as a stepping stone, and not as a stumbling block impending seismic processing. Despite the many remaining challenges in attenuation analysis, I am optimistic that we will be able to use attenuation and attenuation anisotropy for reservoir characterization in the near future.

References

Akbar, N., Dvorkin, J., & Nur, A. 1993. Relating P-wave attenuation to permeability. *Geophysics*, **58**, 20–29.

Aki, K., & Richards, P.G. 2002. *Quantitative Seismology.* Second edn. Sausalito: Univ. Science Books.

Alkhalifah, T., & Tsvankin, I. 1995. Velocity analysis for transversely isotropic media. *Geophysics*, **60**, 1550–1566.

Amundsen, L., & Mittet, R. 1994. Estimation of phase velocities and Q-factors from zero-offset, vertical seismic profile data. *Geophysics*, **59**, 500–517.

Arts, R. J., & Rasolofosaon, P. N. J. 1992. Approximation of velocity and attenuation in general anisotropic rocks. *Pages 640–643 of: Expanded Abstracts.* Society of Exploration Geophysicists.

Ayzenberg, M., Tsvankin, I., Aizenberg, A., & Ursin, B. 2008. Effective Reflection Coefficients for Curved Interfaces in TI Media. *70th EAGE Conference & Exhibition.*

Backus, G. E. 1962. Long wave elastic anisotropy produced by horizontal layering. *J. Geophys. Res.*, **67**, 4427–4440.

Bakulin, A. 2003. Intrinsic and layer-induced vertical transverse isotropy. *Geophysics*, **68**, 1708–1713.

Banik, N. C. 1987. An effective anisotropy parameter in transversely isotropic media. *Geophysics*, **52**, 1654–1664.

Bates, D. M., & Watts, D. G. 2007. *Nonlinear Regression Analysis and Its Applications.* Wiley-Interscience.

Batzle, M. L., Han, De-H., & Hofmann, R. 2006. Fluid mobility and frequency-dependent seismic velocity — Direct measurements. *Geophysics*, **71**(1), N1–N9.

Behura, J., & Tsvankin, I. 2006. Small-angle AVO response of PS-waves in tilted transversely isotropic media. *Geophysics*, **71**(5), C69–C79.

Behura, J., & Tsvankin, I. 2008. Estimation of interval anisotropic attenuation from reflection data. *SEG Technical Program Expanded Abstracts.*

Behura, J., & Tsvankin, I. 2009. Role of the inhomogeneity angle in anisotropic attenuation analysis. *Geophysics, in print.*

Behura, J., Batzle, M., & Hofmann, R. 2006. Shear properties of oil shales. *Pages 1973–1977 of: Expanded Abstracts.* Society of Exploration Geophysicists.

Behura, J., Batzle, M., Hofmann, R., & Dorgan, J. 2007. Heavy oils: Their shear story. *Geophysics*, **72**(5), E175–E183.

Best, A. I. 1994. Seismic attenuation anisotropy in reservoir sedimentary rocks. *SEG Technical Program Expanded Abstracts*, **13**, 822–825.

Bortfeld, D. 1961. Approximations to the reflection and transmission coefficients of plane longitudinal and transverse waves. *Geophysical Prospecting*, **9**, 485–502.

Boulanger, P., & Hayes, M. A. 1993. *Bivectors and Waves in Mechanics and Optics.* 1 edn. Chapman & Hall/CRC.

Brajanovski, M., Gurevich, B., & Schoenberg, M. 2005. A model for P-wave attenuation and dispersion in a porous medium permeated by aligned fractures. *Geophysical Journal International*, **163**, 372–384.

Braun, S., Ewins, D., & Rao, S. S. 2001. *Encyclopedia of Vibration.* Academic Press Inc.

Buckingham, M. J. 2000. Wave propagation, stress relaxation, and grain-to-grain shearing in saturated, unconsolidated marine sediments. *The Journal of the Acoustical Society of America*, **108**, 2796–2815.

Carcione, J. M. 1992. Anisotropic Q and velocity dispersion of finely layered media. *Geophysical Prospecting*, **40**, 761–783.

Carcione, J. M. 2000. A model for seismic velocity and attenuation in petroleum source rocks. *Geophysics*, **65**, 1080–1092.

Carcione, J. M. 2007. *Wave Fields in Real Media: Wave Propagation in Anisotropic, Anelastic, Porous and Electromagnetic Media.* 2nd edn. Elsevier Science.

Carcione, J. M., & Cavallini, F. 1995. Forbidden directions for inhomogeneous pure shear waves in dissipative anisotropic media. *Geophysics*, **60**, 522–530.

Červený, V., & Pšenčík, I. 2005a. Plane waves in viscoelastic anisotropic media-I. Theory. *Geophysical Journal International*, **161**, 197–212.

Červený, V., & Pšenčík, I. 2005b. Plane waves in viscoelastic anisotropic media-II. Numerical examples. *Geophysical Journal International*, **161**, 213–229.

Červený, V., & Pšenčík, I. 2006. Energy flux in viscoelastic anisotropic media. *Geophysical Journal International*, **166**(Sept.), 1299–1317.

Červený, V., & Pšenčík, I. 2008a. Quality factor Q in dissipative anisotropic media. *Geophysics*, **73**(4), T63–T75.

Červený, V., & Pšenčík, I. 2008b. Weakly inhomogeneous plane waves in anisotropic, weakly dissipative media. *Geophysical Journal International*, **172**, 663–673.

Chapman, M. 2003. Frequency dependent anisotropy due to meso-scale fractures in the presence of equant porosity. *Geophysical Prospecting*, **51**, 369–379.

Chow, T. L. 1995. *Classical Mechanics.* Wiley.

Crampin, S., & Peacock, S. 2005. A review of shear-wave splitting in the compliant crack-critical anisotropic earth. *Wave Motion*, **41**, 59–77.

Crandall, S. H., Dahl, N. C., & Lardner, T. J. 1999. *An Introduction to the Mechanics of Solids.* Second edn. McGraw-Hill.

Dasgupta, R., & Clark, R. A. 1998. Estimation of Q from surface seismic reflection data. *Geophysics*, **63**, 2120–2128.

Declercq, N. F., Briers, R., Degrieck, J., & Leroy, O. 2005. The history and properties of ultrasonic inhomogeneous waves. *IEEE Transactions on Ultrasonics, Ferroelectrics and Frequency Control*, **52**(5), 776–791.

Deschamps, M., & Assouline, F. 2000. Attenuation Along the Poynting Vector Direction of Inhomogeneous Plane Waves in Absorbing and Anisotropic Solids. *Acta Acustica united with Acustica*, **86**, 295–302.

Dewangan, P., & Tsvankin, I. 2006. Velocity-independent layer stripping of PP and PS reflection traveltimes. *Geophysics*, **71**(4), U59–U65.

Dilay, A., & Eastwood, J. 1995. Spectral analysis applied to seismic monitoring of thermal recovery. *The Leading Edge*, **14**, 1117–1122.

Eastwood, J., Lebel, P., Dilay, A., & Blakeslee, S. 1994. Seismic monitoring of steam-based recovery of bitumen. *The Leading Edge*, **13**, 242–251.

Edgeworth, R., Dalton, B.J., & Parnell, T. 1984. The pitch drop experiment. *European Journal of Physics*, **5**, 198–200.

Gajewski, D., & Pšenčík, I. 1992. Vector wavefields for weakly attenuating anisotropic media by the ray method. *Geophysics*, **57**, 27–38.

Ganley, D. C., & Kanasewich, E. R. 1980. Measurement of absorption and dispersion from check shot surveys. *Journal of Geophysical Research*, **85**(Oct.), 5219–5226.

Gautam, K., Batzle, M. L., & Hofmann, R. 2003. Effects of fluids on attenuation of elastic waves. *SEG Technical Program Expanded Abstracts*, **22**, 1592–1595.

Gray, D. E. 1972. *American Institute of Physics Handbook.* Third edn. Mcgraw-Hill.

Grechka, V., & Tsvankin, I. 1998. 3-D description of normal moveout in anisotropic inhomogeneous media. *Geophysics*, **63**, 1079–1092.

Hauge, P. S. 1981. Measurements of attenuation from vertical seismic profiles. *Geophysics*, **46**, 1548–1558.

Hayes, B.J.R., Christopher, J.E., Rosenthal, L., Los, G., McKercher, B., Minken, D., Tremblay, Y.M., & Fennell, J. 2008. Cretaceous Mannville Group of the Western Canada Sedimentary Basin. *Atlas of the Western Canada Sedimentary Basin.*

Hearn, D. J., & Krebes, E. S. 1990. On computing ray-synthetic seismograms for anelastic media using complex rays. *Geophysics*, **55**(Apr.), 422–432.

Hedlin, K., Mewhort, L., & Margrave, G. 2001. Delineation of steam flood using seismic attenuation. *SEG Technical Program Expanded Abstracts*, **20**, 1572–1575.

Helbig, K. 1994. *Foundations of anisotropy for exploration seismics.* Amsterdam: Pergamon Press.

Hiramatsu, Y., & Ando, M. 1995. Attenuation Anisotropy Beneath the Subduction Zones in Japan. *Geophysical Research Letters*, **22**, 1653–1656.

Hosten, B., Deschamps, M., & Tittmann, B. R. 1987. Inhomogeneous wave generation and propagation in lossy anisotropic solids - Application to the characterization of viscoelastic composite materials. *Journal of the Acoustical Society of America*, **82**(Nov.), 1763–1770.

Huang, W., Briers, R., Rokhlin, S. I., & Leroy, O. 1994. Experimental study of inhomogeneous wave reflection from a solid–air periodically rough boundary using leaky Rayleigh waves. *The Journal of the Acoustical Society of America*, **96**, 363–369.

Iwasaki, T., Tatsuoka, F., & Takagi, Y. 1978. Shear moduli of sand under cyclic torsional shear loading. *Soils and Foundations*, **18**, 39–56.

Jackson, I., & Paterson, M. S. 1987. Shear modulus and internal friction of calcite rocks at seismic frequencies: pressure, frequency, and grainsize dependence. *Physics of Earth and Planetary Interiors*, **45**, 349–367.

Jackson, P. C. 1984. Paleogeography of the Lower Cretaceous Mannville Group of Western Canada. *Pages 49–77 of:* Masters, J. A. (ed), *M38: Elmworth: Case Study of a Deep Basin Gas Field.* American Association of Petroleum Geologists.

Jech, J., & Pšenčík, I. 1989. First-order perturbation method for anisotropic media. *Geophysical Journal International*, **99**(nov), 369–376.

Jílek, P. 2002a. Converted PS-wave reflection coefficients in weakly anisotropic media. *Pure and Applied Geophysics*, **159**, 1527–1562.

Jílek, P. 2002b. *Modeling and inversion of converted-wave reflection coefficients in anisotropic media: A tool for quantitative AVO analysis.* Ph.D. thesis, Colorado School of Mines.

Johnson, D. L. 2001. Theory of frequency dependent acoustics in patchy-saturated porous media. *Journal of the Acoustical Society of America*, **110**, 682–694.

Johnston, D. H. 1987. Physical properties of shale at temperature and pressure. *Geophysics*, **52**, 1391–1401.

Johnston, D. H., & Toksöz, M. N. 1981. *Seismic wave attenuation.* Geophysics reprint series, Society of Exploration Geophysicists.

Johnston, D. H., Toksöz, M. N., & Timur, A. 1979. Attenuation of seismic waves in dry and saturated rocks: II. Mechanisms. *Geophysics*, **44**, 691–711.

Johnston, J. E., & Christensen, N. I. 1996. Seismic anisotropy of shales. *International Journal of Rock Mechanics and Mining Sciences and Geomechanics Abstracts*, **33**, 72A–72A(1).

Klimentos, T. 1995. Attenuation of P- and S-waves as a method of distinguishing gas and condensate from oil and water. *Geophysics*, **60**, 447–458.

Krebes, E. S. 1983. The viscoelastic reflection/transmission problem: Two special cases. *Bulletin of Seismological Society of America*, **73**(Dec.), 1673–1683.

Krebes, E. S., & Le, L. H. T. 1994. Inhomogeneous plane waves and cylindrical waves in anisotropic anelastic media. *Journal of Geophysical Research*, **99**, 899–919.

Lakes, R. S. 1998. *Viscoelastic solids.* CRC Press.

Liu, E., Crampin, S., Queen, J. H., & Rizer, W. D. 1993. Velocity and attenuation anisotropy caused by microcracks and microfractures in a multiazimuth reverse VSP. *Canadian Journal of Exploration Geophysics*, **29**, 177–188.

Liu, E., Chapman, M., Varela, I., Li, X., Queen, J. H., & Lynn, H. 2007. Velocity and attenuation anisotropy: Implication of seismic fracture characterizations. *The Leading Edge*, **26**, 1170–1174.

Lockner, D. A., Walsh, J. B., & Byerlee, J. D. 1977. Changes in seismic velocity and attenuation during deformation of granite. *Journal of Geophysical Research*, **82**, 5374–5378.

Luh, P. C. 1988. Wavelet dispersion and bright spot detection. *SEG Technical Program Expanded Abstracts*, **7**, 1217–1220.

Lynn, H. B., Campagna, D., Simon, K. M., & Beckham, W. E. 1999. Relationship of P-wave seismic attributes, azimuthal anisotropy, and commercial gas pay in 3-D P-wave multiazimuth data, Rulison Field, Piceance Basin, Colorado. *Geophysics*, **64**, 1293–1311.

MacBeth, C. 1999. Azimuthal variation in P-wave signatures due to fluid flow. *Geophysics*, **64**, 1181–1192.

Macrides, C. G., Kanasewich, E. R., & Bharatha, S. 1988. Multiborehole seismic imaging in steam injection heavy oil recovery projects. *Geophysics*, **53**, 65–75.

Mah, M. 2005. *Determination of elastic constants of orthorhombic and transversely isotropic materials: Experimental application to a kerogen rich rock.* Ph.D. thesis, University of Alberta.

Masters, J. A. 1984. Lower Cretaceous Oil and Gas in Western Canada. *Pages 1–33 of:* Masters, J. A. (ed), *M38: Elmworth: Case Study of a Deep Basin Gas Field.* American Association of Petroleum Geologists.

Maultzsch, S., Chapman, M., Liu, E., & Li, X. Y. 2003. Modelling frequency-dependent seismic anisotropy in fluid-saturated rock with aligned fractures: implication of fracture size estimation from anisotropic measurements. *Geophysical Prospecting*, **51**, 381–392.

Maultzsch, S., Chapman, M., Liu, E., & Li, X. 2007. Modelling and analysis of attenuation anisotropy in multi-azimuth VSP data from the Clair field. *Geophysical Prospecting*, **55**, 627–642.

Mavko, G. M., & Dvorkin, J. 2005. P-wave attenuation in reservoir and non-reservoir rock. *67th EAGE Conference & Exhibition.*

Mavko, G. M., & Nur, A. 1979. Wave attenuation in partially saturated rocks. *Geophysics*, **44**, 161–178.

Molotkov, L. A., & Bakulin, A. 1998. Attenuation in the effective model of finely layered porous Biot media. *Page P156 of: Expanded Abstracts.* European Association of Geoscientists and Engineers.

Monk, D., Larson, R., & Anderson, P. 2006. An East-Central Alberta multi-component seismic case history. *CSEG Recorder*, May, 18–22.

Moyal, J. E., & Fletcher, W. P. 1945. Free and forced vibration methods in the measurement of the dynamic properties of rubbers. *Journal of Scientific Instruments*, **22**, 167–170.

Murphy, W. F., Winkler, K. W., & Kleinberg, R. L. 1986. Acoustic relaxation in sedimentary rocks: Dependence on grain contacts and fluid saturation. *Geophysics*, **51**, 757–766.

Nechtschein, S., & Hron, F. 1997. Effects of anelasticity on reflection and transmission coefficients. *Geophysical Prospecting*, **45**, 775–793.

Neep, J. P., Sams, M. S., Worthington, M. H., & O'Hara-Dhand, K. A. 1996. Measurement of seismic attenuation from high-resolution crosshole data. *Geophysics*, **61**, 1175–1188.

Nowick, A. S., & Berry, B. S. 1972. *Anelastic relaxation in crystalline solids.* Academic Press.

O'Connell, R. J., & Budiansky, B. 1977. Viscoelastic properties of fluid-saturated cracked solids. *Journal of Geophysical Research*, **82**(Dec.), 5719–5736.

O'Hara, S. G. 1989. Elastic-wave attenuation in fluid-saturated Berea sandstone. *Geophysics*, **54**, 785–788.

Parker, R. D. 1968. *The effect of kerogen content on ultrasonic velocities in oil shales.* M.Phil. thesis, University of Texas at Austin.

Parra, J. O. 1997. The transversely isotropic poroelastic wave equation including the Biot and the squirt mechanisms: Theory and application. *Geophysics*, **62**, 309–318.

Parra, J. O., Hackert, C. L., & Xu, P. 2002. Characterization of fractured low Q zones at the Buena Vista Hills reservoir, California. *Geophysics*, **67**, 1061–1070.

Pech, A., & Tsvankin, I. 2004. Quartic moveout coefficient for a dipping azimuthally anisotropic layer. *Geophysics*, **69**, 699–707.

Pointer, T., Liu, E., & Hudson, J. A. 2000. Seismic wave propagation in cracked porous media. *Geophysical Journal International*, **142**, 199–231.

Prasad, M., & Nur, A. 2003. Velocity and attenuation anisotropy in reservoir rocks. *Pages 1652–1655 of: Expanded Abstracts.* Society of Exploration Geophysicists.

Pride, S. R., & Berryman, J. G. 2003. Linear dynamics of double-porosity dual-permeability materials. I. Governing equations and acoustic attenuation. *Physical Review E*, **68**(Sept.), 036603–1–10.

Pride, S. R., Harris, J. M., Johnson, D. L., Mateeva, A., Nihel, K. T., Nowack, R. L., Rector, J. W., Spetzler, H., Wu, R., Yamomoto, T., Berryman, J. G., & Fehler, M. 2003. Acquisition/Processing—Permeability dependence of seismic amplitudes. *The Leading Edge*, **22**, 518–525.

Putnam, P. E. 1982. Fluvial channel sandstones within upper Mannville (Albian) of Lloydminster area, Canada - geometry, petrography, and paleogeographic implications. *The American Association of Petroleum Geologists Bulletin*, **66**, 436–459.

Quan, Y., & Harris, J. M. 1997. Seismic attenuation tomography using the frequency shift method. *Geophysics*, **62**, 895–905.

Rapoport, Miron B., Rapoport, Larisa I., & Ryjkov, Valery I. 2004. Direct detection of oil and gas fields based on seismic inelasticity effect. *The Leading Edge*, **23**, 276–278.

Rüger, A. 1997. P-wave reflection coefficients for transversely isotropic models with vertical and horizontal axis of symmetry. *Geophysics*, **62**, 713–722.

Rüger, A. 1998. Variation of P-wave reflectivity with offset and azimuth in anisotropic media. *Geophysics*, **63**, 935–947.

Rüger, A. 2002. *Reflection Coefficients and Azimuthal* AVO *Analysis in Anisotropic Media.* Society of Exploration Geophysicists.

Samec, P., Blangy, J. P., & Nur, A. 1990. Effect of viscoelasticity and anisotropy on amplitude-versus-offset interpretation. *SEG Technical Program Expanded Abstracts*, **9**, 1479–1482.

Schmidt, H., & Tango, G. 1986. Efficient global matrix approach to the computation of synthetic seismograms. *Geophysical Journal of Royal Astronomical Society*, **84**, 331–359.

Schmitt, D. R. 1999. Seismic attributes for monitoring of a shallow heated heavy oil reservoir: A case study. *Geophysics*, **64**, 368–377.

Shuey, R. T. 1985. A simplification of the Zoeppritz equations. *Geophysics*, **50**, 609–614.

Sidler, R., & Carcione, J. M. 2007. Wave reflection at an anelastic transversely isotropic ocean bottom. *Geophysics*, **72**(5), SM139–SM146.

Spencer, J. W. 1979. Bulk and shear attenuation in Berea Sandstone: The effects of pore fluids. *Journal of Geophysical Research*, **84**(Dec.), 7521–7523.

Stanley, D., & Christensen, N. I. 2001. Attenuation anisotropy in shale at elevated confining pressure. *International Journal of Rock Mechanics & Mining Sciences*, **38**, 1047–1056.

Stovas, A., & Ursin, B. 2003. Reflection and transmission responses of layered transversely isotropic viscoelastic media. *Geophysical Prospecting*, **51**, 447–477.

Strobl, G. 1997. *The physics of polymers - concepts for understanding their structures and behaviors.* Springer-Verlag.

Tao, G., & King, M. S. 1990. Shear-wave velocity and Q anisotropy in rocks: A laboratory study. *International Journal of Rock Mechanics and Mining Science & Geomechanics Abstracts*, **27**(Oct.), 353–361.

Thomsen, L. 1986. Weak elastic anisotropy. *Geophysics*, **51**, 1954–1966.

Toksöz, M. N., Johnston, D. H., & Timur, A. 1979. Attenuation of seismic waves in dry and saturated rocks: I. Laboratory measurements. *Geophysics*, **44**, 681–690.

Tonn, R. 1991. The determination of the seismic quality factor Q from VSP data: A comparison of different computational methods. *Geophysical Prospecting*, **39**, 1–27.

Tsvankin, I. 1995. *Seismic Wavefields in Layered Isotropic Media.* Samizdat Press.

Tsvankin, I. 1997. Anisotropic parameters and P-wave velocity for orthorhombic media. *Geophysics*, **62**, 1292–1309.

Tsvankin, I. 2005. *Seismic Signatures and Analysis of Reflection Data in Anisotropic Media.* 2 edn. Elsevier Science.

Tutuncu, A. N., Podio, A. L., Gregory, A. R., & Sharma, M. M. 1998. Nonlinear viscoelastic behavior of sedimentary rocks, Part I: Effect of frequency and strain amplitude. *Geophysics*, **63**, 184–194.

Ursin, B., & Stovas, A. 2002. Reflection and transmission responses of a layered isotropic viscoelastic medium. *Geophysics*, **67**, 307–323.

Valle-García, R., & Ramírez-Cruz, L. 2002. Spectral attributes for attenuation analysis in a fractured carbonate reservoir. *The Leading Edge*, **21**, 1038–1041.

van der Baan, M., & Smit, D. 2006. Amplitude analysis of isotropic P-wave reflections. *Geophysics*, **71**(6), C93–C103.

Varela, I., Liu, E., & Chapman, M. 2006. Azimuthal multi-attribute analysis for fracture properties in time lapse VSP data. *SEG Technical Program Expanded Abstracts*, **25**, 3432–3436.

Vasco, D. W., Peterson, J. E., & Majer, E. L. 1996. A simultaneous inversion of seismic traveltimes and amplitudes for velocity and attenuation. *Geophysics*, **61**, 1738–1757.

Vasconcelos, I., & Jenner, E. 2005. Estimation of azimuthally varying attenuation from wide-azimuth P-wave data. *SEG Technical Program Expanded Abstracts*, **24**, 123–126.

Vasconcelos, I., & Tsvankin, I. 2006. Nonhyperbolic moveout inversion of wide-azimuth P-wave data for orthorhombic media. *Geophysical Prospecting*, **54**, 535–552.

Vavryčuk, V. 2007. Ray velocity and ray attenuation in homogeneous anisotropic viscoelastic media. *Geophysics*, **72**(6), D119–D127.

Vavryčuk, V. 2008. Velocity, attenuation, and quality factor in anisotropic viscoelastic media: A perturbation approach. *Geophysics*, **73**(5), D63–D73.

Vavryčuk, V., & Psencík, I. 1998. PP-wave reflection coefficients in weakly anisotropic elastic media. *Geophysics*, **63**, 2129–2141.

Vernik, L., & Liu, X. 1997. Velocity anisotropy in shales: A petrophysical study. *Geophysics*, **62**, 521–532.

Vernik, L., & Nur, A. 1992. Ultrasonic velocity and anisotropy of hydrocarbon source rocks. *Geophysics*, **57**, 727–735.

Vo-Thanh, D. 1990. Effects of fluid viscosity on shear-wave attenuation in saturated sandstones. *Geophysics*, **55**, 712–722.

Walsh, J. B. 1966. Seismic Wave Attenuation in Rock Due to Friction. *Journal of Geophysical Research*, **71**(May), 2591–2599.

Wang, X., & Tsvankin, I. 2009. Interval anisotropic parameter estimation using velocity-independent layer stripping. *Geophysics, in print.*

Wang, Z. 2002. Seismic anisotropy in sedimentary rocks, part 2: Laboratory data. *Geophysics*, **67**, 1423–1440.

Wilhelm, M. 2002. Fourier-transform rheology. *Macromolecular Materials and Engineering*, **287**, 83–105.

Willis, M., Rao, R., Burns, D., Byun, J., & Vetri, L. 2004. Spatial orientation and distribution of reservoir fractures from scattered seismic energy. *Pages 1535–1538 of: Expanded Abstracts.* Society of Exploration Geophysicists.

Winkler, K., Nur, A., & Gladwin, M. 1979. Friction and seismic attenuation in rocks. *Nature*, **277**, 528–531.

Winkler, K. W., & Nur, A. 1982. Seismic attenuation: Effects of pore fluids and frictional-sliding. *Geophysics*, **47**, 1–15.

Xu, X., & Tsvankin, I. 2006. Anisotropic geometrical-spreading correction for wide-azimuth P-wave reflections. *Geophysics*, **71**, D161–D170.

Xu, X., Tsvankin, I., & Pech, A. 2005. Geometrical spreading of P-waves in horizontally layered, azimuthally anisotropic media. *Geophysics*, **70**(5), D43–D53.

Zhang, Y., Rodrigue, D., & Aït-Kadi, A. 2003. Torsion properties of high density polyethylene foams. *Journal of Cellular Plastics*, **39**, 451–474.

Zhu, Y. 2006. *Seismic wave propagation in attenuative anisotropic media.* Ph.D. thesis, Colorado School of Mines.

Zhu, Y., & Tsvankin, I. 2006. Plane-wave propagation in attenuative transversely isotropic media. *Geophysics*, **71**(2), T17–T30.

Zhu, Y., & Tsvankin, I. 2007. Plane-wave attenuation anisotropy in orthorhombic media. *Geophysics*, **72**(1), D9–D19.

Zhu, Y., Tsvankin, I., & Vasconcelos, I. 2007a. Effective attenuation anisotropy of thin-layered media. *Geophysics*, **72**(5), D93–D106.

Zhu, Y., Tsvankin, I., Dewangan, P., & van Wijk, K. 2007b. Physical modeling and analysis of P-wave attenuation anisotropy in transversely isotropic media. *Geophysics*, **72**(1), D1–D7.

Appendix A

Complex wave vector for isotropic attenuative media

We consider a harmonic plane wave with an arbitrary inhomogeneity angle ξ propagating in isotropic attenuative media:

$$A(\mathbf{x},t) = A_0\, e^{i(\omega\, t - \mathbf{k}\cdot\mathbf{x})}\,, \tag{A.1}$$

where ω is the angular frequency and $\mathbf{k} = \mathbf{k}^R - i\,\mathbf{k}^I$ is the complex wave vector responsible for the velocity and the attenuation coefficient. Substitution of the plane wave A.1 into the acoustic wave equation results in

$$k_1^2 + k_2^2 + k_3^2 = \frac{\omega^2}{V^2\left(1 + \dfrac{i}{Q}\right)}\,, \tag{A.2}$$

where V is the real part of the medium velocity, and Q is the quality factor. Dropping quadratic and higher-order terms in $1/Q$, we rewrite equation A.2 as

$$(k^R)^2 - 2\,i\,\mathbf{k}^R\cdot\mathbf{k}^I - (k^I)^2 = \frac{\omega^2}{V^2}\left(1 - \frac{i}{Q}\right); \tag{A.3}$$

$k^R = |\mathbf{k}^R|$ and $k^I = |\mathbf{k}^I|$. Equation A.3 can be separated into the real and imaginary parts:

$$(k^R)^2 - (k^I)^2 = \frac{\omega^2}{V^2}\,, \tag{A.4}$$

$$\mathbf{k}^R\cdot\mathbf{k}^I = \frac{\omega^2}{2V^2Q}\,. \tag{A.5}$$

When the medium is non-attenuative and $1/Q = 0$, the right-hand side of equation A.5

vanishes. Then the vectors $\mathbf{k}^R$ and $\mathbf{k}^I$ of an inhomogeneous (evanescent) plane wave have to be orthogonal, with the relationship between k^R and k^I determined by equation A.4.

Because the factor Q responsible for attenuation is positive, equation A.5 can be satisfied only if $\mathbf{k}^R \cdot \mathbf{k}^I > 0$, which requires that $\cos\xi > 0$ and $\xi < 90°$. (We make the assumption that $\xi > 0$ because the solutions of equations A.4 and A.5 do not depend on the sign of ξ.) With the inhomogeneity angle smaller than 90°, equation A.5 allows us to express k^I through k^R as

$$k^I = \frac{\omega^2}{2\,k^R V^2 Q \cos\xi}\,. \tag{A.6}$$

Substitution of k^I into equation A.4 yields a quadratic equation for $(k^R)^2$, which has only one positive solution:

$$(k^R)^2 = \frac{\omega^2}{2V^2}\left[\sqrt{1+\frac{1}{(Q\cos\xi)^2}}+1\right]. \tag{A.7}$$

The corresponding imaginary part k^I can be obtained from either equation A.4 or A.6:

$$(k^I)^2 = \frac{\omega^2}{2V^2}\left[\sqrt{1+\frac{1}{(Q\cos\xi)^2}}-1\right]. \tag{A.8}$$

For typical large values of the quality factor, the product $(Q\cos\xi) \gg 1$, unless the inhomogeneity angle is close to 90°. Expanding the radical in equations A.7 and A.8 in $1/(Q\cos\xi)^2$, we find

$$k^R \cong \frac{\omega}{V}\left[1+\frac{1}{8(Q\cos\xi)^2}\right], \tag{A.9}$$

$$k^I \cong \frac{\omega}{2VQ\cos\xi}\left[1-\frac{1}{8(Q\cos\xi)^2}\right]. \tag{A.10}$$

Equations A.9 and A.10 can be simplified further by neglecting the small (compared to unity) term $1/[8(Q\cos\xi)^2]$:

$$k^R = \frac{\omega}{V}, \tag{A.11}$$

$$k^I = \frac{\omega}{2VQ\cos\xi}\,. \tag{A.12}$$

A.1 Large Inhomogeneity Angles

Although equations A.11 and A.12 are sufficiently accurate for a wide range of inhomogeneity angles, they break down when $\xi \to 90°$. For $(Q\cos\xi) \ll 1$, equations A.7 and A.8 can be approximated by

$$k^R = \frac{\omega}{V\sqrt{2Q\cos\xi}}\left(1+\frac{Q\cos\xi}{2}\right), \tag{A.13}$$

$$k^I = \frac{\omega}{V\sqrt{2Q\cos\xi}}\left(1-\frac{Q\cos\xi}{2}\right). \tag{A.14}$$

The phase attenuation coefficient $\mathcal{A}$ can be found from equations A.13 and A.14:

$$\mathcal{A} = \frac{k^I}{k^R} = 1 - Q\cos\xi\,; \tag{A.15}$$

here, we have dropped the term quadratic in $(Q\cos\xi)$.

A.2 Group Angle

In elastic isotropic media, the group- and phase-velocity vectors are always parallel. If, however, the medium is strongly attenuative and $\xi \neq 0°$, the group direction might deviate from the phase direction. The group-velocity vector in arbitrarily anisotropic, attenuative media can be computed from (Červený & Pšenčík, 2006)

$$\begin{aligned}(V_g)_i &= \frac{S_i}{\mathbf{S}\cdot\mathbf{p}^R} \\ &= \frac{(a_{ijkl}\,g_k\,g_j^*\,p_l)^R}{(a_{ijkl}\,g_k\,g_i^*\,p_l)^R\,p_j^R}\,,\end{aligned} \tag{A.16}$$

where $\mathbf{S}$ is the energy flux, a_{ijkl} is the density-normalized stiffness tensor, $\mathbf{p}$ is the slowness vector, and $\mathbf{g}$ is the polarization vector; the superscripts "R" and "$*$" represent the real part and complex conjugate, respectively.

For isotropic media, equation A.16 yields the following components of $\mathbf{V}_g$:

$$\mathbf{V}_g = \frac{\omega}{k^R}\left[\frac{k^I\sin\xi}{k^RQ + k^I\cos\xi}, 0, 1\right]. \tag{A.17}$$

From equation A.17, we find the group angle ψ:

$$\tan\psi = \frac{k^I \sin\xi}{k^R Q + k^I \cos\xi}\,. \tag{A.18}$$

To obtain the group angle for small and moderate inhomogeneity angles, we substitute equations A.11 and A.12 into equation A.18, yielding

$$\tan\psi = \frac{\tan\xi}{1+2Q^2} \ll 1\,. \tag{A.19}$$

For angles ξ approaching 90°, we substitute equation A.15 into equation A.18 and linearize the result in $\cos\xi$ to get

$$\tan\psi = \frac{1}{Q} - \cos\xi\,. \tag{A.20}$$

It is clear that for large inhomogeneity angles and strongly attenuative media, the angle ψ may not be negligible.

Appendix B

Perturbation analysis

Here, we derive analytic expressions for the real and imaginary parts of the wave vector in arbitrarily anisotropic, attenuative media using first-order perturbation theory. A homogeneous, isotropic, attenuative full space is taken as the background medium (Figure B.1a). The inhomogeneity angle ξ between the real ($k^{R,0}$) and imaginary ($k^{I,0}$) parts of the wave vector in the background can be arbitrarily large. The background medium is perturbed to make it anisotropic in terms of both velocity and attenuation (Figure B.1b), which results in perturbations of the real (Δk^R) and imaginary (Δk^I) parts of the wave vector. Because the inhomogeneity angle ξ is a free parameter, we choose not to perturb it when making the medium anisotropic. This implies that the vectors $\mathbf{k}^R$ and $\mathbf{k}^{R,0}$, as well as $\mathbf{k}^I$ and $\mathbf{k}^{I,0}$, are parallel.

We choose $\mathbf{k}^0$ such that $\mathbf{k}^{R,0}$ coincides with the axis x_3 and $\mathbf{k}^{I,0}$ lies in the $[x_1, x_3]$-plane (Figures B.1a and B.1b). This approach differs from the one adopted by Jech & Pšenčík (1989), Červený & Pšenčík (2008b), and Vavryčuk (2008), who used a fixed reference frame. To compute the perturbations for a different vector $\mathbf{k}$ in the same medium, we rotate the coordinate frame such that $\mathbf{k}^R$ coincides with the axis x_3 and $\mathbf{k}^I$ lies in the $[x_1, x_3]$-plane. This approach involves the rotation of the density-normalized stiffness tensor a_{ijkl} but obviates the need for introducing two additional angles needed to define the orientations of $\mathbf{k}^R$ and $\mathbf{k}^I$.

B.1 Real and Imaginary Parts of the Wave Vector

We start with the Christoffel equation in the perturbed medium:

$$(G_{ik} - \delta_{ik})\, g_k = 0\,, \tag{B.1}$$

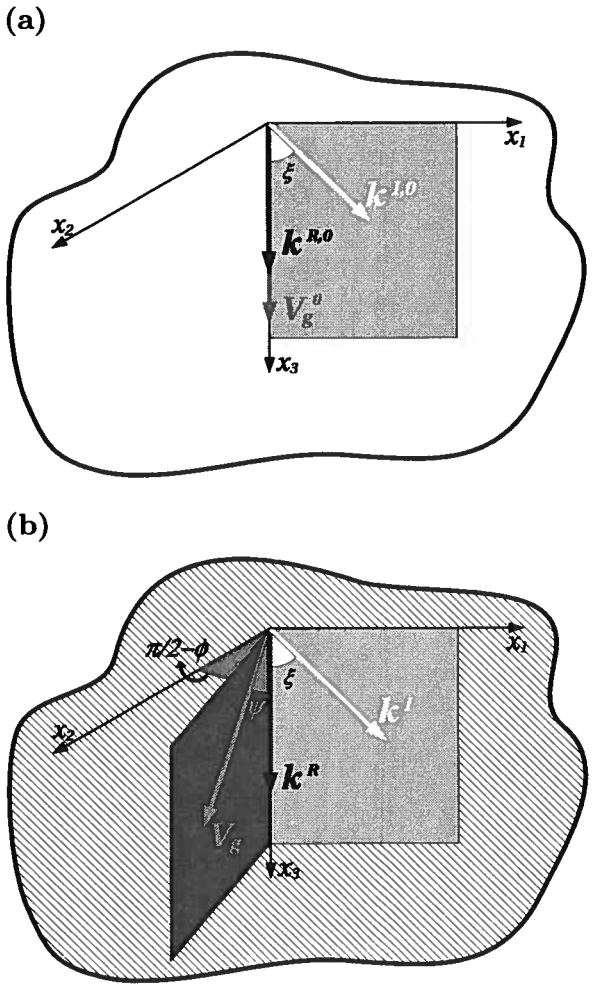

Figure B.1: Isotropic attenuative background medium (a) is perturbed to make it anisotropic (b). $\mathbf{k}^{R,0}$ and $\mathbf{k}^{I,0}$ are the real and imaginary parts of the wave vector in the background, and $\mathbf{k}^R = \mathbf{k}^{R,0} + \Delta\mathbf{k}^R$ and $\mathbf{k}^I = \mathbf{k}^{I,0} + \Delta\mathbf{k}^I$ form the wave vector in the perturbed medium; ξ is the inhomogeneity angle. The vectors $\mathbf{k}^{R,0}$ and $\mathbf{k}^R$ are parallel to the vertical x_3 direction while $\mathbf{k}^{I,0}$ and $\mathbf{k}^I$ are confined to the $[x_1, x_3]$-plane. $\mathbf{V}_g^0$ is the group velocity in the background; ψ is the polar group angle after the perturbation, and ϕ is the azimuth of the perturbed vector $\mathbf{V}_g$ with respect to the $[x_1, x_3]$-plane.

where $G_{ik} = a_{ijkl}\, p_j\, p_l$ is the Christoffel matrix, $\mathbf{p}$ is the complex slowness vector, and $\mathbf{g}$ is the polarization vector of the plane wave. Perturbation of equation B.1 yields

$$\left(G^0_{ik} + \Delta G_{ik} - \delta_{ik}\right)\left(g^0_k + \Delta g_k\right) = 0\,, \tag{B.2}$$

which can be linearized to obtain

$$\left(G^0_{ik} - \delta_{ik}\right)\Delta g_k + \Delta G_{ik}\, g^0_k = 0\,, \tag{B.3}$$

where $\mathbf{g}^0$ is the plane-wave polarization in the background and $\Delta\mathbf{g}$ is the perturbation of the polarization vector. The polarization $\mathbf{g}^0$ defines whether the wave mode is P, SV, or SH. The mode obtained by perturbing the SV-wave will be denoted S_1, and the perturbed SH-wave will be denoted S_2. Multiplying equation B.3 with g^0_i (Jech & Pšenčík, 1989) reduces equation B.3 to

$$\Delta G_{ik}\, g^0_i\, g^0_k = 0\,, \tag{B.4}$$

with

$$\Delta G_{ik} = \Delta a_{ijkl}\, p^0_j\, p^0_l + 2a^0_{ijkl}\, \Delta p_j\, p^0_l\,, \tag{B.5}$$

where a^0_{ijkl} and $\mathbf{p}^0$ are defined in the isotropic background, and Δa_{ijkl} and $\Delta\mathbf{p}$ are the perturbations. The tensors a^0_{ijkl} and Δa_{ijkl} are given by

$$a^0_{ijkl} = a^{R,0}_{ijkl} + i a^{I,0}_{ijkl} = a^{R,0}_{ijkl}\left(1 + \frac{i}{Q^0_{ijkl}}\right), \tag{B.6}$$

$$\Delta a_{ijkl} = \Delta a^R_{ijkl} + i\Delta a^I_{ijkl}\,, \tag{B.7}$$

where the superscripts "R" and "I" denote the real and imaginary parts, and Q^0_{ijkl} is the ratio a^R_{ijkl}/a^I_{ijkl}. The background slowness $\mathbf{p}^0$ and its perturbation $\Delta\mathbf{p}$ can be expressed as

$$\mathbf{p}^0 = \left[-ip^{I,0}\sin\xi,\ 0,\ p^{R,0} - ip^{I,0}\cos\xi\right], \tag{B.8}$$

$$\Delta\mathbf{p} = \left[-i\Delta p^I \sin\xi,\ 0,\ \Delta p^R - i\Delta p^I \cos\xi\right], \tag{B.9}$$

where $p^{R,0}$, $p^{I,0}$ and Δp^R, Δp^I are the magnitudes of the real and imaginary parts of $\mathbf{p}^0$ and $\Delta\mathbf{p}$, respectively.

Assuming $(Q^0\cos\xi) \gg 1$, we solve equation B.4 for $\Delta k^R = \omega\Delta p^R$ and $\Delta k^I = \omega\Delta p^I$:

$$\frac{\Delta k^R}{k^{R,0}} = -\frac{\chi^R}{2} - \frac{\chi^I}{2Q^0}\left(1 - \frac{\sec^2\xi}{2}\right), \tag{B.10}$$

$$\frac{\Delta k^I}{k^{I,0}} = -\frac{\chi^R}{2} + Q^0\chi^I, \tag{B.11}$$

where χ^R and χ^I are the real and imaginary parts of $\chi = \Delta a_{ijkl}p_j^0 p_l^0 g_i^0 g_k^0$. The above analysis is valid for all three modes (P-, S_1-, and S_2-waves). By choosing the corresponding $\mathbf{k}^0$ and χ, we can compute the perturbations of the complex wave vector for any of the three modes. The term χ for P-, S_1-, and S_2-waves has the form

$$\begin{aligned}\chi_P =& \frac{1}{V_{P0}^2}\left(\Delta a_{33}^R + \frac{\Delta a_{33}^I}{Q_{P0}} + \frac{2\Delta a_{35}^I}{Q_{P0}}\tan\xi\right)\\ &+ i\frac{1}{V_{P0}^2}\left(-\frac{\Delta a_{33}^R}{Q_{P0}} + \Delta a_{33}^I - \frac{2\Delta a_{35}^R}{Q_{P0}}\tan\xi\right),\end{aligned} \tag{B.12}$$

$$\begin{aligned}\chi_{S_1} =& \frac{1}{V_{S0}^2}\left(\Delta a_{55}^R + \frac{\Delta a_{55}^I}{Q_{S0}} + \frac{\Delta a_{15}^I - \Delta a_{35}^I}{Q_{S0}}\tan\xi\right)\\ &+ i\frac{1}{V_{S0}^2}\left(-\frac{\Delta a_{55}^R}{Q_{S0}} + \Delta a_{55}^I - \frac{\Delta a_{15}^R - \Delta a_{35}^R}{Q_{S0}}\tan\xi\right),\end{aligned} \tag{B.13}$$

and

$$\begin{aligned}\chi_{S_2} =& \frac{1}{V_{S0}^2}\left(\Delta a_{44}^R + \frac{\Delta a_{44}^I}{Q_{S0}} + \frac{\Delta a_{46}^I}{Q_{S0}}\tan\xi\right)\\ &+ i\frac{1}{V_{S0}^2}\left(-\frac{\Delta a_{44}^R}{Q_{S0}} + \Delta a_{44}^I - \frac{\Delta a_{46}^R}{Q_{S0}}\tan\xi\right);\end{aligned} \tag{B.14}$$

Q_{P0} and Q_{S0} are the P- and S-wave quality factors in the background medium. Substituting equations B.12–B.14 into equations B.10 and B.11 and retaining only the terms linear in

Δa_{ij} yields

$$\frac{\Delta k_P^R}{k_P^{R,0}} \approx -\frac{1}{V_{P0}^2}\left[\frac{\Delta a_{33}^R}{2} + \frac{\Delta a_{33}^I}{Q_{P0}}\left(1 - \frac{\sec^2\xi}{4}\right) + \frac{\Delta a_{35}^I}{Q_{P0}}\tan\xi\right], \tag{B.15}$$

$$\frac{\Delta k_P^I}{k_P^{I,0}} \approx -\frac{1}{V_{P0}^2}\left(\frac{3\Delta a_{33}^R}{2} - Q_{P0}\Delta a_{33}^I + 2\Delta a_{35}^R\tan\xi\right), \tag{B.16}$$

$$\frac{\Delta k_{S_1}^R}{k_{S_1}^{R,0}} \approx -\frac{1}{V_{S0}^2}\left[\frac{\Delta a_{55}^R}{2} + \frac{\Delta a_{55}^I}{Q_{S0}}\left(1 - \frac{\sec^2\xi}{4}\right) + \frac{\Delta a_{15}^I - \Delta a_{35}^I}{2Q_{S0}}\tan\xi\right], \tag{B.17}$$

$$\frac{\Delta k_{S_1}^I}{k_{S_1}^{I,0}} \approx -\frac{1}{V_{S0}^2}\left(\frac{3\Delta a_{55}^R}{2} - Q_{S0}\Delta a_{55}^I + (\Delta a_{15}^R - \Delta a_{35}^R)\tan\xi\right), \tag{B.18}$$

$$\frac{\Delta k_{S_2}^R}{k_{S_2}^{R,0}} \approx -\frac{1}{V_{S0}^2}\left[\frac{\Delta a_{44}^R}{2} + \frac{\Delta a_{44}^I}{Q_{S0}}\left(1 - \frac{\sec^2\xi}{4}\right) + \frac{\Delta a_{46}^I}{2Q_{S0}}\tan\xi\right], \tag{B.19}$$

and

$$\frac{\Delta k_{S_2}^I}{k_{S_2}^{I,0}} \approx -\frac{1}{V_{S0}^2}\left(\frac{3\Delta a_{44}^R}{2} - Q_{S0}\Delta a_{44}^I + \Delta a_{46}^R\tan\xi\right). \tag{B.20}$$

B.2 Normalized Phase Attenuation Coefficient

We linearize the normalized phase attenuation coefficient $\mathcal{A}$ for $\xi = 0°$ by retaining only the first-order terms:

$$\mathcal{A}|_{\xi=0°} = \left.\frac{k^I}{k^R}\right|_{\xi=0°} = \left.\frac{k^{I,0} + \Delta k^I}{k^{R,0} + \Delta k^R}\right|_{\xi=0°} \tag{B.21}$$

$$= \frac{1}{2Q_0}\left(1 + \frac{\Delta k^I}{k^{I,0}} - \frac{\Delta k^R}{k^{R,0}}\right). \tag{B.22}$$

By substituting Δk^R and Δk^I from equations B.15–B.20 into equation B.22, we obtain $\mathcal{A}|_{\xi=0°}$ in arbitrarily anisotropic media for all three modes:

$$\mathcal{A}|_{\xi=0°,P} = \frac{1}{2Q_{P0}} - \frac{1}{2V_{P0}^2}\left(\frac{\Delta a_{33}^R}{Q_{P0}} - \Delta a_{33}^I\right), \tag{B.23}$$

$$\mathcal{A}|_{\xi=0°,S_1} = \frac{1}{2Q_{S0}} - \frac{1}{2V_{S0}^2}\left(\frac{\Delta a_{55}^R}{Q_{S0}} - \Delta a_{55}^I\right), \tag{B.24}$$

$$\mathcal{A}|_{\xi=0^\circ,S_2} = \frac{1}{2Q_{S0}} - \frac{1}{2V_{S0}^2}\left(\frac{\Delta a_{44}^R}{Q_{S0}} - \Delta a_{44}^I\right). \tag{B.25}$$

B.3 Normalized Group Attenuation Coefficient

To obtain the normalized group attenuation from equation 3.32, we find the quantity $\tan\psi\cos\phi = V_{g1}/V_{g3}$ from equation A.16:

$$\tan\psi_P\cos\phi_P = \frac{2\Delta a_{35}^R}{V_{P0}^2}, \tag{B.26}$$

$$\tan\psi_{S_1}\cos\phi_{S_1} = \frac{\Delta a_{15}^R - \Delta a_{35}^R}{V_{S0}^2}, \tag{B.27}$$

and

$$\tan\psi_{S_2}\cos\phi_{S_2} = \frac{\Delta a_{46}^R}{V_{S0}^2}, \tag{B.28}$$

where only the leading-order terms are retained.

Next, we substitute Δk^R and Δk^I from equations B.15–B.20 and $\tan\psi$ from equations B.26–B.28 into equation 3.32 and retain only the terms linear in Δa_{ij}:

$$\mathcal{A}_{g,P} = \frac{1}{2Q_{P0}} - \frac{1}{2V_{P0}^2}\left(\frac{\Delta a_{33}^R}{Q_{P0}} - \Delta a_{33}^I\right), \tag{B.29}$$

$$\mathcal{A}_{g,S_1} = \frac{1}{2Q_{S0}} - \frac{1}{2V_{S0}^2}\left(\frac{\Delta a_{55}^R}{Q_{S0}} - \Delta a_{55}^I\right), \tag{B.30}$$

and

$$\mathcal{A}_{g,S_2} = \frac{1}{2Q_{S0}} - \frac{1}{2V_{S0}^2}\left(\frac{\Delta a_{44}^R}{Q_{S0}} - \Delta a_{44}^I\right). \tag{B.31}$$

Appendix C

Shear-wave phase and group quantities in TI media

Here, we present closed-form expressions for the shear-wave parameters Δk^R, Δk^I, $\mathcal{A}$, and $\mathcal{A}_g$ in TI media. Note that all equations in Appendix A are derived for the coordinate frame defined by the vectors $\mathbf{k}^R$ and $\mathbf{k}^I$. Therefore, in order to obtain Δk^R, Δk^I, $\mathcal{A}$, and $\mathcal{A}_g$ as a function of the phase angle θ (the angle between $\mathbf{k}^R$ and the x_3-axis), one needs to rotate the tensor Δa_{ijkl} accordingly. Since $\mathbf{k}^I$ is assumed to lie in the plane defined by $\mathbf{k}^R$, Δa_{ijkl} in Appendix A is rotated by the phase angle θ around the x_2-axis.

By linearizing the rotated tensor Δa_{ijkl} in the Thomsen velocity-anisotropy parameters ϵ, δ, and γ and in the Thomsen-style attenuation-anisotropy parameters ϵ_Q, δ_Q, and γ_Q (Zhu & Tsvankin, 2006), we obtain the real ($\mathbf{k}^R$) and imaginary ($\mathbf{k}^I$) parts of the wave vector from equations B.17–B.20:

$$\frac{\Delta k^R_{SV}}{k^{R,0}_{SV}} = -\sigma \sin^2\theta \cos^2\theta\,, \tag{C.1}$$

$$\frac{\Delta k^I_{SV}}{k^{I,0}_{SV}} = (\epsilon_Q - \delta_Q)\frac{g^2}{g_Q}\sin^2\theta\cos^2\theta + \sigma\frac{2-3g_Q}{g_Q}\sin^2\theta\cos^2\theta$$

$$- \sigma \sin 2\theta \cos 2\theta \tan\xi\,, \tag{C.2}$$

$$\frac{\Delta k^R_{SH}}{k^{R,0}_{SH}} = -\gamma \sin^2\theta\,, \tag{C.3}$$

$$\frac{\Delta k^I_{SH}}{k^{I,0}_{SH}} = \gamma_Q \sin^2\theta - \gamma\sin^2\theta - \gamma\sin 2\theta\tan\xi\,, \tag{C.4}$$

where $g = V_{P0}/V_{S0}$, the parameter $\sigma = g^2(\epsilon - \delta)$ controls the SV-wave phase velocity, $g_Q = Q_{P0}/Q_{S0}$, and the parameters γ and γ_Q are responsible for the SH-wave velocity and attenuation anisotropy, respectively (Zhu & Tsvankin, 2006).

The normalized SV- and SH-wave phase attenuation coefficients for $\xi = 0°$ can be found from equations B.24 and B.25:

$$\mathcal{A}|_{\xi=0°,SV} = \frac{1}{2Q_{S0}}\left(1 + \sigma_Q \sin^2\theta\cos^2\theta\right), \tag{C.5}$$

$$\mathcal{A}|_{\xi=0°,SH} = \frac{1}{2Q_{S0}}\left(1 + \gamma_Q \sin^2\theta\right), \tag{C.6}$$

where the parameter σ_Q (Zhu & Tsvankin, 2006) controls the SV-wave attenuation coefficient:

$$\sigma_Q = \frac{1}{g_Q}\left[2\sigma(1 - g_Q) + g^2(\epsilon_Q - \delta_Q)\right]. \tag{C.7}$$

To obtain the linearized shear-wave group angles in TI media, we use equations B.27 and B.28 (see also Tsvankin, 2005):

$$\tan\psi_{SV}\cos\phi_{SV} = \sigma\sin 2\theta\cos 2\theta \tag{C.8}$$

and

$$\tan\psi_{SH}\cos\phi_{SH} = \gamma\sin 2\theta\,. \tag{C.9}$$

Substituting the anisotropy parameters into equations B.30 and B.31 yields the following group attenuation coefficients:

$$\mathcal{A}_{g,SV} = \frac{1}{2Q_{S0}}\left(1 + \sigma_Q \sin^2\theta\cos^2\theta\right), \tag{C.10}$$

$$\mathcal{A}_{g,SH} = \frac{1}{2Q_{S0}}\left(1 + \gamma_Q \sin^2\theta\right). \tag{C.11}$$

Appendix D

Attenuation for large inhomogeneity angles

Here, we develop closed-form expressions for the wave vector $\mathbf{k}$ and group attenuation coefficient $\mathcal{A}_g$ for large angles ξ. For simplicity, we analyze only S_2-waves; expressions for P- and S_1-waves can be derived using the same procedure. The development follows the same approach as that described in Appendix B. The group angle ψ^0 in the background, however, does not vanish (equation 3.26), and the background vector $\mathbf{k}^0 = \mathbf{k}^{R,0} - i\mathbf{k}^{I,0}$ is given by equations 3.23 and 3.24. (Note that for small and moderate angles ξ considered in Appendix B, the group angle ψ^0 was zero.) For large ξ, the real ($k^{R,0}$) and imaginary ($k^{I,0}$) parts of the background wave vector are related by (equation 3.25)

$$\frac{k^{I,0}}{k^{R,0}} = 1 - Q^0 \cos\xi\,, \tag{D.1}$$

and the group angle ψ^0 is expressed as (equation 3.26)

$$\tan\psi^0 = \frac{1}{Q^0} - \cos\xi\,, \tag{D.2}$$

where Q^0 is the background quality factor. The perturbation produces a change in both the wave vector ($\Delta k^R - i\Delta k^I$) and the group direction.

First, we obtain k^R and k^I by solving equation B.4 and linearizing the result in Δa_{ij}. Eliminating terms quadratic or higher-order in $Q^0\cos\xi$ and those proportional to $\Delta a_{ij} Q^0 \cos\xi$, as well as setting terms quadratic in $\sin\xi$ to one, we find

$$\frac{k^R_{S_2}}{k^{R,0}_{S_2}} = \frac{k^I_{S_2}}{k^{I,0}_{S_2}} = 1 - \frac{1}{2V^2_{S0}}\left(\Delta a^R_{46} + \frac{\Delta a^I_{46}}{Q_{S0}}\right)\tan\xi$$

$$+ \frac{1}{4V^2_{S0}\cos\xi}\left(\Delta a^I_{44} - \frac{\Delta a^R_{44}}{Q_{S0}} - \Delta a^I_{66} + \frac{\Delta a^R_{66}}{Q_{S0}}\right). \tag{D.3}$$

For the special case of TI media, the S_2-mode becomes the SH-wave, and equation D.3 (after eliminating terms proportional to γ/Q_{S0}^2 and γ_Q/Q_{S0}^2) takes the form

$$\frac{k_{S_2}^R}{k_{S_2}^{R,0}} = \frac{k_{S_2}^I}{k_{S_2}^{I,0}} \approx 1 + \frac{\gamma \sin 2\theta}{2} \tan\xi - \frac{\gamma_Q \cos 2\theta}{4Q_{S0}} \frac{1}{\cos\xi}. \tag{D.4}$$

The product $\tan\psi \cos\phi$ needed to find $\mathcal{A}_g$ can be obtained from equation A.16:

$$\tan\psi\cos\phi = \frac{1}{Q_{S0}} - \cos\xi - \frac{1}{4V_{S0}^2}\left[\frac{2\Delta a_{46}^I}{Q_{S0}} - 6\Delta a_{46}^R + \left(\frac{3\Delta a_{44}^R}{Q_{S0}} + \frac{\Delta a_{66}^R}{Q_{S0}} + \Delta a_{44}^I - 5\Delta a_{66}^I\right)\sin\xi\right]. \tag{D.5}$$

The group attenuation coefficient $\mathcal{A}_g$ is found by substituting equations D.1–D.5 into equation 3.31:

$$\mathcal{A}_g = \frac{1}{Q_{S0}} - \cos\xi - \frac{1}{4V_{S0}^2}\left[\frac{3\Delta a_{44}^R}{Q_{S0}} + \frac{\Delta a_{66}^R}{Q_{S0}} + \Delta a_{44}^I - 5\Delta a_{66}^I + \left(\frac{2\Delta a_{46}^I}{Q_{S0}} - 6\Delta a_{46}^R\right)\sin\xi\right]; \tag{D.6}$$

equation D.6 is linearized in Δa_{ij} and $(Q_{S0}\cos\xi)$, and terms proportional to $(\Delta a_{ij} Q_{S0}\cos\xi)$ have been eliminated. The range of ξ for which equation D.6 is valid is set by the assumption $Q_{S0}\cos\xi \ll 1$ which ensures that $\mathcal{A}_g$ is positive. For the special case of TI media, $\mathcal{A}_g$ takes a simpler form after linearization in the anisotropy parameters:

$$\mathcal{A}_g = \frac{1}{Q_{S0}} - \cos\xi - \frac{3\gamma\sin 2\theta}{2}\sin\xi + \frac{2\gamma\cos 2\theta}{Q_{S0}} + \frac{\gamma_Q\cos 2\theta}{4Q_{S0}} + \frac{\gamma_Q\cos^2\theta}{4Q_{S0}}. \tag{D.7}$$

Appendix E

Linear functions in the approximate reflection coefficients

Here, we give explicit expressions for the linear functions f_i in the approximate equations for the reflection coefficients.

The functions f_1, f_2, f_3, and f_4 in equations 4.20 and 4.21 have the form

$$f_1 = \frac{1}{2g}\frac{\Delta\rho}{\rho_0} + \frac{1}{g}\frac{\Delta V_{S0}}{V_{S0}} + \frac{g}{4(1+g)^2}\Delta\delta + \frac{i}{g}\Delta\mathcal{A}_{S0} + \frac{g}{4(1+g)}\Delta\delta_Q\,, \tag{E.1}$$

$$f_2 = \frac{1}{2g}\frac{\Delta\rho}{\rho_0} + \frac{1}{g}\frac{\Delta V_{S0}}{V_{S0}} + \frac{g}{4(1+g)^2}\Delta\delta + \frac{i}{g}\Delta\mathcal{A}_{S0}\,, \tag{E.2}$$

$$\begin{aligned} f_3 =& \frac{3+g}{2g^2}\frac{\Delta\rho}{\rho_0} + \frac{4+g}{g^2}\frac{\Delta V_{S0}}{V_{S0}} - \frac{g}{(1+g)^2}\Delta\epsilon + \frac{5g}{4(1+g)^2}\Delta\delta \\ &+ i\frac{4+g}{g^2}\Delta\mathcal{A}_{S0} - \frac{g}{(1+g)^2}\Delta\epsilon_Q + \frac{4g-1}{4(1+g)}\Delta\delta_Q\,, \end{aligned} \tag{E.3}$$

$$f_4 = \frac{3+g}{2g^2}\frac{\Delta\rho}{\rho_0} + \frac{4+g}{g^2}\frac{\Delta V_{S0}}{V_{S0}} - \frac{g}{(1+g)^2}\Delta\epsilon + \frac{5g}{4(1+g)^2}\Delta\delta + i\frac{1}{g^2}\Delta\mathcal{A}_{S0}\,, \tag{E.4}$$

where $g \equiv V_{P0}/V_{S0}$.

The functions f_5, f_6, and f_7 in equations 4.25–4.27 are given by

$$f_5 = -i\frac{\Delta V_{P0}}{V_{P0}} + \Delta\mathcal{A}_{P0}\,, \tag{E.5}$$

$$f_6 = \frac{-2}{g^2}\frac{\Delta\rho}{\rho_0} + \frac{\Delta V_{P0}}{2V_{P0}} - \frac{4}{g^2}\frac{\Delta V_{S0}}{V_{S0}} + \frac{\Delta\delta}{2} + i\left(\frac{\Delta\mathcal{A}_{P0}}{2} - \frac{4\Delta\mathcal{A}_{S0}}{g^2}\right), \tag{E.6}$$

$$f_7 = \left(1+\frac{1}{g^2}\right)\frac{\Delta V_{P0}}{V_{P0}} - \Delta\delta + i\left(1+\frac{1}{g^2}\right)\Delta\mathcal{A}_{P0}\,. \tag{E.7}$$

Finally, for the functions f_8 and f_9 in equations 4.29 and 4.31 we have

$$f_8 = \frac{2+g}{4g}\frac{\Delta\rho}{\rho_0} + \frac{\Delta V_{S0}}{gV_{S0}} - \frac{g}{4(1+g)}\Delta\delta + \frac{i}{g}\Delta\mathcal{A}_{S0}\,, \tag{E.8}$$

$$f_9 = \frac{9+8g+g^2}{8g^2}\frac{\Delta\rho}{\rho_0} + \frac{3+2g}{g^2}\frac{\Delta V_{S0}}{V_{S0}} + \frac{3-13g}{8(1+g)}\Delta\delta + \frac{3g}{2(1+g)}\Delta\epsilon$$
$$+ i\,\frac{3+2g}{g^2}\Delta\mathcal{A}_{S0}\,. \tag{E.9}$$